HPS
HEAVY PHOTON SEARCH

A Proposal to Search for Massive Photons at Jefferson Laboratory

September 10, 2010

Authors

W. Cooper, M. Demarteau
Fermi National Accelerator Laboratory, Batavia, IL 60510-5011

S. Bueltmann, L. Weinstein
Old Dominion University, Norfolk, VA 23529

A. Grillo
University of California, Santa Cruz, CA 95064

M. Holtrop, K. Slifer, S. Phillips, E. Ebrahim
University of New Hampshire, Durham, NH 03824

P. Schuster, N. Toro
Perimeter Institute, Ontario, Canada N2L 2Y5

R. Essig, C. Field, M. Graham, G. Haller, R. Herbst, J. Jaros (Co-Spokesperson), C. Kenney,T. Maruyama,
K. Moffeit, T. Nelson, H. Neal, A. Odian, M. Oriunno, R. Partridge, D. Walz
SLAC National Accelerator Laboratory, Menlo Park, CA 94025

S. Boyarinov, V. Burkert, A. Deur, H. Egiyan, A. Freyberger, F.-X. Girod,
V. Kubarovsky, S. Stepanyan (Co-Spokesperson)
Thomas Jefferson National Accelerator Facility, Newport News, VA 23606

A. Fradi, B. Guegan, M. Guidal, S. Niccolai, S. Pisano, E. Rauly, P. Rosier and D. Sokhan
Institut de Physique Nucleaire d'Orsay, 91405 Orsay, France

M. Khandaker, C. Salgado
Norfolk State University, Norfolk, VA 23504

N. Dashyan, N. Gevorgyan, R. Paremuzyan, H. Voskanyan
Yerevan Physics Institute, 375036 Yerevan, Armenia

M. Battaglieri, R. DeVitta
INFN, Sezione di Genova, 16146 Genova, Italy

Table of Contents

1 Introduction

Interest in the possibility that a massive photon-like particle could exist has been piqued recently by suggestions from Arkani-Hamed et al. [1] and Pospelov and Ritz [2] and others that such a particle could mediate dark matter annihilations and account for recently observed electron/positron features in the cosmic rays, and perhaps even the putative DAMA dark matter annual modulation. The possible existence of a heavy photon was suggested earlier, however, especially by Holdom [3]. He considered the possibility that Nature has additional U(1)'s, such as those suggested in string theories, which would naturally kinetically mix with *the* photon, generating a coupling between the new heavy photon(s) and electric charge of order 10^{-3} e. Since it does couple to electric charge, the heavy photon could be produced when suitably energetic electron beams bremstrahlung off heavy targets, albeit at rates strongly suppressed compared to expected QED processes. For heavy photons of mass ~100 MeV, preferred by those trying to account for the cosmic ray data and in line with more general considerations as well, the decay would be to e^+e^-; at higher masses other channels would open up. The signature for a heavy photon would be twofold: 1) a sharp bump in the e^+e^- invariant mass above the copious QED trident background; and 2) a secondary decay vertex, since the coupling can be weak enough to generate detectable lifetime effects. For heavy photons of mass between 100 MeV and 1 GeV, electron beams of ~few GeV can initiate heavy photon bremstrahlung.

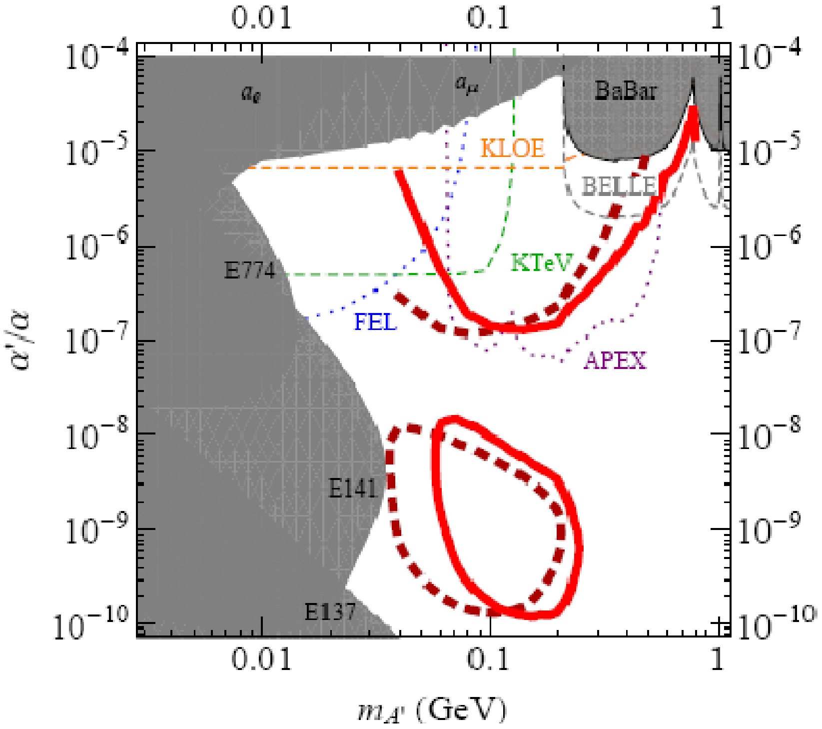

Figure 1.1. Existing heavy photon exclusion regions (gray), and proposed search regions for HPS (bold solid and dashed lines) and other future experiments (dotted lines) in the heavy photon mass-coupling plane.

Existing constraints on heavy photon masses and couplings come from axion searches, the anomalous magnetic moments of the muon and electron, and direct searches for heavy photons in the B factory data [4]. These constraints and the reach of the HPS and other proposed experiments are shown in Figure 1.1. Roughly speaking, heavy photons are allowed below a coupling strength of few x 10^{-3} and throughout the mass range of 50-1000 MeV/c^2. As indicated in the figure, the Heavy Photon Search experiment will simultaneously explore two large regions of this parameter space. One HPS search region focuses on a wide range of heavy photon masses and moderate couplings with a traditional bump-hunt search, which other experiments plan to probe as well. The other region is unique, and utilizes both invariant mass and separated decay vertex information to provide unparalleled sensitivity to small couplings over the mass range 50-250 MeV/c^2.

Physicists and engineers from SLAC, the Hall B Group at JLab and their collaborators, Fermilab, and UC Santa Cruz have developed a concept put forward in Reference [4] into this proposal. The experiment utilizes a high acceptance forward spectrometer with precise momentum, vertexing, and calorimetric measurement capability to provide ~1% momentum resolution, ~1 mm vertex resolution, and fast triggering and electron identification. The experiment probes a unique region of the mass-coupling plane where the heavy photon signal would be lost in the trident background without the additional signature of a secondary vertex displaced from the target, and it simultaneously accesses a higher mass region by relying on bump hunting alone. The experiment depends upon the 40 MHz readout capability of the silicon microstrip vertex/tracker which utilizes LHC readout electronics, the matching high rate capability of a highly segmented $PbWO_4$ calorimeter, and high rate triggering and data acquisition systems. Combined with CEBAF's superb duty-cycle, high intensities, and excellent beam properties, this high rate capability lets HPS achieve the high integrated luminosities required to search for heavy photons. As a bonus, HPS should also be able to observe a particle expected in conventional QED but as yet unseen, so-called true muonium. This $\mu^+ \mu^-$ atom is expected to decay into e^+e^- with the heavy photon signature, a sharp mass bump (at ~210 MeV/c^2) and a separated decay vertex, which in this case is often a centimeter or more beyond the target!

In what follows, we discuss the physics motivation for heavy photon searches, the properties of the heavy photon signal and the prominent QED backgrounds, the proposed beamline and apparatus, the performance of the apparatus as determined from detailed full Monte Carlo simulations, and finally the calculated reach of the experiment. We conclude with an overview of the resources needed for the experiment and a proposed run plan.

1.1 References

1. N. Arkani-Hamed , D.P. Finkbeiner, T. R. Slatyer, and N. Weiner, Phys. Rev. **D79**, 015014 (2009), ArXiv: 0810.0713.
2. M. Pospelov and A. Ritz, Phys. Lett. **B671**, 391 (2009), 0810.1502.
3. B. Holdom, Two U(1)'s and Epsilon Charge Shifts, Phys. Lett. **B166** (1986) 196.

4. J.D. Bjorken, R. Essig, P. Schuster, and N. Toro, "New Fixed-Target Experiments to Search for Dark Gauge Forces", Phys. Rev. **D80**, 2009, 075018, arXiv: 0906.0580.

2 Physics Motivation

We consider new sub-GeV mass vector bosons - “dark photons” A' - that couple very weakly to electrons (similar considerations apply to pseudo-vectors, scalars, and pseudo-scalars with sub-GeV mass that couple to electrons). It is useful to parameterize the coupling g' of the A' to electrons by a dimensionless $\varepsilon \equiv g'/e$, where e is the electron charge. Cross-sections for A' production then scale as $\alpha'/\alpha = \varepsilon^2$, where $\alpha' = g'^2/4\pi$ and $\alpha = e^2/4\pi$ are the fine-structure constants for the dark photon and ordinary electromagnetic interactions, respectively. This experiment will search for A′ bosons with mass $m_{A'} \sim 100$ MeV and $\alpha'/\alpha \leq 10^{-5}$, which can be produced by a reaction analogous to photon bremsstrahlung and will decay promptly to e^+e^- or other charged particle pairs. We refer the reader to Figure 2.3.1 for a summary of the reach of this experiment.

2.1 Motivation for New Physics Near the GeV Scale

New light vector particles, matter states, and their associated interactions are ubiquitous in extensions of the Standard Model [1-10]. However, the symmetries of the Standard Model restrict the interaction of ordinary matter with such new states. Indeed, most interactions consistent with Standard Model gauge symmetries and Lorentz invariance have couplings suppressed by a high mass scale. One of the few unsuppressed interactions is the coupling of charged Standard Model particles ψ,

$$\Delta L = g' A'^{\mu} \bar{\psi} \gamma_{\mu} \psi \qquad (2.1)$$

to a new gauge boson A′, which is quite poorly constrained for small g' (see Figure 2.3.1). Similar couplings between the A' and other Standard Model fermions are also allowed, with relations between their couplings (anomaly cancellation) required for the A' gauge symmetry to be quantum-mechanically consistent. For example, the A' could couple only to electrons and muons, with opposite charges $g'_e = -g'_\mu$ (a U(1) e,μ boson), or could have couplings proportional to the electromagnetic charges q_i of each fermion, $g_{qi} = \varepsilon\, e\, q_i$.

A' couplings to Standard Model matter with the latter structure can be induced by ordinary electromagnetic interactions through the kinetic mixing interaction proposed by Holdom [1],

$$\Delta L = \frac{\epsilon_Y}{2} F'_{\mu\nu} F_Y^{\mu\nu} \qquad (2.2)$$

where $F'_{\mu\nu} = \partial_\mu A'_\nu - \partial_\nu A'_\mu$ is the field strength of the A' gauge boson, and similarly $F_Y^{\mu\nu}$ is the hypercharge field strength. This effect is generic, ensures that the A' interactions respect parity, and (as we discuss below) naturally produces small g' and A' masses near the GeV scale. This mixing is equivalent in low-energy interactions to assigning a charge $\varepsilon e q_i$ to Standard Model particles of electromagnetic charge q_i, where $\varepsilon = \varepsilon_Y/\cos(\theta_W)$ and θ_W is the Weinberg mixing angle.

The A' couplings to neutrinos and parity-violating couplings are negligible compared to Z-mediated effects (see e.g. [12]).

As noted in [1], a new gauge boson A' that does not couple to Standard Model matter at a classical level can still couple through quantum-mechanical corrections. For example, loops of any particle X that couples to both the A′ and Standard Model hypercharge generates mixing of the form (2.1), with

$$\epsilon \sim 10^{-3} - 10^{-2}, \quad \frac{\alpha'}{\alpha} \sim 10^{-6} - 10^{-4} \qquad (2.3)$$

These quantum effects are significant regardless of the mass m_X of the particle in question, which could be well above the TeV scale (or even at the Planck scale) and thus evade detection.

Smaller ε are expected if nature has enhanced symmetry at high energies. For example, it has been conjectured that the strong and electroweak gauge groups of the Standard Model are embedded in a grand unified theory (GUT) with gauge group SU(5) or larger that is broken spontaneously at a high scale $M_{GUT} \approx 10^{16}$ GeV. In this case the mixing (2.1) is suppressed,

$$\epsilon_{GUT} \sim \frac{\alpha_i^2}{16\pi^2} \ln\left(\frac{M_{GUT}}{M_X}\right) \sim 10^{-5} - 10^{-3} \qquad (2.4)$$

where α_i are gauge couplings. An ε of this size leads to effective couplings

$$\frac{\alpha'}{\alpha} \sim 10^{-10} - 10^{-6} \qquad (2.5)$$

As shown in Figure 2.3.1, no experiment to date has probed the range of ε expected in grand unified theories for $m_{A'} \geq 50$ MeV.

An A' mass near but beneath the weak scale is particularly well-motivated, as U(1)' symmetry-breaking and the resulting A' mass may be determined by the same physics that generates the W and Z masses [13]. The best candidate for the origin of the weak scale is low-energy supersymmetry. In this case, the A' can naturally acquire mass suppressed by a loop factor or by $\sqrt{\varepsilon}$ compared to the weak scale, leading to MeV to GeV-scale A' masses [5,12,14-17]. In supersymmetric models, the gauge kinetic mixing (2.1) is accompanied by quartic interactions

$$\frac{\epsilon_Y}{4} g_Y g_D |\phi_D|^2 |h|^2 \qquad (2.6)$$

between the Standard Model Higgs doublet h and any scalar Φ_D charged under U(1)', where g_Y and g_D are the gauge couplings of Standard Model hypercharge and the A' coupling to Φ_D, respectively. Electroweak symmetry breaking gives h a weak-scale vacuum expectation value, so that (2.5) generates a mass term for Φ_D. For positively charged Φ_D, and sufficiently small bare mass, this mass term is negative and triggers U(1)' breaking by the Higgs mechanism. The resulting induced mass for the A' is

$$m_{A'} \sim \sqrt{\epsilon}\,\sqrt{\left(\frac{g_D g_Y}{g_2^2}\right)}\, m_W \sim MeV - GeV \qquad (2.7)$$

where g_2 is the Standard Model $SU(2)_L$ gauge coupling and m_W is the W-boson mass. The resulting mass is precisely in the 50-1000 MeV range targeted by this experiment. The combined resonance and vertexing search will probe a sizeable fraction of this parameter space. In particular, the resonance search will probe the small g_D region, e.g. for $g_D = 0.005$ and $\alpha'/\alpha \sim 7 \times 10^{-7}$, we have $m_{A'} \sim 150$ MeV/c^2, which is well within the reach of the experiment. The vertexing search will probe larger values for g_D, e.g. for $g_D = 0.1$ and $\alpha'/\alpha \sim 3 \times 10^{-7}$, we have $m_{A'} \sim 100$ MeV/c^2. Note that the mechanism of U(1)' breaking above does not rely on supersymmetry, as any quartic interaction of the form (2.5), with arbitrary coupling, can transmit electro-weak masses to the A'. Thus, the mass relation (2.6) should not be interpreted too literally.

We stress that the mass of the A' breaks any apparent symmetry between it and the photon: though Standard Model particles have induced ε-suppressed charges under the A', any new matter charged under the A' would not have any direct coupling to the photon, and would thus not have an electric "milli-charge". This is the main reason why such particles could have gone undetected.

An electron beam scattering on a high-Z target such as Tungsten will produce A's through bremsstrahlung reactions with a cross-section

$$\sigma_{A'} \sim 100\, pb\, \left(\frac{\epsilon}{10^{-4}}\right)^2 \left(\frac{100\, MeV}{m_{A'}}\right)^2 \qquad (2.8)$$

several orders of magnitude larger than in colliding electron and hadron beams [18]. The A' can decay to electrons, and is therefore visible as a narrow resonance in the trident e^+e^- mass spectrum.

Seeing such a new gauge boson would constitute the first discovery of a new gauge force since the observation of Z-mediated neutral currents. Besides the obvious physical interest of a fifth force, the A' like the Z could open up a new ``sector'' of light, weakly coupled particles whose spectrum and properties could be measured in fixed-target experiments and flavor factories. The A' sector would provide a new laboratory for many physical questions, and would be revealing precisely because its interactions with Standard Model particles are so weak. In particular, if nature is approximately supersymmetric near the TeV scale, the mass scale of supersymmetry breaking for the A' sector is naturally suppressed by ε times gauge couplings. In this case, supersymmetry could be studied easily in the A' sector, and possibly even discovered there by relatively low-energy experiments before Standard Model superpartners are seen at colliders.

2.2 Motivation for an A' from Dark Matter

Dark matter interpretations of recent astrophysical and terrestrial anomalies provide an urgent impetus to search for A's in the mass range 50 MeV - 1 GeV, with a coupling ε ~ $10^{-4} - 10^{-2}$.

The concordance model of big bang cosmology - the "Lambda Cold Dark Matter" (ΛCDM) model - explains all observations of the cosmic microwave background, large scale structure formation, and supernovae; see e.g. [19-23]. This model suggests that Standard Model particles make up only about 4% of the energy density in the Universe, while ``dark energy'' and ``dark matter'' make up 74% and 22%, respectively, of the Universe's energy density. The concordance model does not require dark matter to have any new interactions beyond gravity with Standard Model particles. However, an intriguing theoretical observation, dubbed the WIMP miracle, suggests that dark matter does have new interactions. In particular, if dark matter consists of ~100 GeV to 10 TeV particles interacting via the electroweak force ("weakly interacting massive particles" or "WIMPs"), they would automatically have the right relic abundance observed today.

In addition to the WIMP miracle, evidence from cosmic-ray data and the terrestrial direct dark matter detection experiment DAMA/LIBRA may indicate that dark matter interacts with ordinary matter not just gravitationally. While the WIMP miracle suggests that dark matter is charged under the Standard Model electroweak force, we will see that these observations are also consistent with the hypothesis that dark matter interacts with ordinary matter through a new *force, mediated by a new 50 MeV - 1 GeV mass gauge boson*.

In addition to explaining any or all of these observations, dark matter charged under this new force can easily have the correct thermal relic abundance observed today by virtue of its interactions via the new force carrier, reproducing the success of the WIMP dark matter hypothesis. The reason is that the thermal relic abundance is set by the annihilation cross-section at freeze-out, which is given by $\sigma_v \sim \pi \alpha_X^2 / m_{DM}^2$, where α_X is the coupling of the dark matter to the A′ and is independent of ε; for α_X of order the weak-interaction strength and dark matter masses of order the weak scale, the WIMP miracle is reproduced.

The satellites PAMELA [24] and Fermi [25], the balloon-borne detector ATIC [26], the ground-based Cherenkov telescope HESS [27,28], as well as other experiments, observe a likely excess in the cosmic-ray flux of electrons and/or positrons above backgrounds expected from normal astrophysical processes. If their source is dark matter annihilation or decay, synchrotron radiation from these electrons and positrons could also explain the "WMAP haze" near the Galactic center [29], which consists of an excess seen in the WMAP Cosmic Microwave Background data.

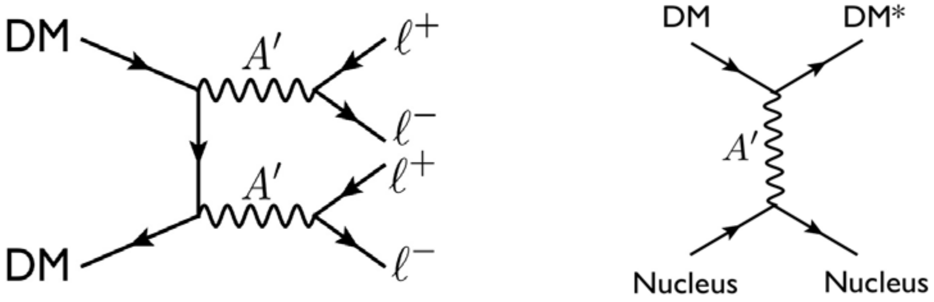

Figure 2.2.1 Left: Dark matter annihilation into the dark photon A', which decays into charged leptons such as electrons and/or muons, can explain the cosmic-ray electron and/or positron excesses seen by PAMELA, Fermi, ATIC, HESS, and other experiments. Right: Dark matter scattering into an excited state off nuclei through A' exchange in direct dark matter detection experiments can explain the annual modulation signal observed by DAMA/LIBRA, and the null results of other direct detection experiments.

In addition, starlight near the Galactic center would inverse Compton scatter off the high energy electrons and positrons and produce an excess in gamma-rays. A detection of a gamma-ray excess towards the Galactic center region in the gamma-ray data obtained with the Fermi satellite was recently reported in [30], and has been dubbed the “Fermi haze”.

Taken together, these observations by several experimental collaborations provide strong evidence that there is an unexplained excess in cosmic-ray electrons and positrons in our Galaxy. A very natural source of these excesses is dark matter annihilation. However, two features of these observations are incompatible with annihilation of ordinary thermal WIMP dark matter, but compatible with an alternative explanation: that dark matter is charged under a new U(1)' and annihilates into A′-pairs, which decay directly into electrons and positrons, or into muons that decay into electrons and positrons, see Figure 2.2.1 (left) (see e.g. [13,31-37]). These two features are:

- The annihilation cross-section required to explain the electron signal is 50-1000 times larger than the thermal freeze-out cross-section for an ordinary WIMP that is needed to reproduce the observed dark matter relic density. This can be explained if dark matter interacts with a new long range force mediated by an O(GeV) mass gauge boson, which allows the dark matter annihilation cross-section $\langle \sigma v \rangle$ to be enhanced at low dark matter velocities, i.e. ~ $\langle \sigma v \rangle \propto 1/v$. In this case, in the early Universe when the dark matter velocity was high (~ 0.3c), the annihilation cross-section that determines the relic abundance can naturally be the same as that of an ordinary WIMP and reproduce the WIMP miracle. However, in the Milky Way halo now, the dark matter has a much lower velocity ($v \sim 10^{-3}c$), leading to a large increase in the annihilation cross-section that is required to explain the cosmic-ray data. The enhancement at low velocities through a new long-range force is very well known and called the Sommerfeld effect [38].
- The PAMELA satellite did not see an anti-proton excess [39], which strongly suggests that dark matter annihilation is dominantly producing leptons, and not baryons. If dark matter is

interacting via a O(GeV) mass force particle in order to have a large annihilation rate via the Sommerfeld mechanism, then annihilations into the force carrier automatically fail to produce any baryons. Kinematically, the force carriers cannot decay into baryons, and are instead forced to decay into the lighter charged leptons. Thus, annihilation products of dark matter are leptonic in this case.

We note that within supersymmetry, neutralino ("wino") dark matter could be responsible for the electron and positron excesses, but ordinarily produces too many anti-protons. Moreover, if the neutralino is a thermal relic, its annihilation cross-section is too small to account for the observed signals.

To explain the additional sources of evidence for a new GeV scale force, we briefly summarize the consequence for dark matter mass spectra that follow from dark matter carrying a charge under a new force. If in addition to its U(1)′ charge, dark matter is charged under a non-Abelian force (a very natural possibility) and the force carriers acquire a mass, then radiative effects can split all components of the dark matter with size, $\delta \sim \alpha' \, \Delta m_{W'}$, where α' is the non-Abelian fine structure constant and $\Delta m_{W'}$ is the splitting of gauge boson masses [13]. Typically, these splittings are $\Delta m_{W'} \sim \alpha' \, m_{W'} \sim$ 1-10 MeV for $m_{W'} \sim 1$ GeV [14]. Thus, $\delta \sim 100$ keV for $\alpha' \sim 10^{-2}$. These splittings are completely analogous to the splittings that arise between the $\pi^{\pm}$ and π^0 from Standard Model SU(2) breaking. If instead a non-Abelian force confines at a scale $\Lambda_D \sim$ GeV, then a heavy-flavor meson can be cosmologically long-lived and thus a dark matter candidate [40]. Hyperfine interactions can naturally induce ~ 100 keV splittings of the dark matter particles in this case.

We emphasize that the GeV-scale non-Abelian force carrier particles mediate quantum corrections that generate the 100 keV and 1-10 MeV splittings of dark matter states [14, 40, 41]. When mass splittings arise, Dirac states split into two Majorana states, and the A' mediated interactions of dark matter with ordinary matter as well as dark matter self-interactions are dominated by inelastic interactions between the two Majorana states[13]. The direct dark matter detection experiment DAMA/LIBRA as well as the INTEGRAL telescope provide intriguing evidence for such interactions. The DAMA/NaI [43] and DAMA/LIBRA [44] experiments have reported an annual modulation signal over nearly eleven years of operation with more than 8σ significance. Modulation is expected because the Earth's velocity with respect to the dark matter halo varies as the Earth moves around the sun, and the phase of the observed modulation is consistent with this origin. A simple hypothesis that explains the spectrum and magnitude of the signal, and reconciles it with the null results of other experiments, is that dark matter-nucleus scattering is dominated by an inelastic process,

$$\chi N \to \chi^* N \tag{2.9}$$

in which the dark matter χ scatters off a nucleus N into an excited state χ^* with mass splitting $\delta \approx$ 100 keV [41,42]. The kinematics of these reactions is also remarkably consistent with all the distinctive properties of the nuclear recoil spectrum reported by DAMA/LIBRA. In addition, the INTEGRAL telescope [45] has reported a 511 keV photon signal near the galactic center, indicating a new source of ~ 1-10 MeV electrons and positrons. This excess could be explained by collisions of O(100 GeV~1 TeV) mass dark matter into excited states only slightly more massive (O(MeV)) in the galaxy [46]—the excited dark matter states subsequently decay back to the ground state by emitting an A′, which in turn decays to an e^+e^- pair. The 511 keV excess then arises from the subsequent annihilation of the produced positrons.

The existence of an A' may also help explain various other particle physics anomalies [47] such as the anomalous magnetic moment of the muon ((g-2)μ) [48].

While these experimental hints provide an urgent motivation to look for an A', it is important to emphasize the value of these searches in general. There has never been a systematic search for new GeV-scale force carriers that are weakly coupled to Standard Model particles. Nothing forbids their existence, and their discovery would have profound implications for our understanding of nature. The HPS experiment will probe a range of A' masses and couplings that are expected on general theoretical grounds, and suggested by astrophysical evidence.

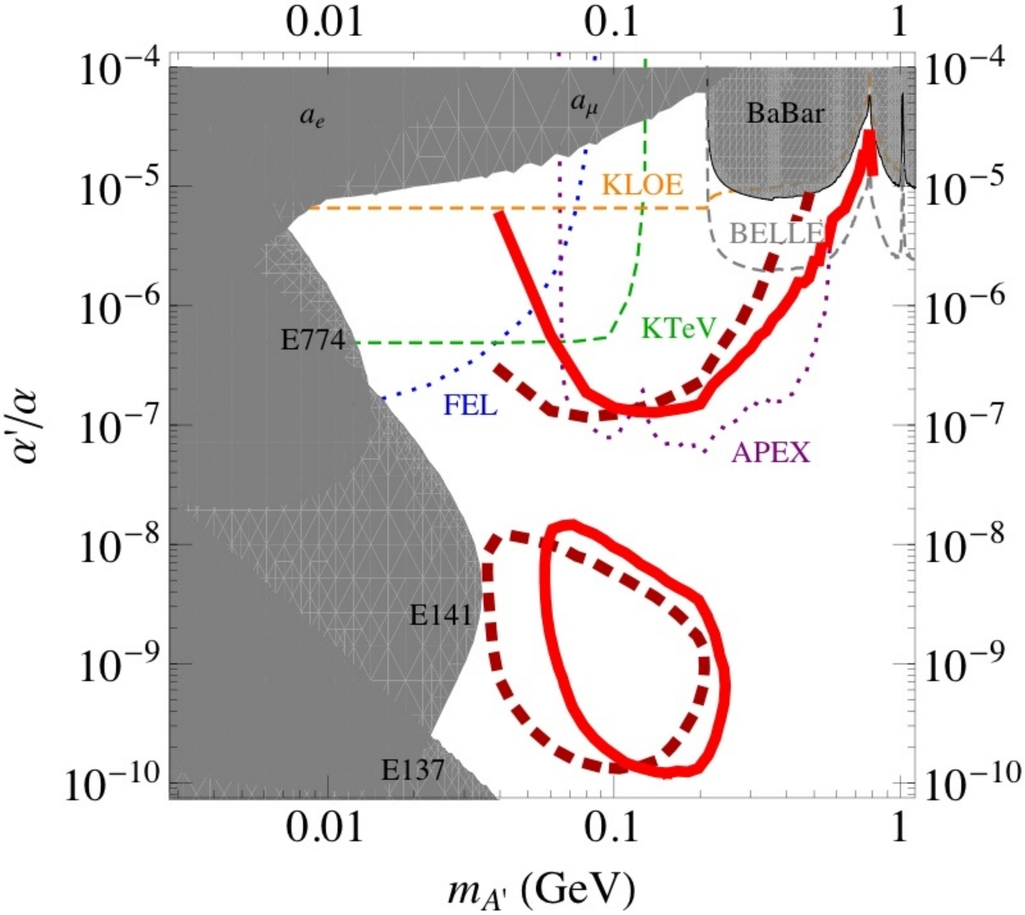

Figure 2.3.1 Anticipated reach in $\alpha'/\alpha = \varepsilon^2$ for the Heavy Photon Search (HPS) experiment at Hall B in JLab (red and maroon lines) with *existing* constraints on an A' from electron and muon anomalous magnetic moment measurements, a_e and a_μ (see [54]), the BaBar search for $\Upsilon(3S) \to \gamma\mu^+\mu^-$ [49], and three beam dump experiments, E137, E141, and E774 [55, 56, 57] (see [11]). The a_μ and $\Upsilon(3S)$ limits assume equal-strength couplings to electrons and muons. Also shown are *estimates* of *potential* 2σ sensitivities for A' searches in existing data (thin dashed lines), assuming optimal sensitivity as described in the text: KTeV $\pi^0 \to \gamma A' \to \gamma e^+$

e^-, (green dashed curve), KLOE $\Phi \rightarrow \eta A' \rightarrow \eta e^+ e^-$ (orange dashed curve) and Belle $e^+e^- \rightarrow \gamma A' \rightarrow \gamma \mu^+ \mu^-$ (gray dashed curve). In addition, we show the projected 2σ sensitivities for the proposed "APEX" experiment in JLab Hall A (dotted purple) [58] and the proposed "DarkLight" experiment using the JLab Free-Electron Laser (FEL) (dotted blue) [59] The solid red (dashed maroon) lines assume an electron beam with a current of 400 nA incident for 3×10^6 seconds on a 0.25% (0.125%) radiation length tungsten target and a beam energy of 5.5 GeV (3.3 GeV). The upper solid red and dashed maroon lines correspond to the 2σ sensitivity of a full resonance search. The lower contours in the same colors denote the sensitivity of a vertex-based resonance search. Here the lines correspond to 2.4 signal events where the vertex requirement was chosen to have 0.5 expected background events in each resolution-limited mass window. The full detector, trigger, and vertexing efficiencies have been included in these estimates. Note that all the curves for 3.3 GeV are *preliminary* and *conservative*. See Section 6 for a more detailed discussion.

.

2.3 **Current Limits on Light *U(1)* Gauge Bosons**

Constraints on new A's that decay to e^+e^- and the potential search reach of HPS are summarized in Figure 2.3.1. Also shown are constraints from electron and muon anomalous magnetic moment measurements, a_e and a_μ [47], the BaBar search for $\Upsilon(3S) \rightarrow \gamma A' \rightarrow \gamma \mu^+ \mu^-$ [49] and three beam dump experiments, E137, E141, and E774 [11]. The constraints from a_μ and the BaBar search assume that the A' couples to muons -- this is the case, for example, if it mixes with the photon. If it only couples to electrons, then the constraints on α'/α and $m_{A'}$ in the region to which the proposed experiment is sensitive are weaker than $\alpha'/\alpha \leq 10^{-4}$.

We caution that systematic uncertainties in the A' limit beyond those quoted in [49] may slightly weaken the resulting limit, which should therefore be taken as a rough approximation unless further analysis is done. First, A' production in B-factories is more forward-peaked than the $\Upsilon(3S)$ decay mode considered in [49], so that the signal acceptance is more uncertain. In addition, background distributions in [49] are derived from smooth polynomial fits to data collected on the $\Upsilon(4S)$ resonance, which is assumed to contain no signal. This assumption is not correct for A' production, though the resulting systematic effects are expected to be small.

Several past and current experiments have data that could be used to significantly improve current limits on α'/α, as discussed in [47,51,52]. Here, we estimate the potential sensitivity of searches in three channels ($\pi^0 \rightarrow \gamma A' \rightarrow \gamma e^+ e^-$, $\Phi \rightarrow \eta A' \rightarrow \eta e^+ e^-$, and $e^+e^- \rightarrow \gamma A' \rightarrow \gamma \mu^+ \mu^-$), considering only the statistical uncertainties and irreducible backgrounds. These are likely overestimates, as we are unable to include either systematic uncertainties or significant instrumental backgrounds such as photon conversion in the detector volume.

BaBar, BELLE, and KTeV (E799-II) have produced and detected large numbers of neutral pions, of order 10^{10}, of which roughly 1% decay in the Dalitz mode $\pi^0 \rightarrow \gamma e^+ e^-$. These experiments can search for the decay $\pi^0 \rightarrow \gamma A'$ induced by A'-photon kinetic mixing, which would appear as a narrow resonance over the continuum Dalitz decay background. KTeV has the largest π^0 sample, and its $e^+ e^-$ mass resolution can be approximated from the reported measurement of the $\pi^0 \rightarrow e^+ e^-$ branching fraction [50] to be roughly 2 MeV. This paper also reports the measured mass distribution of Dalitz decays above 70 MeV, from which we estimate potential sensitivity to α'/α

as small as 5×10^{-7} for 70 < m_{e+e-} < 100 MeV, as shown by the green shaded region in Figure 2.3.1.

Similarly, KLOE can search for the decay $\Phi \rightarrow \eta A'$, likewise induced by A' kinetic mixing with the photon, in a sample of 10^{10} Φ's. An analysis of this data is ongoing [53]. We have taken the blue dashed curve in Figure 2.3.1 from [51], which assumes that mass resolution σ_m is dominated by KLOE's 0.4% momentum resolution. We have adjusted the contours from [51] to determine a 2σ contour and enlarged the bin width used to determine signal significance from σ_m in [51] to $2.5\sigma_{\text{m}}$. Above the muon threshold, Φ decays are not competitive with B-factory continuum production.

In addition, BaBar and Belle can search for the continuum production mode $e^+e^- \rightarrow \gamma A' \rightarrow \gamma\mu^+ \mu^-$ in their full datasets. For example, an analysis of the Belle ϒ(4S) data set would increase statistics by a factor of ~ 24 relative to the BaBar ϒ(3S) search that we have interpreted as a limit above. We have derived the expected sensitivity (shown as a black dashed line in Figure 2.3.1 simply by scaling the ϒ(3S) estimated reach by √24. These searches have not been extended below the muon threshold because of large conversion backgrounds.

Finally, we also show the projected 2σ sensitivities for the proposed "APEX" experiment in JLab Hall A (dotted purple) [58] and the proposed "DarkLight" experiment using the JLab Free-Electron Laser (FEL) (dotted blue) [59]. The vertexing reach of HPS covers a region that is not covered by either of the other two proposed experiments.

2.4 References

1. B. Holdom, Two U(1)'s and Epsilon Charge Shifts, Phys. Lett. B166 (1986) 196.
2. M. J. Strassler, Possible effects of a hidden valley on supersymmetric phenomenology, hep-ph/0607160.
3. M. J. Strassler and K. M. Zurek, Echoes of a hidden valley at hadron colliders, Phys. Lett. B651 (2007) 374–379, [hep-ph/0604261].
4. M. J. Strassler, Why Unparticle Models with Mass Gaps are Examples of Hidden Valleys, 0801.0629.
5. K. R. Dienes, C. F. Kolda, and J. March-Russell, Kinetic mixing and the supersymmetric gauge hierarchy, Nucl. Phys. B492 (1997) 104–118, [hep-ph/9610479].
6. S. A. Abel and B. W. Schofield, Brane-antibrane kinetic mixing, millicharged particles and SUSY breaking, Nucl. Phys. B685 (2004) 150–170, [hep-th/0311051].
7. S. A. Abel, M. D. Goodsell, J. Jaeckel, V. V. Khoze, and A. Ringwald, Kinetic Mixing of the Photon with Hidden U(1)s in String Phenomenology, JHEP 07 (2008) 124, [0803.1449].
8. A. Ringwald, From Axions to Other WISPs, 0810.3106.

9. Y. Nomura and J. Thaler, Dark Matter through the Axion Portal, 0810.5397.
10. J. Mardon, Y. Nomura, and J. Thaler, Cosmic Signals from the Hidden Sector, 0905.3749.
11. J. D. Bjorken, R. Essig, P. Schuster, and N. Toro, New Fixed-Target Experiments to Search for Dark Gauge Forces, Phys. Rev. D80 (2009) 075018, [0906.0580].
12. M. Baumgart, C. Cheung, J. T. Ruderman, L.-T. Wang, and I. Yavin, Non-Abelian Dark Sectors and Their Collider Signatures, JHEP 04 (2009) 014, [0901.0283].
13. N. Arkani-Hamed, D. P. Finkbeiner, T. R. Slatyer, and N. Weiner, A Theory of Dark Matter, Phys. Rev. D79 (2009) 015014, [0810.0713].
14. N. Arkani-Hamed and N. Weiner, LHC Signals for a SuperUnified Theory of Dark Matter, JHEP 12 (2008) 104, [0810.0714].
15. C. Cheung, J. T. Ruderman, L.-T. Wang, and I. Yavin, Kinetic Mixing as the Origin of Light Dark Scales, 0902.3246.
16. D. E. Morrissey, D. Poland, and K. M. Zurek, Abelian Hidden Sectors at a GeV, 0904.2567.
17. A. Katz and R. Sundrum, Breaking the Dark Force, 0902.3271.
18. R. Essig, P. Schuster, and N. Toro, Probing Dark Forces and Light Hidden Sectors at Low-Energy e+e- Colliders, 0903.3941.
19. WMAP Collaboration, E. Komatsu et al., Five-Year Wilkinson Microwave Anisotropy Probe (WMAP) Observations: Cosmological Interpretation, Astrophys. J. Suppl. 180 (2009) 330–376, [0803.0547].
20. SDSS Collaboration, D. J. Eisenstein et al., Detection of the Baryon Acoustic Peak in the Large-Scale Correlation Function of SDSS Luminous Red Galaxies, Astrophys. J. 633 (2005) 560–574, [astro-ph/0501171].
21. Supernova Cosmology Project Collaboration, S. Perlmutter et al., Measurements of Omega and Lambda from 42 High-Redshift Supernovae, Astrophys. J. 517 (1999) 565–586, [astro-ph/9812133].
22. Supernova Search Team Collaboration, A. G. Riess et al., Observational Evidence from Supernovae for an Accelerating Universe and a Cosmological Constant, Astron. J. 116 (1998) 1009–1038, [astro-ph/9805201].
23. Supernova Cosmology Project Collaboration, M. Kowalski et al., Improved Cosmological Constraints from New, Old and Combined Supernova Datasets, Astrophys. J. 686 (2008) 749–778, [0804.4142].
24. PAMELA Collaboration, O. Adriani et al., Observation of an anomalous positron abundance in the cosmic radiation, 0810.4995.
25. The Fermi LAT Collaboration, A. A. Abdo et al., Measurement of the Cosmic Ray e+ plus e- spectrum from 20 GeV to 1 TeV with the Fermi Large Area Telescope, 0905.0025.

26. J. Chang et al., An excess of cosmic ray electrons at energies of 300.800 GeV, Nature 456 (2008) 362–365.
27. H.E.S.S. Collaboration, F. Aharonian et al., The energy spectrum of cosmic-ray electrons at TeV energies, Phys. Rev. Lett. 101 (2008) 261104, [0811.3894].
28. H.E.S.S. Collaboration, F. Aharonian, Probing the ATIC peak in the cosmic-ray electron spectrum with H.E.S.S, 0905.0105.
29. D. P. Finkbeiner, Microwave ISM Emission Observed by WMAP, Astrophys. J. 614 (2004) 186–193, [astro-ph/0311547].
30. G. Dobler, D. P. Finkbeiner, I. Cholis, T. R. Slatyer, and N. Weiner, The Fermi Haze: A Gamma-Ray Counterpart to the Microwave Haze, 0910.4583.
31. M. Pospelov and A. Ritz, Astrophysical Signatures of Secluded Dark Matter, Phys. Lett. B671 (2009) 391–397, [0810.1502].
32. J. Hisano, S. Matsumoto, and M. M. No jiri, Explosive dark matter annihilation, Phys. Rev. Lett. 92 (2004) 031303, [hep-ph/0307216].
33. J. March-Russell, S. M. West, D. Cumberbatch, and D. Hooper, Heavy Dark Matter Through the Higgs Portal, JHEP 07 (2008) 058, [0801.3440].
34. M. Cirelli, M. Kadastik, M. Raidal, and A. Strumia, Model-independent implications of the e+, e-, anti-proton cosmic ray spectra on properties of Dark Matter, Nucl. Phys. B813 (2009) 1–21, [0809.2409].
35. I. Cholis, G. Dobler, D. P. Finkbeiner, L. Goodenough, and N. Weiner, The Case for a 700+ GeV WIMP: Cosmic Ray Spectra from ATIC and PAMELA, 0811.3641.
36. I. Cholis, D. P. Finkbeiner, L. Goodenough, and N. Weiner, The PAMELA Positron Excess from Annihilations into a Light Boson, 0810.5344.
37. Y. Cui, D. E. Morrissey, D. Poland, and L. Randall, Candidates for Inelastic Dark Matter, JHEP 05 (2009) 076, [0901.0557].
38. A. Sommerfeld Ann. Phys. 11 (1931) 257.
39. O. Adriani et al., A new measurement of the antiproton-to-proton flux ratio up to 100 gev in the cosmic radiation, 0810.4994.
40. D. Alves, S. R. Behbahani, P. Schuster, and J. G. Wacker, Composite Inelastic Dark Matter, 0903.3945.
41. D. Tucker-Smith and N. Weiner, Inelastic dark matter, Phys. Rev. D64 (2001) 043502, [hep-ph/0101138].
42. S. Chang, G. D. Kribs, D. Tucker-Smith, and N. Weiner, Inelastic Dark Matter in Light of DAMA/LIBRA, 0807.2250.

43. R. Bernabei et al., Dark matter particles in the galactic halo: Results and implications from DAMA/NaI, Int. J. Mod. Phys. D13 (2004) 2127–2160, [astro-ph/0501412].

44. DAMA Collaboration, R. Bernabei et al., First results from DAMA/LIBRA and the combined results with DAMA/NaI, Eur. Phys. J. C56 (2008) 333–355, [0804.2741].

45. A. W. Strong et al., Gamma-ray continuum emission from the inner Galactic region as observed with INTEGRAL/SPI, Astron. Astrophys. 444 (2005) 495, [astro-ph/0509290].

46. D. P. Finkbeiner and N. Weiner, Exciting Dark Matter and the INTEGRAL/SPI 511 keV signal, Phys. Rev. D76 (2007) 083519, [astro-ph/0702587].

47. M. Pospelov, Secluded U(1) below the weak scale, 0811.1030.

48. Muon G-2 Collaboration, G. W. Bennett et al., Final report of the muon E821 anomalous magnetic moment measurement at BNL, Phys. Rev. D73 (2006) 072003, [hep-ex/0602035].

49. The BABAR Collaboration, B. Aubert, Search for Dimuon Decays of a Light Scalar in Radiative Transitions Y(3S) → γ A0, 0902.2176.

50. KTeV Collaboration, E. Abouzaid et al., Measurement of the rare decay pi0→e+ e-, Phys. Rev. D75 (2007) 012004, [hep-ex/0610072].

51. M. Reece and L.-T. Wang, Searching for the light dark gauge boson in GeV-scale experiments, 0904.1743.

52. B. Batell, M. Pospelov, and A. Ritz, Exploring Portals to a Hidden Sector Through Fixed Targets, Phys. Rev. D80 (2009) 095024, [0906.5614].

53. Bossi, F., private communication

54. M. Pospelov, Secluded U(1) below the weak scale, 0811.1030.

55. J.D. Bjorken et.al., "Search for Neutral Metastable Penetrating Particles Produced in the SLAC Beam Dump", Phys. Rev. D38, 1988, 3375.

56. E.M. Riordan et.al., "A Search for Short Lived Axions in an Electron Beam Dump Experiment", Phys. Rev. Lett., 59, 1987, 755.

57. A. Bross et.al., "A Search for Shortlived Particles Produced in an Electron Beam Dump", Phys. Rev. Lett., 67, 1991, 2942-2945.

58. R. Essig, P. Schuster, N. Toro, B. Wojtsekhowski, "An Electron Fixed Target Experiment to Search for a New Vector Boson A' Decaying to e+e-", arXiv:1001.2557.

59. M. Freytsis, G. Ovanesyan, J. Thaler, "Dark Force Detection in Low Energy e-p Collisions", [arXiv: 0909.2862] JHEP 1001 (2010) 111.

3 Signal and Backgrounds

3.1 Heavy Photon Signal

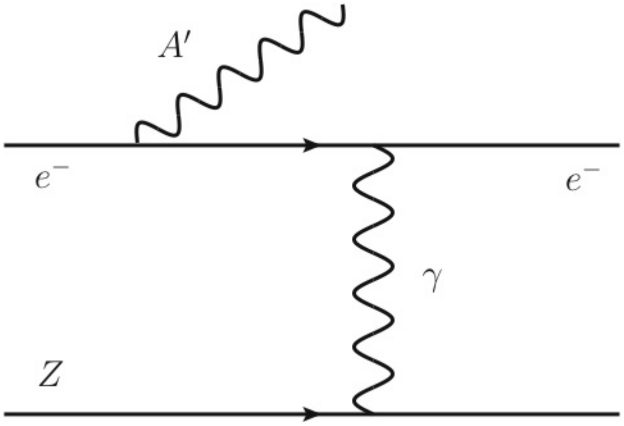

Figure 3.1.1 A' production by bremsstrahlung off an incoming electron as it scatters on a nucleus with atomic number Z.

A' particles are generated in electron collisions on a fixed target by a process analogous to ordinary photon bremsstrahlung, see Figure 3.1.1. This can be reliably estimated in the Weizsäcker-Williams approximation (see [1-4]). When the incoming electron has energy E_0, the differential cross-section to produce an A' of mass $m_{A'}$ with energy $E_{A'} \equiv x\, E_0$ is

$$\frac{d\sigma}{dx\, d\cos\theta_{A'}} \approx \frac{8\, Z^2\alpha^3\epsilon^2 {E_0}^2 x}{U^2}\, \tilde{\chi} \times \left[\left(1 - x + \frac{x^2}{2}\right) - \frac{x(1-x){m_{A'}}^2\, {E_0}^2 x\, {\theta_{A'}}^2}{U^2}\right] \qquad (3.1)$$

where Z is the atomic number of the target atoms, $\alpha \simeq 1/137$, $\theta_{A'}$ is the angle in the lab frame between the emitted A' and the incoming electron,

$$U(x,\theta_{A'}) = {E_0}^2 x {\theta_{A'}}^2 + {m_{A'}}^2 \tfrac{1-x}{x} + {m_e}^2 x \qquad (3.2)$$

is the virtuality of the intermediate electron in initial-state bremsstrahlung, and $\tilde{\chi}$ is the Weizsäcker-Williams effective photon flux, with an overall factor of Z^2 removed. The form of $\tilde{\chi}$ and its dependence on the A' mass, beam energy, and target nucleus are discussed in [1]. For HPS with E_0 = 5.5 GeV, we find $\tilde{\chi}$ ~ 7 (4, 1) for $m_{A'}$ = 100 (200, 500) MeV/c^2. The above results are valid for

$$m_e \ll m_{A'} \ll E_0, \quad x\, {\theta_{A'}}^2 \ll 1$$

For $m_e \ll m_{A'}$, the angular integration gives

$$\frac{d\sigma}{dx} \approx \frac{8\,Z^2\alpha^3\epsilon^2 x}{{m_{A'}}^2}\left(1+\frac{x^2}{3\,(1-x)}\right)\tilde{\chi}\,. \qquad (3.3)$$

The rate and kinematics of A' radiation differ from massless bremsstrahlung in several important ways:

- **Rate:** The total A' production rate is controlled by $\alpha^3\epsilon^2/m_{A'}^2$. Therefore, it is suppressed relative to photon bremsstrahlung by $\sim \epsilon^2 m_e^2/m_{A'}^2$. Additional suppression from small $\tilde{\chi}$ occurs for large $m_{A'}$ or small E_0.
- **Angle:** A' emission is dominated at angles $\theta_{A'}$ such that $U(x,\theta_{A'}) \lesssim 2\,U(x,0)$ (beyond this point, wide-angle emission falls as ${\theta_{A'}}^4$. For x near its median value, the cutoff emission angle is

$$\theta_{A',\max} \sim \max\left(\frac{\sqrt{m_{A'}\,m_e}}{E_0}, \left({m_{A'}}/{E_0}\right)^{\frac{3}{2}}\right),$$

- which is parametrically smaller than the opening angle of the A' decay products, $\sim m_{A'}/E_0$. Although this opening angle is small, the backgrounds mimicking the signal (discussed in Section 3.2) dominate at even smaller angles.
- **Energy:** A' bremsstrahlung is sharply peaked at ≈ 1, where $U(x,0)$ is minimized. When an A' is produced, it carries nearly the entire beam energy. In fact the median value of $(1-x)$ is $\sim \max\left(\frac{m_e}{m_{A'}}, \frac{m_{A'}}{E_0}\right)$.

The latter two properties are quite important in improving signal significance, and are discussed further in Section 3.2.

Assuming the A' decays into Standard Model particles rather than exotics, its boosted lifetime is

$$l_0 \equiv \gamma\, c\tau \simeq \frac{(3\,E_{A'})}{\left(N_{eff} m_{A'}^2 \alpha\,\epsilon^2\right)} \simeq \frac{0.8\,cm}{N_{eff}}\left(\frac{E_0}{10\,GeV}\right)\left(\frac{10^{-4}}{\epsilon}\right)^2\left(\frac{100\,MeV}{\mathrm{m_{A'}}}\right)^2, \qquad (3.4)$$

where we have neglected phase-space corrections, and N_{eff} counts the number of available decay products. If the A' couples only to electrons, then $N_{eff}=1$. If the A' mixes kinetically with the photon, then $N_{eff}=1$ for $m_{A'} < 2m_\mu$ when only $A' \to e^+e^-$ decays are possible, and $2+R(m_{A'})$ for $m_{A'} \geq 2\,m_\mu$, where [5]

$$R = \left.\frac{\sigma(e^+e^- \to hadrons)}{\sigma(e^+e^- \to \mu^+\mu^-)}\right|_{E=m_{A'}}.$$

For the ranges of ε and $m_{A'}$ probed by this experiment, the mean decay length l_0 can be prompt or as large as tens of centimeters.

The total number of A' produced when N_e electrons scatter in a target of $T \ll 1$ radiation lengths is

$$N \sim N_e \frac{N_0 X_0}{A} T \frac{Z^2 \alpha^2 \epsilon^2}{m_{A'}{}^2} \tilde{\chi} \sim \; N_e C \, T \frac{\epsilon^2 \, m_e{}^2}{m_{A'}{}^2}, \qquad (3.5)$$

where X_0 is the radiation length of the target in g/cm², $N_0 \simeq 6 \times 10^{23} mole^{-1}$ is Avogadro's number, and A is the target atomic mass in g/mole. The numerical factor $C \approx 5$ is logarithmically dependent on the choice of nucleus (at least in the range of masses where the form-factor is only slowly varying) and on $m_{A'}$, because, roughly, $X_0 \propto \frac{A}{Z^2}$ (see [1,3,4]). For a Coulomb of incident electrons, the total number of A's produced is given by

$$N {\sim} 10^6 \left(\frac{N_e}{1\,C}\right) \tilde{\chi} \left(\frac{T}{0.1}\right) \left(\frac{\epsilon}{10^{-4}}\right)^2 \left(\frac{100\,MeV}{m_{A'}}\right)^2$$

The efficiency of the detector for detecting these A's is discussed in Section 5.

3.2 Radiative and Bethe-Heitler Trident backgrounds

The stark kinematic differences between QED trident backgrounds and the A' signal can be used to advantage to maximize the signal to background ratio. QED tridents dominate the final event sample, so we consider their properties in some detail here.

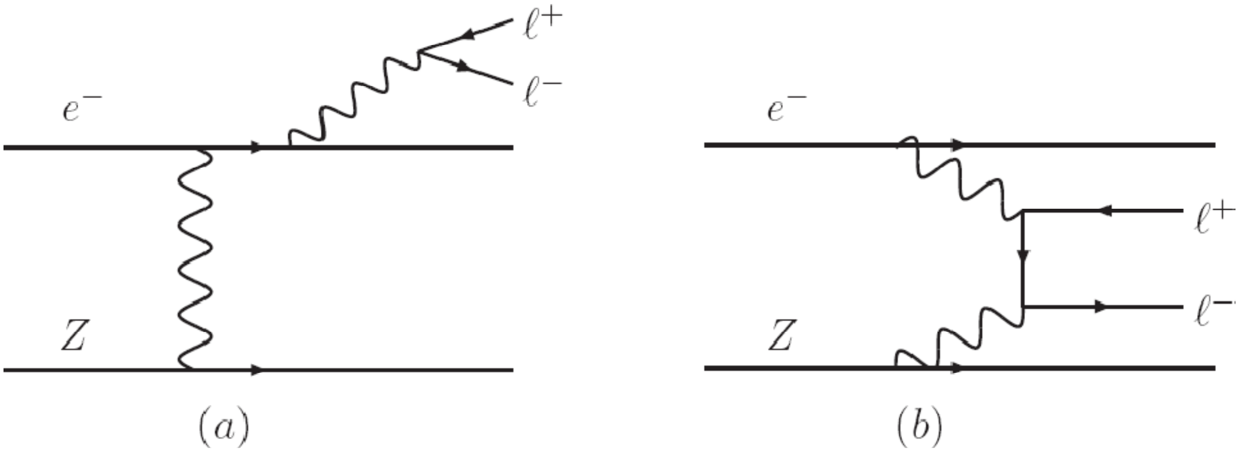

Figure 3.2.1: Sample diagrams of (a) radiative trident (γ*) and (b) Bethe-Heitler trident reactions that comprise the primary QED background to A' → ℓ+ℓ- search channels.

The irreducible background rates are given by the diagrams shown in Figure 3.2.1. These trident events can be usefully separated into "radiative" diagrams (Figure 3.2.1 (a)), and "Bethe-Heitler" diagrams (Figure 3.2.1 (b)), that are separately gauge-invariant (we discuss the simulation of the QED trident background events in Section 6).

The contribution from the radiative diagrams (Figure 3.2.1 (a)) alone is also useful as a guide to the behavior of A' signals at various masses. Indeed, the kinematics of the A' signal events is identical to the distribution of radiative trident events restricted in an invariant mass window near the A' mass. Moreover, the rate of the A' signal is simply related to the radiative trident cross-section within the spectrometer acceptance and a mass window of width δm by [4]

$$\frac{d\sigma\left(e^- Z \rightarrow e^- Z(A' \rightarrow \ell^+ \ \ell^-)\right)}{d\sigma\left(e^- Z \rightarrow e^- Z(\gamma * \rightarrow \ell^+ \ \ell^-)\right)} = \frac{3\pi\epsilon^2}{2\,N_{eff}\alpha}\,\frac{m_{A'}}{\delta m}\,, \qquad (3.6)$$

where N_{eff} counts the number of available decay products. This exact analytic formula was also checked with a MC simulation of both the A' signal and the radiative trident background restricted to a small mass window δm, and we find nearly perfect agreement. Thus, the radiative subsample can be used to analyze the signal, which simplifies the analysis considerably.

It is instructive to compare kinematic features of the radiative and Bethe-Heitler distributions, as the most sensitive experiment maximizes acceptance of radiative events and rejection of Bethe-Heitler tridents. Although the Bethe-Heitler process has a much larger total cross-section than either the signal or the radiative trident background, it can be significantly reduced by exploiting its very different kinematics. In particular, the A' carries most of the beam energy (see discussion in Section 3.1), while the recoiling electron is very soft and scatters to a wide angle. In contrast, the Bethe-Heitler process is not enhanced at high pair energies. Moreover, Bethe-Heitler processes have a forward singularity that strongly favors asymmetric configurations with one energetic, forward electron or positron and the other constituent of the pair much softer.

These properties are discussed further in the Appendix of [4], and illustrated in Figure 3.2.2.

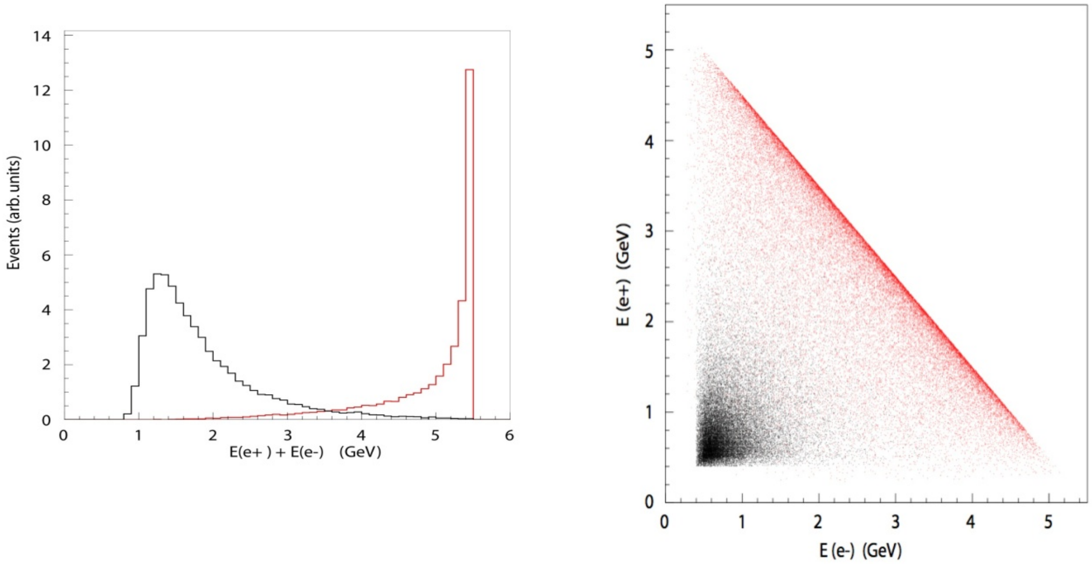

Figure 3.2.2: Left: The distribution of Bethe-Heitler background events (black) and A' signal events (red) as a function of the sum of the electron and positron energy. Note that the signal is peaked at high energies,

while the background is peaked at much lower energies. Right: The distribution of the positron versus electron energy for Bethe-Heitler background events (black dots) and A' signal events (red dots). Note that in both plots neither the signal nor background events have been normalized to the correct number. In reality, the number of background events is much larger than the number of signal events. Also, note that the electron energy here refers to the energy of the electron produced in the reaction, not the recoiling beam electron.

3.3 Beam Backgrounds

The experimental requirements of a high beam current and a large forward detector coverage conspire to make beam backgrounds a significant challenge in the design of the experiment. The multiple Coulomb scattering and bremsstrahlung processes in the target will generate high intensity fluxes of electrons and photons in the very forward direction, while the large Moller interaction cross section with atomic electrons will generate high intensity low energy electrons. The beam backgrounds are simulated using the high energy interaction simulation codes, EGS5 and Geant4.

The beam backgrounds determine a "dead zone" where the high intensity particle flux must be avoided to eliminate secondary particle production and extensive radiation damage in the detectors. All the detector components must be placed outside of the dead zone. To determine its extent, we have considered the detector occupancy and radiation tolerance in the Si tracker, and the trigger rate and radiation tolerance in the electromagnetic calorimeter. Multiple Coulomb scattering in the target increases the primary beam size and angular divergence as it passes through the apparatus, and limits how closely detector elements can be placed to the beam. As the rms scattering angle is $<\theta> \sim \sqrt{T}/E_0$, a thinner target and/or higher energy beam can minimize the dead zone. When the target thickness is reduced, however, the beam current (I) must be increased proportionately in order to maintain the A′ production rate, $T \cdot I$. See Section 5.2 for details.

An additional process that yields high-energy electron-positron pairs is the "two-step" (or incoherent) trident production, consisting of a high-energy bremsstrahlung photon emission followed by the e^+e^- conversion inside the target. As this is a two-step process, the production rate is proportional to T^2. This process has been simulated using EGS5. The rate becomes comparable to that of the radiative trident background described above for a 1% X_0 tungsten target, and is significantly less for the target thicknesses proposed for this experiment.

3.4 References

1. K.J Kim and Y.-S. Tsai, "Improved Weizsacker-Williams methos and its application to lepton and W-boson pair productions", Phys. Rev. D8, 1973, 3109.
2.] J. Alwall et.al., "MadGraph/MadEvent v4: The New Web Generation", JHEP, 09, 2007, 028, arXiv: 0706.2334.

3. R. Essig, P, Schuster, N. Toro, and B. Wojtsekhowski, "An Electron Fixed Target Experiment to Search for a New Vector Boson A' Decaying to e+e-", arXiv: 1001.2557.

4. J.D. Bjorken, R. Essig, P. Schuster, and N. Toro, "New Fixed-Target Experiments to Search for Dark Gauge Forces", Phys. Rev. D80, 2009, 075018, arXiv: 0906.0580.

4 Experimental Setup

4.1 Overview

Sensitivity to dark photons relies upon the precision measurement of two quantities in this experiment: the invariant mass of the A′ decay products and the position of the decay vertex. By placing a tracking and vertexing detector immediately downstream of the target inside an analyzing magnet, one obtains the complete kinematic information required for A′ reconstruction from a single system, whose proximity to the target naturally maximizes the acceptance of a relatively compact detector and provides excellent momentum and vertexing resolution.

Placing the planes of the tracker immediately downstream of the target means that the intense primary beam must pass directly through the middle of the tracking detector. There are two key consequences of this arrangement. First, scattered beam particles and radiative secondaries are bent by the magnetic field to sweep out a “dead zone” where the particle fluxes would be damaging to the sensors as well as creating an environment too dense for pattern recognition. This necessitates a tracking geometry that keeps the sensors out of this region. However, since the energy released in the decay of low mass A′ is small relative to their boost, the opening angle between decay daughters can be quite small. Therefore, in order to maximize the acceptance for low masses, the size of the dead zone must be minimized. Second, interactions of the primary beam with air or even helium at atmospheric pressure gives rise to low-momentum secondaries that generate unacceptable occupancies in the detector. The only way to keep the beam in a vacuum without severely compromising acceptance and vertex resolution is to enclose the entire tracking and vertexing system within a vacuum chamber as well. The background environment and the high spatial precision required for good momentum and vertexing resolution make silicon sensors the obvious choice in this region.

High luminosities are needed to search for heavy photons with small couplings and masses in the 100MeV range. HPS, utilizing CEBAF’s essentially continuous duty cycle, can simultaneously maximize luminosity and minimize backgrounds by employing detectors with short livetimes and rapid readout. Silicon tracking sensors are ideal from this perspective, since they collect ionization in 10’s of nanoseconds and produce pulses as short as 50-100 nanoseconds. Thanks to electronics developed for the LHC, the sensors can be read out continuously at 40 MHz.

The electromagnetic calorimeter just downstream of the tracker uses detectors with comparably short livetimes and high rate capability, and performs two essential functions for the experiment: triggering and electron identification. The device is highly segmented. It is fast, able to readout at rates comparable to those in the tracker, and able to provide good spatial and energy information to the trigger electronics. Like the tracker system, the electromagnetic calorimeter is split to avoid impinging on the "dead zone". The beam and radiative secondaries pass through the calorimeter in vacuum, to avoid generating unnecessary backgrounds.

The muon detector also has fast response, will be readout rapidly, and will be used to trigger on candidate tracks which pass through ~ 1m iron. It provides an independent trigger, with very different systematics, for A' masses above about 300 MeV/c^2 , and a unique window on A' dimuon decays. The beam will pass through the middle of the detector in vacuum, and eventually be transported to the B-line dump.

Below, we discuss the various elements of the experiment in more detail, beginning with the beamline, continuing with the tracker/vertexer, electromagnetic calorimeter, and muon system, and concluding with the electronics and DAQ.

4.2 Beamline Elements

4.2.1 Layout

The HPS experiment will utilize a setup located behind the CLAS detector, in the downstream alcove of Hall B, shown in Figure 4.2.1.1. The setup will be based on a three-magnet chicane, the second dipole magnet serving as the analyzing magnet. The dipole field direction (Y) will be perpendicular to the horizontal (XZ) plane. A Hall B "Frascati" H magnet will be used (pole length 50 cm, max-field 1.2 T) as the first dipole of the chicane. For a 25 mradian deflection (to beam's left) and at 5.5 GeV, the integrated strength required is 0.459 T-m. The analyzing magnet will be an 18D36 H-magnet from SLAC (pole length 91.44 cm, max-field 1.15 T) with the gap increased to 14 inches. The integrated strength for a 50 mradian deflection (right) is 0.917 T-m. As the last magnet of the chicane, the C-magnet located in the downstream tunnel (the old pair spectrometer of Hall B) will be used. It will deflect the beam 25 mradians to the left and has an integrated strength of 0.459 T-m.

The detector package will include multiple layers of silicon detectors, mounted inside the vacuum box in the high field region of the analyzing magnet. They are described in Section 4.3 below. Downstream of the analyzing magnet there will be electromagnetic calorimeter, for triggering and electron and positron identification (see Section 4.4), and multiple layers of scintillation hodoscopes sandwiched between iron absorbers for muon identification (See Section 4.5). The target foil will be positioned at the beginning of the high field region of the analyzing dipole. The distance from the target to the first layer of the silicon tracker will be 10 cm. The distance from the target to the face of the electromagnetic calorimeter is ~130 cm. The whole length of the setup from the target to the end of the muon hodoscope system is approximately 350 cm.

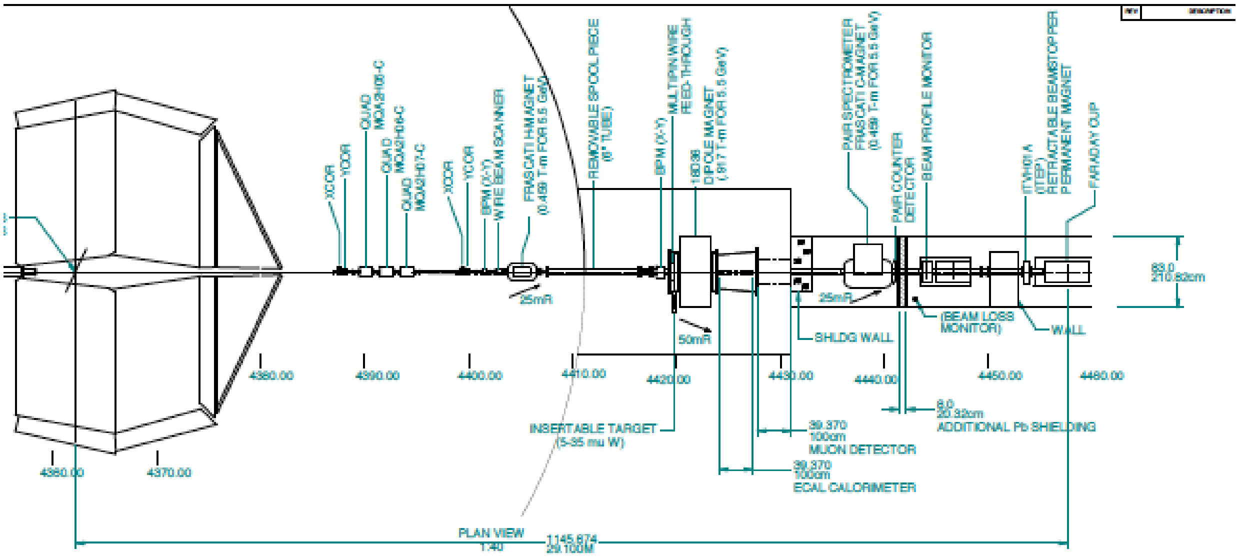

Figure 4.2.1.1. Layout of the HPS experimental setup behind the CLAS detector in Hall B.

4.2.2 Running Conditions

Production data taking will use a five-pass-beam, at ~5.5 GeV energy, incident on a tungsten (W) target. The proposed luminosity for production running is 1.4×10^{32} cm^{-2} s^{-1} per nucleus. This luminosity will be achieved using electron beam currents of 100nA to 700nA, and tungsten or tantalum target foil thicknesses from 5μm (0.14% RL) to 35μm (1% RL). The high intensity electron beam incident on the tungsten target will generate a significant amount of electromagnetic radiation, composed mainly of bremsstrahlung photons, electrons which have radiated, Moller electrons, and beam particles which have multiple Coulomb scattered. In the dipole field, this radiation will create a "sheet of flame" in the bending plane (XZ), at the beam height, $Y \approx 0$. Detectors will be positioned above and below the beam plane, leaving a small gap for the bremsstrahlung and Moller background to pass through. The gap between the up and down planes of the first layer of the silicon tracker will be ±15 mrad as seen from the target location (approximately ±1.5mm). The beam is very clean, and is contained within $Y=\pm 1$mm, so it passes through the "dead zone" gap. The beam halo is at the level of 10^{-5} and extends to ±2mm as seen in Figure 4.2.2.1.

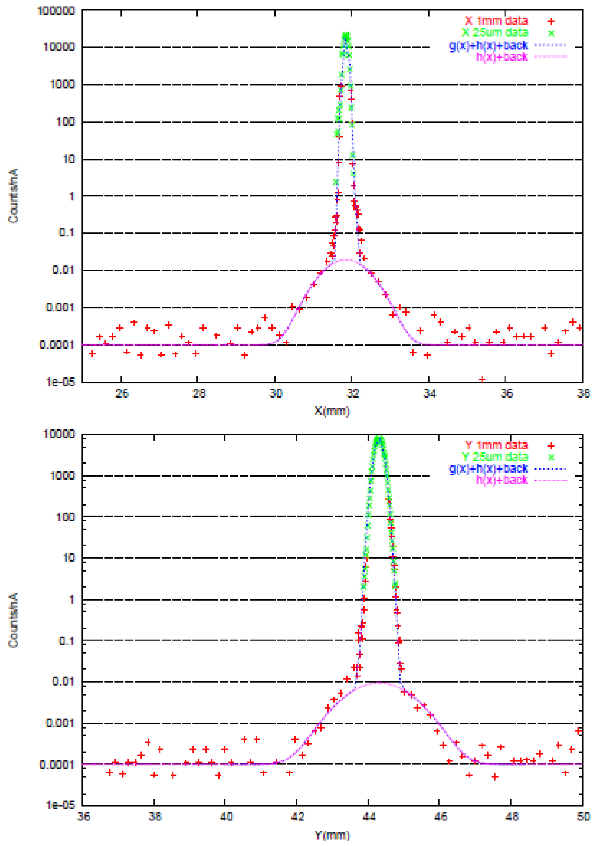

Figure 4.2.2.1: Hall B 6GeV beam profile measured in large dynamic range profile measurement. Figure taken from A.P. Freyberger Proceeding of the 2003 Particle Accelerator Conference 0-7803-7739-9 ©2003 IEEE.

The gap between the up and down parts of the electromagnetic calorimeter will be about ±15 mm. The beam will be terminated in the Hall B electron beam dump. The transport beam line to the dump will be in vacuum. The electron beam will have clear passage to the dump when the chicane is OFF. The proposed running conditions and the close proximity of detector elements to the beam line impose tight constraints on the beam profile quality. The HPS beam parameter requirements are presented in Table 4.2.2.1.

Parameter	Requirement/expectation	Unit
E	5562	MeV
$\delta p/p$	$< 10^{-4}$	
Current	> 100 (< 1000)	nA
Current instability	< 5	%

Parameter	Requirement/expectation	Unit
σ_x	< 50	μm
σ_y	< 50	μm
Position stability	< 50	μm
Divergence	< 100	μrad

Table 4.2.2.1 Required beam parameters.

4.2.3 **Beamline Proposal**

The proposed HPS target location is approximately 18.6 m downstream of the nominal CLAS target location. This location requires that the optics be altered to account for the new location of the experimental target. We have considered two options for the beamline design. In the first option, we use the existing Hall-B beamline to achieve a focus at the new HPS target location, making use of the triplet of quadrupole magnets 25 m upstream of the nominal CLAS target. The following section presents the results of this approach, followed by a section on beam diagnostics and trajectory control. We describe the second option below in Section 4.2.3.2.

4.2.3.1 **Option One: Use Existing Hall- B Beamline**

This section describes the results of optimizing the existing Hall-B beamline to achieve a focus at the proposed HPS target location. The approach is to use the quadrupole magnets upstream of the Goniometer/Moller systems to increase the beam β values in the region of the final focusing triplet. The final quadrupole triplet is then used to achieve a minimum β (or beam size) at the HPS target.

The locations of the HPS chicane and other elements used in the optics development are given in Table 4.2.3.1. The Hall-B *elegant* deck has been modified to include these new elements for this study. The deck does not include diagnostic elements or correctors at this time.

What	Distance in Z (m)	ΔZ(m)	Other info.	Deck name
CLAS nominal target	0	0		ETA2HCLAS
End of Forward Carriage	8.07	0		
First dipole	15.41	1	25 mrad	MBX2H90

What	Distance in Z (m)	ΔZ(m)	Other info.	Deck name
Target	18.35	0.25		ETA2HTEST
Second dipole	19.2	1	50 mrad	MBX2H91
Third dipole	23.23	1.5	25 mrad	MBX2H92
Faraday Cup	28.95	0		IFY2D00

Table 4.2.3.1 Elements used in optics development.

The optics program *elegant* is used to determine the optimized element parameters for HPS. The optimization required that β_x and β_y be less than 400 μm throughout the line and that β_x and β_y are at a minimum at the HPS target (minimum beam size). An emittance, ε , of $2\text{x}10^{-9}$ m-rad is used as input. This is a factor of two larger than ε_{design}; this represents a $\sqrt{2}$ safety factor on beam size.

In order to achieve $\varepsilon = 2\text{x}10^{-9}$ m-rad the CEBAF accelerator must be well matched and the Hall-B line must be properly matched at the start of the line. There exists a wire scanner and matching quadrupole magnets at the start of the Hall-B line explicitly for this purpose. The process of matching the Hall-B line is rarely invoked as empirical tuning suffices to achieve the experimental requirements.

The horizontal and vertical beam size plot for the entire Hall-B beam line is shown in Figure 4.2.3.1 and values for key parameters are given in Table 4.2.3.2. A beam size of ~40 μm in both horizontal and vertical planes has been achieved.

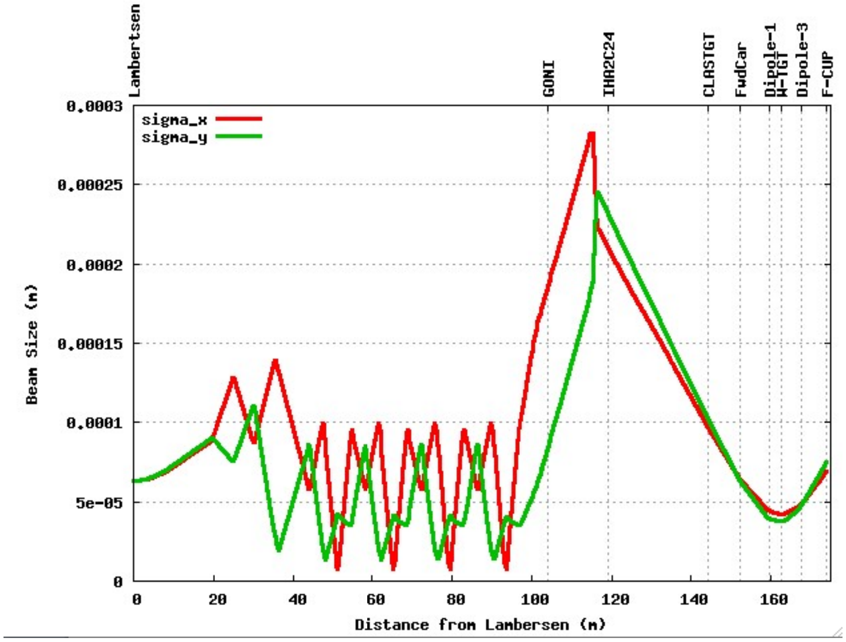

Figure 4.2.3.1. The horizontal (red) and vertical (green) beam size along the HPS beam line in Hall B

Distance (m)	σ_x (μm)	σ_y (μm)	Deck name
119.16	210	231	IHA2C24
144.17	97	102	ETA2HCLAS
162.77	42	38	ETA2HTEST

Table 4.2.3.2 Beam size for entire Hall B beam line for HPS experiment.

4.2.3.2 **Option Two: Modify Hall-B Beamline for HPS**

Adding additional quadrupole magnets to the Hall-B beamline will reduce the beam size at the HPS target. This is advantageous for the experiment because it will allow decay angles to be measured with greater precision and will also improve the vertex definition by adding the additional constraint of the A′ trajectory. There is enough physical space to add more quadrupole magnets either between the tagger magnet and CLAS or between the Forward Carriage and the HPS chicane.

Results from the optics program *elegant* for the horizontal and vertical beam sizes with three additional quadrupoles located on the Forward Carriage are shown in Figure 4.2.3.2. With additional quadrupoles, a beam size of ~10 μm with 20-30 μrad beam divergence can be achieved at the HPS target as shown in Figure 4.2.3.3. For lower beam energies the beam size at the HPS target will be slightly bigger, e.g. 30% bigger for 3 pass beam (3.3 GeV).

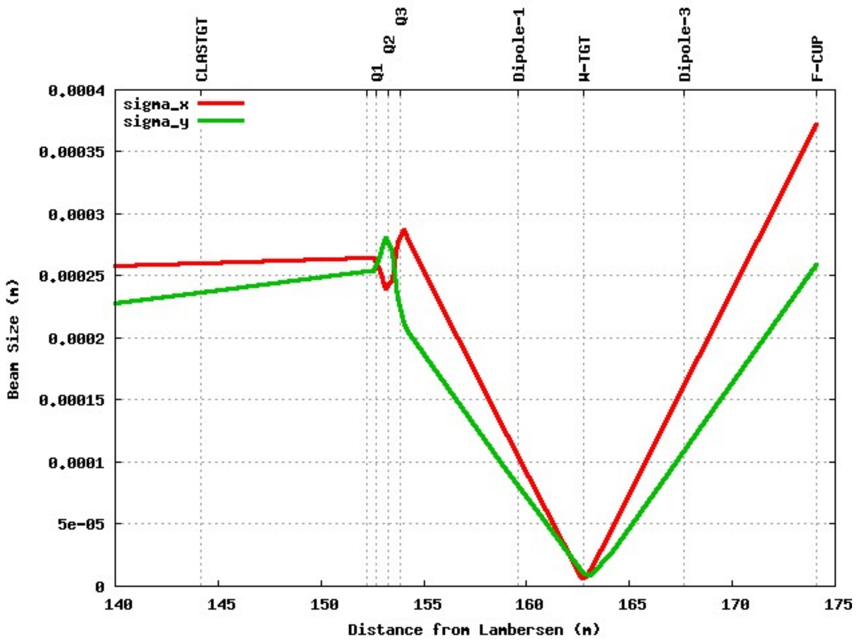

Figure 4.2.3.2. Beam sizes, X and Y, from CLAS center to Faraday Cup with additional quadupoles at forward carriage.

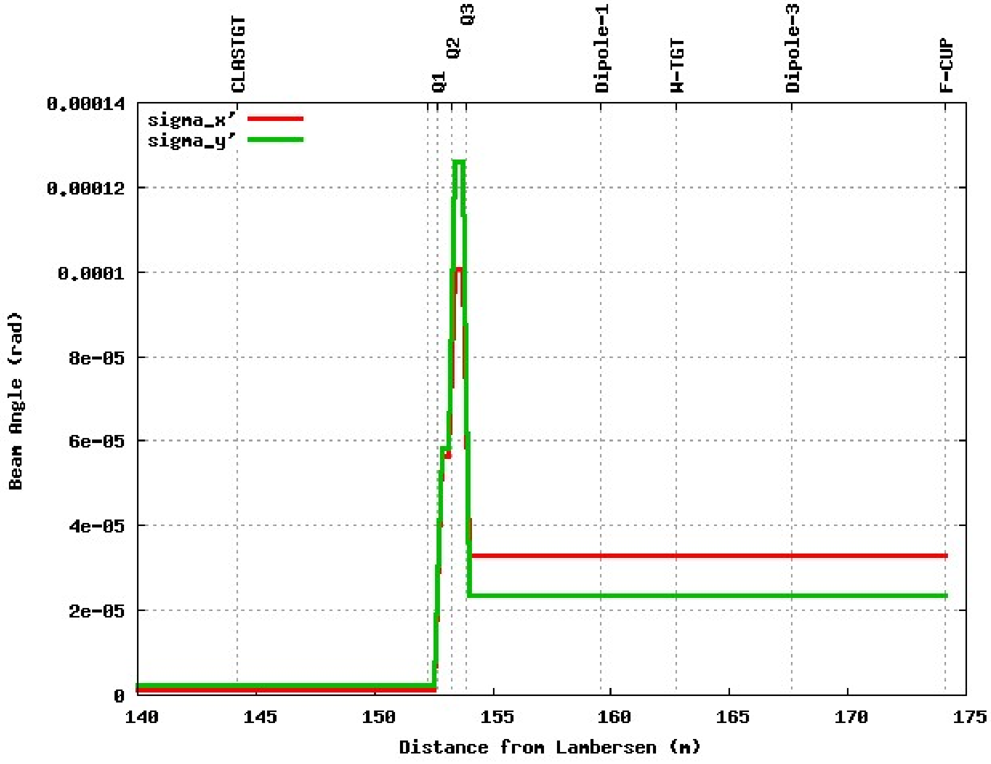

Figure 4.2.3.3. Beam divergence at the HPS setup region.

4.2.3.3 **Diagnostics and Trajectory Control**

Hall-B experiments typically require nA-level beam currents. Measuring beam positions with such small beam currents is difficult; presently Hall-B relies on three sets of cavity beam position monitors (BPM). These monitors are physically large and rather slow. The large (100+ nA) beam currents envisioned for the HPS experiments allows the use of the standard CEBAF antenna BPM cans with transport style electronics. The use of antenna BPMs for the HPS experiment will reduce the space/cost of beam position measurements. The antenna BPM ``cans'' come in two sizes, M15 and M20. The M15 has a standard 2-3/4" flange and is usually associated with 1" or 1.5" beam tubes. The M20 BPM has a 4-5/8" flange and is usually associated with 2" to 3" beam tube. The BPM measured position is linear within about ±7 mm of the electric center of the BPM can.

Adding M15 and/or M20 to the HPS beamline will allow for the beam position to be measured in a straightforward manner. A pair of BPMs upstream of the first dipole will define the incoming trajectory. It might be possible to locate a M20 or M15 on the chicane path just upstream of the target. This would allow for knowledge of the beam position at the target. Trajectory control of the incident beam will require at least four correctors (two horizontal and two vertical) between the forward carriage and the first dipole. Presently there exists a vertical and horizontal corrector in the bore of the Forward Carriage tube. These correctors are presently not used but might be of use for HPS.

The three dipoles which form the chicane might not be on bi-polar supplies so it will not be possible to degauss them easily. Therefore a corrector should be associated with each of these magnets so that any remnant field can be ``nulled'' out to achieve a straight-ahead trajectory. The strengths of these correctors are to be determined.

4.2.4 **Targets**

A selection of target foils will be available. They will be mounted on a horizontal plate of machinable ceramic or carbon fiber material, as shown in Figure 4.2.4.1. The plate will be moved transversely to the beam line, so that a single target is in use at a time. The positioning mechanism will be a vacuum- and magnetic-field-compatible piezo-electric actuator, for example an inch-worm system.

Thin tungsten foils will be used. High Z material is chosen to minimize the hadronic production relative to the trident and A′ production, since the ratio of QED to hadronic processes goes as (Z^2/A). A set of targets will be located 10 cm in front of the first plane of silicon strip detectors. The primary target will be 0.25% of a radiation length (approximately 9 microns tungsten), and foils of 0.1% and 1% can also be moved on to the beam line. A beam scintillation screen of BeO or YAG may also be mounted with this set, and selectable for beam diagnostics. This would require a window in the vacuum chamber and a camera. On the same mounting plate, but only 5 cm in front of the silicon strips, will be another foil of 0.25% radiation lengths. This target will be mounted so that it does not intercept A′ decay tracks that would be accepted from the foils at 10 cm.

The foils will be no greater than 1 cm square, and so the total transverse motion required to select any one of the targets, or to allow the beam to pass through without interacting, will be less than 10 cm. It is intended that fixturing to maintain rigidity in the foils will be thin enough that it will be possible to move between targets without turning off the beam. The 10 cm transverse range retains the flexibility to install additional targets for systematics studies or evolving physics considerations. An example is a set of three carbon foils, each about 150 microns thick, spaced at 2.5 cm intervals along the beam axis, which could be used to search for muonium production and decay.

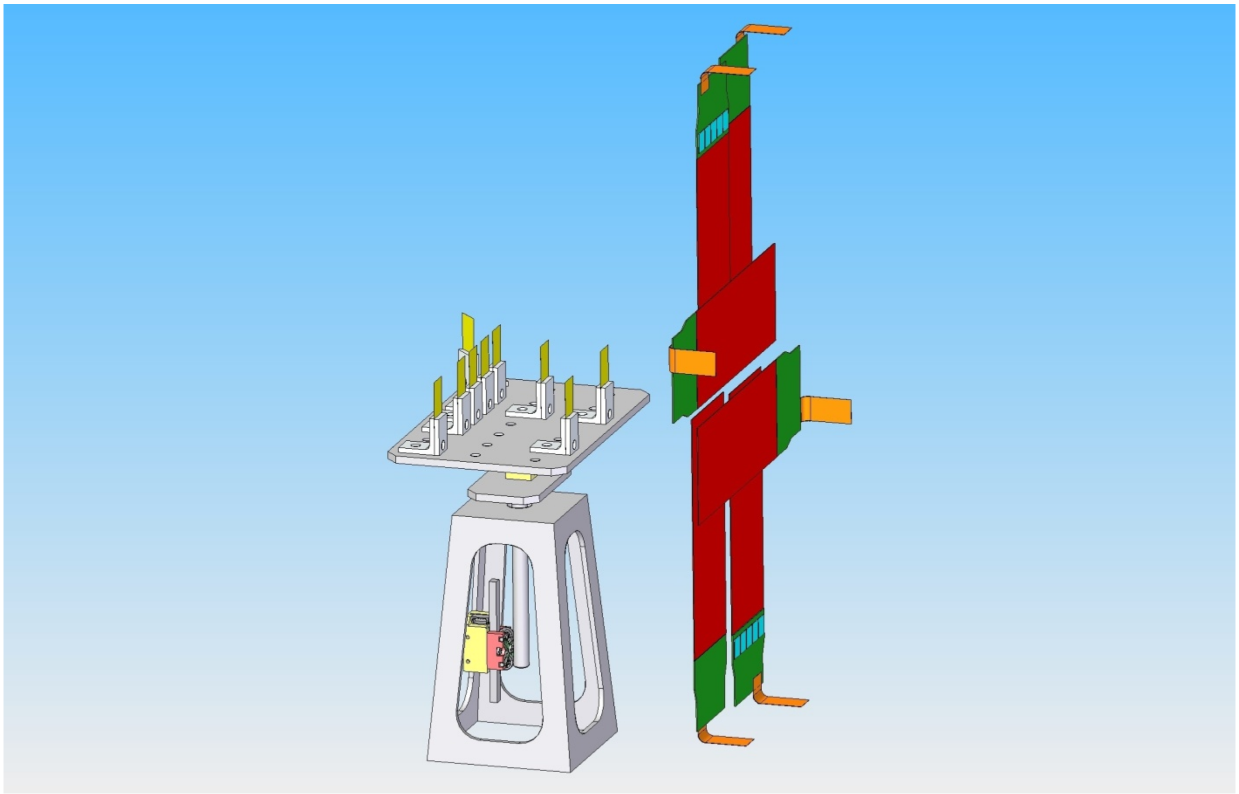

Figure 4.2.4.1. Movable target mechanism and target foils in front of the first silicon detector layers.

4.3 Tracking and Vertexing System

4.3.1 Design Considerations

At the beam energies necessary to achieve sensitivity to A′ in the most interesting mass range, the decay products will be charged particles with momenta on the order of a few GeV/c. Consequently, multiple scattering dominates the measurement uncertainties for any feasible material budget. In particular, uncertainty in the mass determination and uncertainty in the vertex position are limited by the uncertainties in the directions of the A' decay products, which results from multiple Coulomb scattering in the first detector layers. As a result, for both the mass and vertexing resolutions, the radiation lengths of material must be minimized throughout the tracker. Doing so also results in the optimal momentum resolution and minimizes tracking pattern recognition errors in an environment of dense hits.

To minimize the impact of beam backgrounds, the tracker/vertexer is split into upper and lower half-planes which avoid the "dead zone" defined by the beam envelope and those electrons which have radiated in the target. To avoid secondary backgrounds which would arise from the passage of the beam through gas, the beam must be transported in vacuum, and the entire tracker/vertexer placed within a vacuum chamber.

Finally, the position and tails of the beam profile may not be exactly known, and there are significant uncertainties in the background estimates and the radiation tolerance of the sensors for the background environment. So it will be important to be able to adjust the position of the tracking planes in-situ, or even remotely. It is also sensible to provide for access to the tracker with minimal intervention, to accommodate repairs or replacement of tracking planes.

4.3.2 **Sensors**

Given a high density of hits that results in pattern recognition challenges, it is natural to consider pixellated sensors for this experiment. However, the occupancies per unit time are such that the only technology currently meeting the rate requirements is a hybrid pixel detector. This is not a feasible solution here, primarily because the power and cooling required in the tracking volume would result in a material budget that seriously compromises sensitivity. It is also likely that the cost and effort associated with development of a hybrid pixel system for the project makes it unachievable on the desired timescale. The simple, low-mass choice is silicon microstrips.

Cut Dimensions (L×W)	100 mm × 40.34mm
Active Area (L×W)	98.33 mm × 38.34mm
Readout (Sense) Pitch	60μm (30μm)
# Readout (Sense) Strips	639 (1277)
Depletion Voltage	$40V < V_{dep} < 300V$
Breakdown Voltage	>350V
Total Detector Current at 350V bias	<16 μA
Bias Resistor Value (both ends of strips)	0.8 ± 0.3 MΩ
AC Coupling Capacitance	>12 pF/cm
Total Interstrip Capacitance	<1.2 pF/cm
Defective Channels	<1%

Table 4.3.2.1: Specifications of sensors available for this experiment. Many of the sensors exceed the bias voltage and bad channel specifications by a significant margin.

The sensors must to be rectangular and as large as possible to cover a relatively large area with the smallest possible number of sensors. These sensors must also be of a radiation-tolerant design, have a relatively fine readout pitch to minimize occupancies and two-hit resolution and have a very small rate of defects. A sufficient supply of suitable sensors has been identified that meets all of these criteria, remaining from the cancelled Run IIb upgrades of the DØ and CDF detectors at the Tevatron. [1] These are p+ on n, single sided, AC coupled, polysilicon-biased sensors fabricated on <100> silicon. The relevant specifications of these sensors is shown in Table 4.3.2.1 While the specifications only ensure that these sensors may be operated up to 350V bias after irradiation, previous experience indicates that many of them will be operable to 1000V and therefore remain fully depleted to a dose of approximately 1.5×10^{14} 1MeV neq/cm^2. By testing and selecting those that withstand the highest bias voltage for use in the parts of the detector where the radiation field is most intense, the radiation tolerance of the detector can be maximized to allow a smaller dead zone and a longer running time before replacement of planes is necessary.

4.3.3 **Readout Electronics**

The extreme occupancies in the tracker demand the shortest possible readout integration time with the best possible time resolution. Since the development of a front-end readout chip is well beyond the scope of this experiment, existing front-end chips designed for the LHC tracking detectors are the obvious choices. Of these, the APV25, originally developed for use by the CMS tracker, is the most attractive option. [2] The relevant specifications of the chip are summarized in Table 4.3.3.1 and the layout of the chip is shown in Figure 4.3.3.1.

# Readout Channels	128
Input Pitch	44 μm
Shaping Time	50ns nominal (35ns min.)
Output Format	multiplexed analog
Noise Performance (multi-peak mode)	270+36×C(pF) e- ENC
Power Consumption	345 mW
Communication Protocol	I^2C

. **Table 4.3.3.1**: Specifications of APV25 Readout ASIC.

The first desirable attribute is excellent noise performance, largely due to the inherent properties of the 0.25μm fabrication process. High signal-to-noise ratio in the detector results in high single-hit efficiency with a low rate of noise hits and extremely good single-hit spatial resolution. Before irradiation, the signal-to-noise ratio with the previously described sensors will be approximately 34, resulting in full single hit efficiency with a negligible rate of noise hits. Single-hit resolution will be approximately 6.5 μm based upon test beam and simulation with similar sensors. [3] After irradiation, when noise increases and charge becomes lost to trapping centers and a shrinking depletion layer, the extra headroom in signal-to-noise will extend acceptable performance as long as possible and provide a period in which to identify the onset of failure well before replacement is necessary.

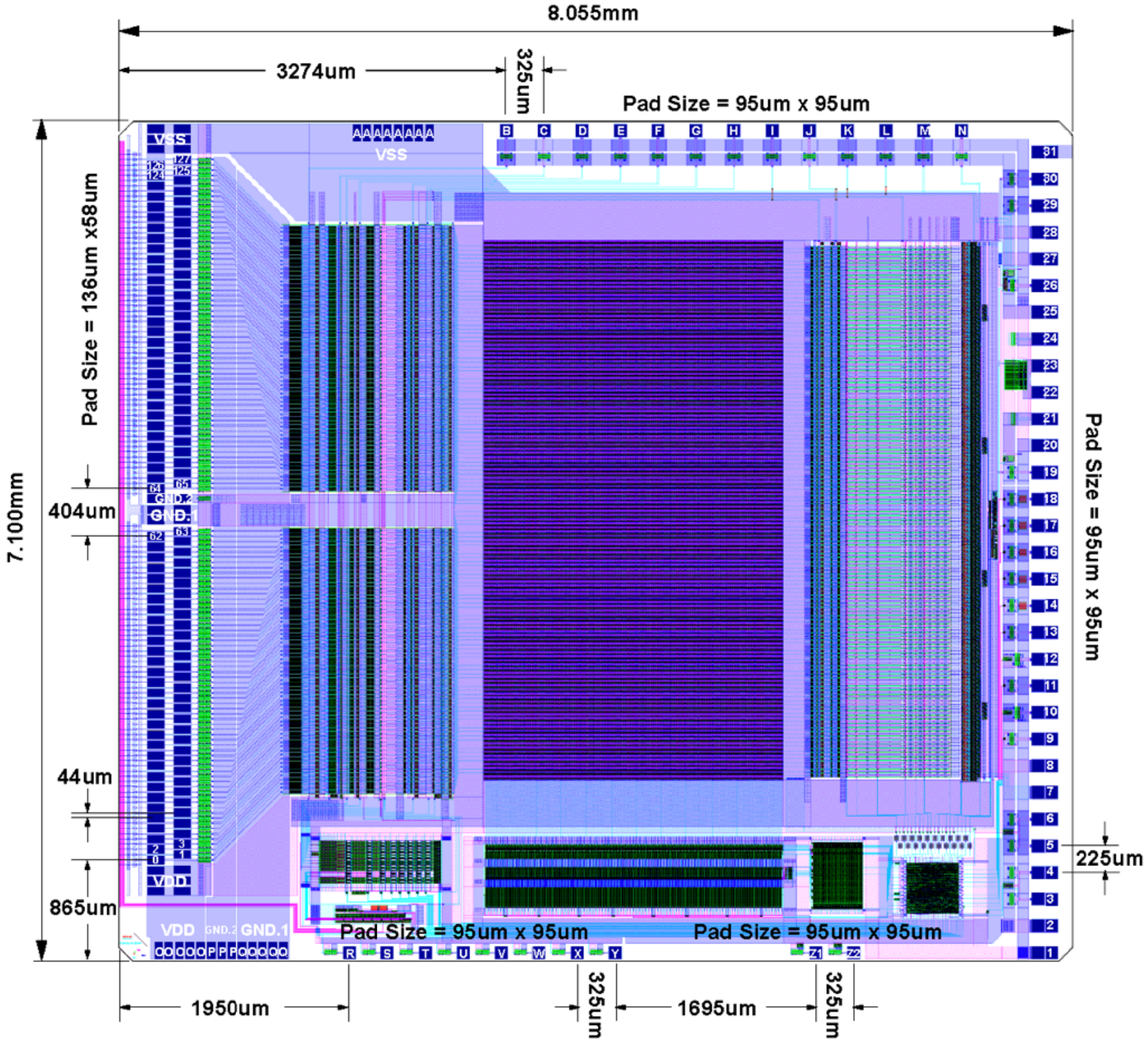

Figure 4.3.3.1: Layout of the APV25 Readout ASIC. The signal input pads are shown at left.

The second desirable attribute naturally arising from the 0.25 micron fabrication process is a high degree of radiation tolerance. Although the readout chips are expected to see much smaller doses than the hottest regions on the sensors, some chips will see doses that would result in performance degradation of chips that are less radiation tolerant.

Finally, and most importantly here, the APV25 has a flexible readout architecture, which can be used to improve the time resolution of the tracker. In addition to the standard readout modes employed at the LHC, the APV25 may be operated in “multi-peak” mode, in which the output of the shaper (with nominal shaping time of 50ns) is sampled at clock-synchronous 25ns intervals, in multiples of three samples, after a trigger is received. [4] Fitting the known form of the shaper output curve to these samples allows the determination of both the peak amplitude and the t0 of the hit. This technique has been developed extensively for the planned use of the APV25 chip for the upgrade of the Belle detector (Belle-II) for operation at Super-KEKB, which has a 2ns bunch spacing. Tests have shown that at S/N>25, the hit time may be reconstructed with an RMS of 2ns or better for the readout of three samples. [5]

Where occupancies are large relative to the decay of the shaper response, one must worry about overlap of hits in time. While this problem has been studied for Belle-II, the effect is small enough that it is sufficient to detect and eliminate such cases and accept a small loss in single-hit efficiency. [6] However, in this experiment, the rate of time overlaps will be larger, and two steps will be taken to mitigate the problem. First, we plan to read out six samples per hit, which will allow the unambiguous deconvolution of pairs of time-overlapping hits. Second, the shaping time of the APV25 can be reduced to 35ns to reduce overlaps once it can be established that this does not compromise the reconstruction of t0 in any way.

The flexibility and availability of the APV25 have made it popular with a number of experiments, which has further advantages. Not only are chips procurable in quantity at reasonable cost, but a reference test stand is widely available to bootstrap the development of DAQ. [7] One of these test stands is being assembled at SLAC for this experiment.

The APV25 chips will be hosted in groups of five on hybrid circuit boards, often simply referred to as "hybrids." In addition to the APV25 chips themselves, the hybrids host a number of passive components that define the power environment of the chips including the bypassing necessary to ensure the low-noise capabilities of the chips are not compromised. In order to reduce the amount of effort in developing them, the design will use existing APV25 hybrid designs as a starting point. In particular, the hybrids for the CMS Tracker Inner Barrel (TIB) were designed with similar constraints in mind and have a very compact format. [8] Mechanically, the hybrids for this experiment will have similar dimensions to the CMS TIB hybrids, with the exception that the TIB hybrids are wider due to the need to support six chips instead of five.

Unlike most trackers, the readout electronics for this experiment will not reside within the tracking volume, so the material budget for the hybrids and the cooling they require is less constrained. It is therefore anticipated that the hybrids will be fabricated in standard FR4 rather than alumina ceramics, which broadens vendor selection, reduces cost and saves turnaround time. In addition to reducing schedule risk, this will allow a prototype run to ensure that the hybrid design is sufficient without incurring significant additional costs.

4.3.4 **Detector Layout**

There are six measurement stations, or "layers", placed immediately downstream of the target. Each layer is comprised of a pair of closely-space planes and each plane is responsible for measuring a single coordinate, or "view". The details of the six layers are shown in Table 4.3.4.1 and a conceptual rendering is shown in Figure 4.3.4.1. Altogether, this layout comprises 106 sensors and hybrids and 530 APV25 chips for a total of 67840 readout channels. The total power consumption of the system is 186 Watts.

	Layer 1	Layer 2	Layer 3	Layer 4	Layer 5	Layer 6
z position, from target (cm)	10	20	30	50	70	90
Stereo Angle	90 deg.	90 deg.	90 deg.	50 mrad	50 mrad	50 mrad
Bend Plane Resolution (μm)	≈ 6.5	≈ 6.5	≈ 6.5	≈ 6.5	≈ 6.5	≈ 6.5
Stereo Resolution (μm)	≈ 6.5	≈ 6.5	≈ 6.5	≈ 130	≈ 130	≈ 130
# Bend Plane Sensors	4	4	6	10	14	18
# Stereo Sensors	2	2	4	10	14	18
Dead Zone (mm)	±1.5	±3.0	±4.5	±7.5	±10.5	±13.5
Power Consumption (W)	10.5	10.5	17.5	35	49	63

Table 4.3.4.1: Key parameters of the sensor layout for the tracking and vertexing system. Notice that the excellent single-hit resolution in the measured view enables good stereo resolution at the relatively small stereo angles necessary for pattern recognition. The stay clear region for the primary beam creates a "dead zone" in the tracker on either side of $y = 0$.

The requirements of the tracking system are discernibly reflected in the layout. The 90-degree stereo of the first three layers provides a pair of high-resolution 3-d space points for vertexing. The small-angle stereo of the last three layers minimize ghost hits to improve pattern recognition while still providing sufficient pointing resolution into Layer 3 for robust hit association in the dense environment there. Meanwhile, the presence of a bend-plane measurement in every single layer assures the best possible momentum resolution. As discussed in Section 5.3 the pattern recognition of this layout is robust and the vertexing and momentum resolution, though limited by multiple scattering, are sufficient to provide the necessary sensitivity.

Because the area needed to cover a given solid angle varies with depth in the tracker, the sensitive area varies by layer. As can be seen in Figure 4.3.4.2, it would possible to achieve almost full acceptance for low-mass A′ decays outside of the dead zone in the first four layers in a 1T magnetic field, whereas some particles escape detection in the last two layers. Because the extremely pure tracking and vertexing required here necessitates at least five hits, the acceptance of the fifth layer is the key quantity in defining the overall acceptance of the tracker. However, achieving the best purity requires the extra constraint of a hit in Layer 6, as discussed in Section 5.3.

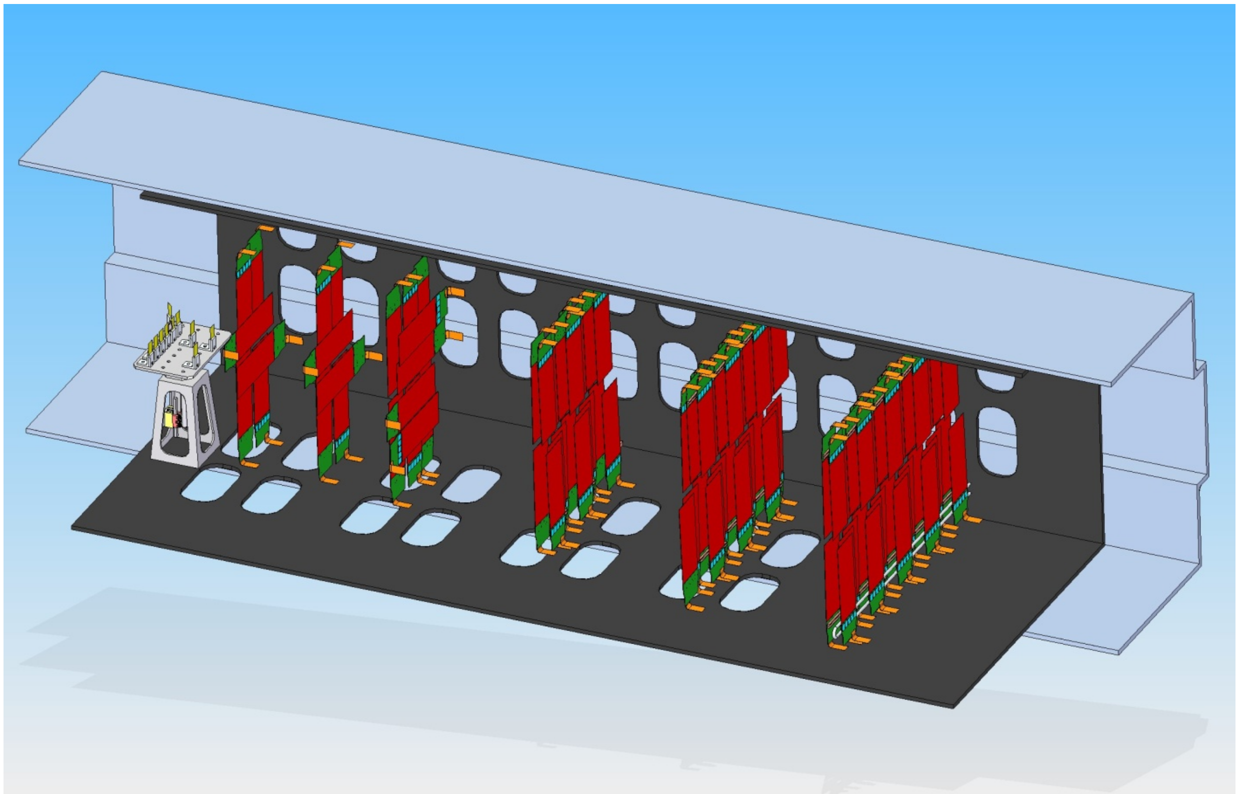

Figure 4.3.4.1: A rendering of the tracker showing the layout of the silicon planes inside a cutaway of the carbon fiber support box and the vacuum chamber. The target assembly is just upstream of the first silicon layer.

The solid angle subtended by the dead zone limits the acceptance for low mass A' decays, which have very small opening angles between decay daughters. For this reason, a great deal of attention has been paid to the optimization of this region of the detector, where careful simulation of the backgrounds has been used to determine the occupancies and radiation doses that limit coverage there.

In particular, three effects have been considered in setting the size of the dead zone. The first is the potential for an accident with the primary beam that would acutely damage or destroy a sensor. The second is the radiation dose from scattered primary beam and radiative secondaries that will render the sensors inoperable over time. The last is the density of hits associated with this radiation field that results in an unacceptable rate of pattern recognition failures. All of these issues are most severe in the first layer, which thereby determines the angular acceptance of the entire detector for prompt decays.

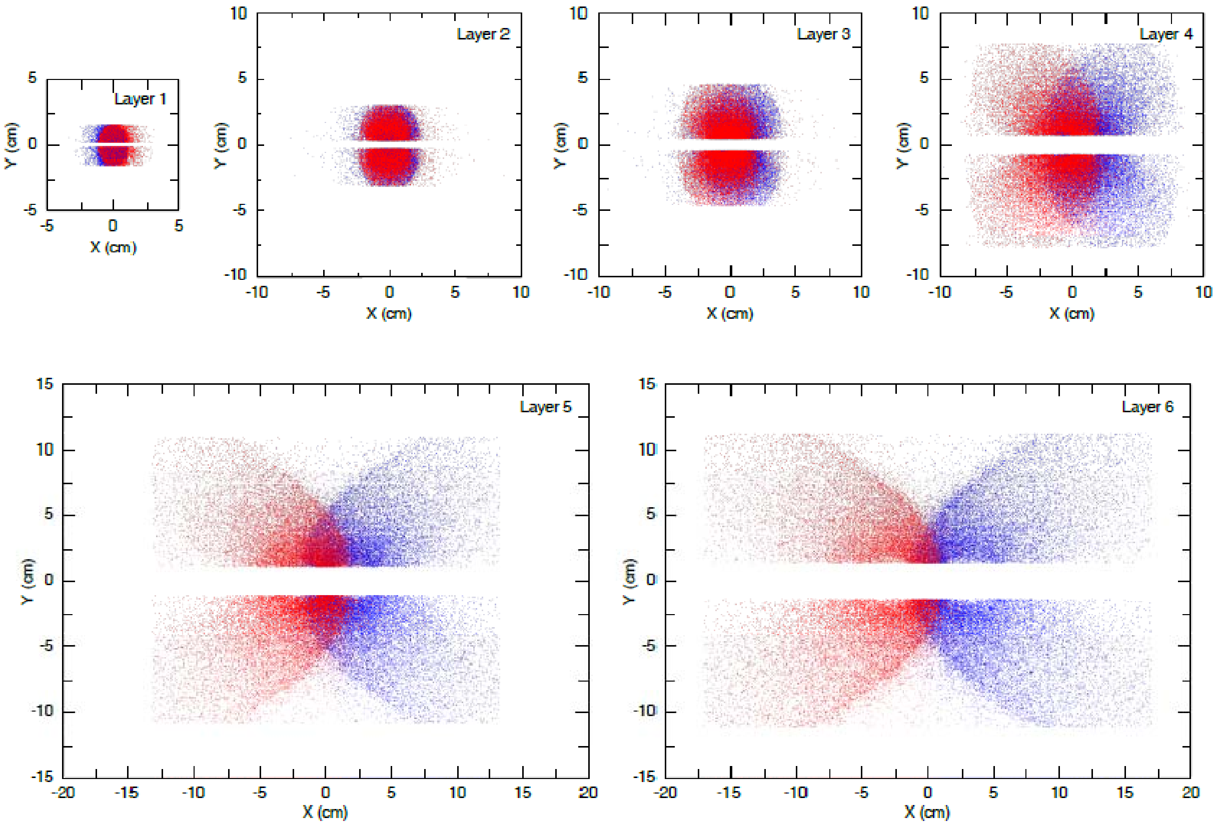

Figure 4.3.4.2: Hits in the silicon tracker in all six layers produced by A′ decays with $m_{A'}$ = 300 MeV/c^2 and E_{beam} = 5.5 GeV. All tracks that hit the first five layers are shown, resulting in a five-layer A′ acceptance of 44% in the 1T magnetic field. Over 90% of tracks within the five-layer acceptance also produce a hit in Layer 6.

The potential for acute damage from the tails of the unscattered primary beam or a steering accident is the least certain but potentially most severe liability of a small dead zone. If a 10 μm beam spot at the target is achievable, these tails should not be a limiting factor in any layer. However, the ability to retract the modules during beam adjustments and change their positions in response to changes in optics will be critically important to ensuring the safety of the detector.

The radiation field at Layer 1 provides the clearest constraint on the size of the dead zone. Under 1000V bias, the sensors will withstand more than $1{\times}10^{14}$ 1MeV neutrons before the silicon can no longer be fully depleted. [9] Since the bulk radiation damage caused by electrons with energies less than 10 GeV is approximately a factor of 30 less than 1 MeV neutrons, this corresponds to more than $3{\times}10^{15}$ electrons. [10] If we demand that the silicon remain fully depleted for three months of continuous running at 400 nA with a 0.25% X_0 target, the active silicon may not come closer than 1.5mm to the center of the dead zone, as illustrated in Figure 4.3.4.3. The depletion layer will shrink by a factor of two only after running a factor of two longer, at which time the signal loss will begin to significantly compromise time tagging. It is important to note that the rapid spatial variation of the dose in Layer 1 results in much more intense irradiation of the guard structure. Because little is known about this specific scenario, the ability to replace at least the first layer with minimal intervention is a mandatory element of the design.

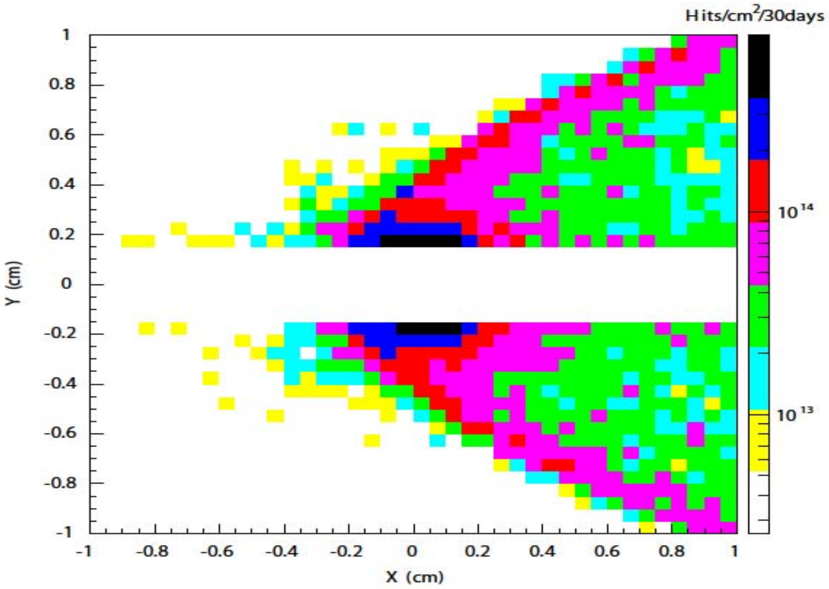

Figure 4.3.4.3: Background hits in the central portion of Layer 1 for one month of 400 nA beam. The active silicon begins at y =±1.5mm.

Limitations on the size of the dead zone due to high occupancies are less clear, and arise from two distinct considerations. First, for robust pattern recognition, it is desirable to limit the hit occupancy that must be considered during pattern recognition to less than 1%. Given hits with 2ns time resolution and a pulse period of 2.5ns, hits can be assigned to a three pulse window without loss of efficiency. Limiting three-pulse occupancy to 1% places the edge of the dead zone in the first layer at y =±1.5mm, as shown in Figure 4.3.4.4. It should be noted that a more advanced algorithm that fits hit times and positions simultaneously will be developed and should outperform this simple selection. Second, for pristine reconstruction of hit times and amplitudes, it is important to minimize triple coincidences within a time window corresponding to the time evolution of the shaper output; approximately 250 ns for the nominal 50ns shaping time. For the 1% hit occupancy considered above, the rate of triple coincidences in individual strips within the same 250 ns window is 11%. While this is probably acceptable in a small number of strips with the highest occupancy, reducing the shaping time to 35ns will suppress this rate by a factor of two and is therefore highly desirable.

Because these considerations lead to similar conclusions, the nominal dead zone of the tracker has been designated as $\theta_y < \pm 15$ mrad. It should be noted that occupancies and radiation intensities in the layers with small-angle stereo, where the sensors must be rotated, are somewhat lower and thus will allow complete stereo coverage down to ±15 mrad in all layers.

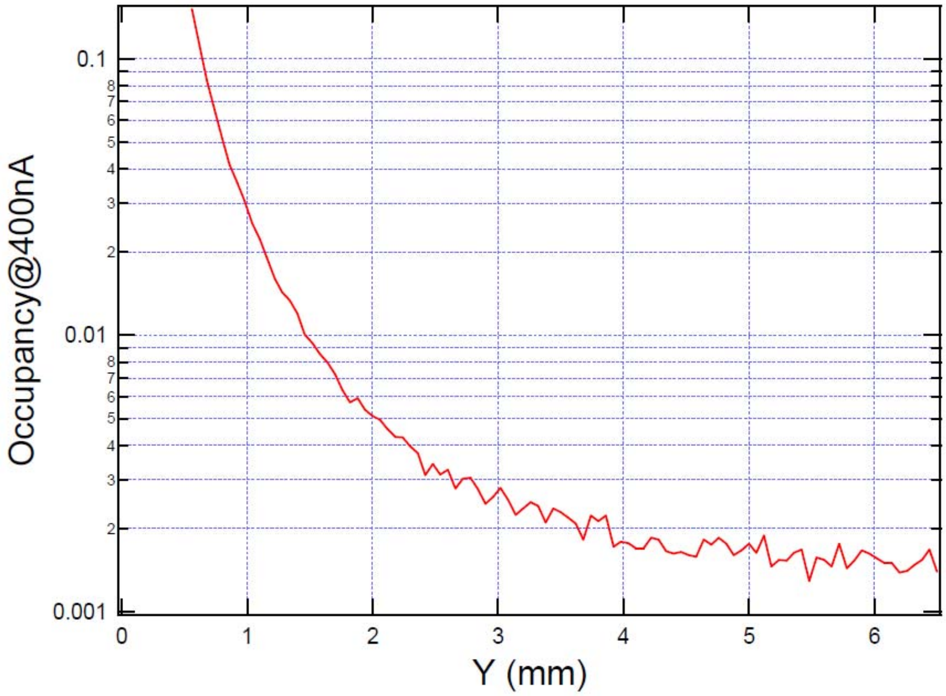

Figure 4.3.4.4: The hit occupancy per strip for 60 μm strips in Layer 1 for 400nA of beam intensity and integration over a three pulse window. This is the relevant integration time for simple track finding algorithms with 2ns timing resolution.

4.3.5 **Sensor Modules and Mechanical Support**

Each of the ten planes that measures a single view is split into two modules to accommodate the horizontal dead zone that cuts the entire tracker in half. These modules are the fundamental mechanical units of the detector: the components of a module are permanently bonded together during assembly. Each consists of a number of silicon sensors and their hybrid circuit boards glued to a composite support structure.

Adjacent silicon sensors are placed on alternating sides of the structure to provide overlap that ensures full sensitivity over the surface of the module for incident particles. In the areas between sensors on either side of the structure, holes are cut in the structures making them approximately 50% void in order to minimize the amount of material the modules present to the passage of particles. At the end of each sensor is the hybrid circuit board containing the five APV25 readout ASICs necessary to read out the signals from a single sensor. The pitch of the APV25 and the sensors are similar enough that a pitch adapter can be avoided here: wire bonds can be made directly from the chips to the sensors.

A set of modules of both types for Layer 6 are shown in Figure 4.3.5.1. Although there are ten unique module types in the system, there are only two arrangements of sensors: those that are square with each other and the underlying module support structure and those that are rotated by 50 mrad. As a result, module assembly requires at most two unique sets of tooling. The key mechanical attributes and material budget for the sensor modules are shown in Table 4.3.5.1.

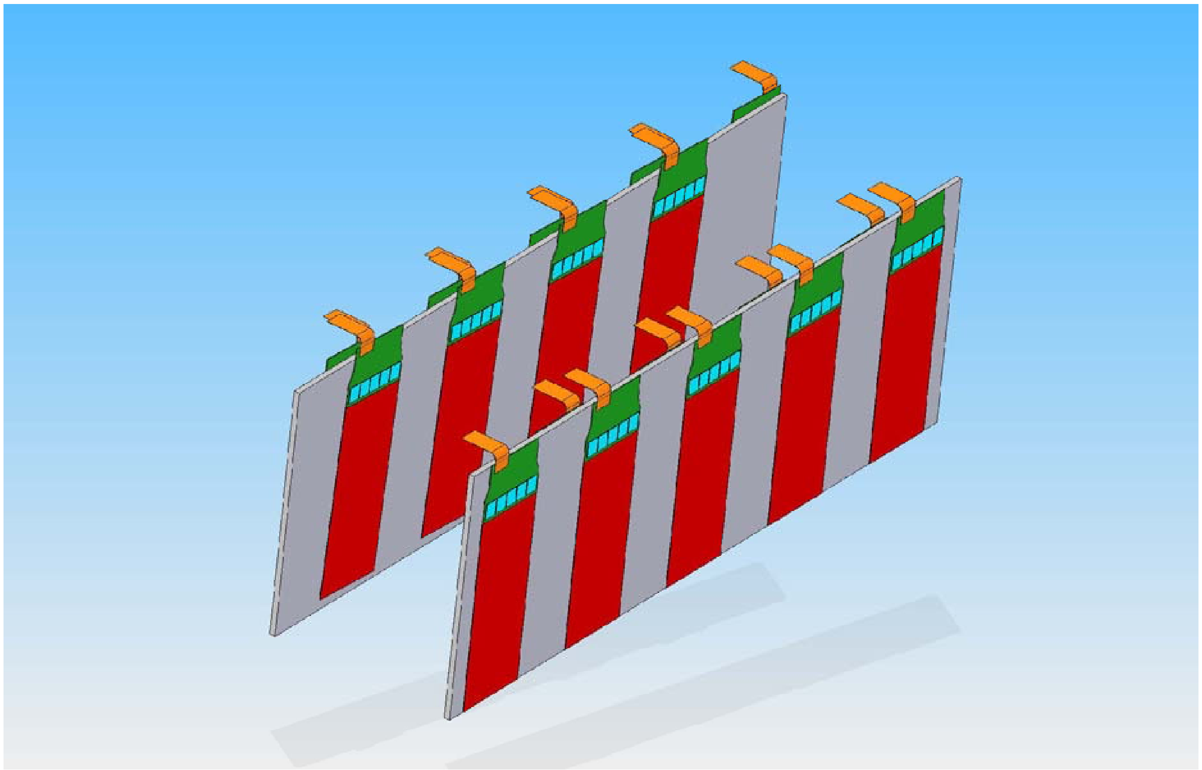

Figure 4.3.5.1: A pair of modules comprising the top half of Layer 6, a 50 mrad stereo layer. Each hybrid has a short pigtail cable attached to a solder array. These pigtails connect to longer cables dressed to the carbon fiber support box.

Each module support structure is comprised of a pair of thin, high-modulus, carbon fiber composite skins sandwiched around a low-mass rohacell core. At the edges of the support structure, running underneath the readout chips, are integrated stainless-steel cooling tubes carrying water-glycol coolant at approximately -5°C to remove the 1.7W heat load generated by each hybrid. The cooling tubes are in contact with the skins on both module faces to cool the silicon to below 0°C, reducing the rate of radiation damage and lowering bias currents to extend the useful life of the sensors. The unidirectional carbon fiber of the skins are oriented to efficiently transport heat from the silicon to the cooling tubes. This arrangement provides sufficient cooling for the silicon without placing cooling tubes inside the tracking volume that would increase multiple coulomb scattering and compromise sensitivity.

	Radiation Length (mm)	Thickness (mm)	Coverage/Unit Acceptance	Scattering Material (% X_0)
Silicon	93.6	0.320	1.2	0.410
Rohacell Foam	13800	3.0	0.5	0.011
Carbon Fiber	242	0.150	0.5	0.031
PGS Passivation	256	0.101	1.25	0.049
Epoxy	290	0.050	0.5	0.009
Total	-	-	-	0.510

Table 4.3.5.1: The material budget for the sensor modules showing the thickness, fraction covered for unit of areal acceptance and average scattering material presented to incident particles. The only full coverage glue gap bonds the carbon fiber to the Rohacell. The silicon will be attached to the passivation with epoxy dots of negligible coverage.

Atop the carbon fiber, there is a self-adhesive layer of pyrolytic graphite sheet that improves thermal conductivity and includes a layer of PEEK passivation rated at 2kV to isolate the back side of the sensors, which are at high voltage, from the conductive graphite. [11] The layers of carbon fiber and graphite will have a low-impedance connection to the analog ground of the readout electronics to ensure the best possible noise performance.

Each pair of modules that make a stereo pair covering half of the acceptance is coupled mechanically around their periphery to ensure that both move together in unison. Along the left and right edges of each pair, they are kinematically mounted to a pair of piezo motors, similar to those used for beam instrumentation. These can be operated remotely to tune the plane positions, optimizing the acceptance for the actual background environment encountered once the experiment is on beam.

The piezo motors are in turn mounted to attachment points in a carbon fiber-honeycomb composite support box that fits inside of the vacuum enclosure, as shown in Figure 4.3.5.2. This support box is the mechanical element that ties all the modules together into a complete tracking system. The cables and cooling lines that attach to the pigtail cables and cooling connections of each sensor module will be semi-permanently installed on the tracker support box to minimize the difficulty of installing and removing sensor modules.

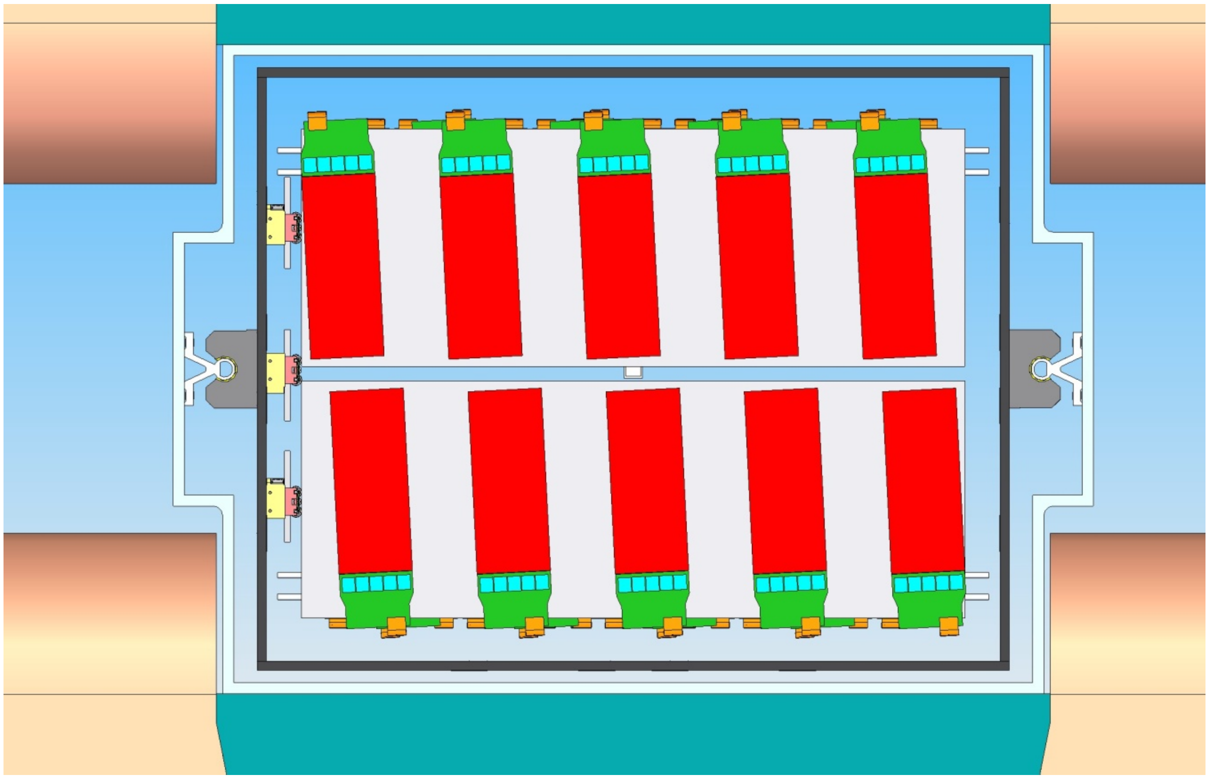

Figure 4.3.5.2: Looking upstream at Layer 6 in the tracker. The piezo motors for moving the half layers are shown at the left, just inside the carbon fiber support box, shown as the dark rectangle. The rail system allows the support box to be extracted from the vacuum chamber to access the silicon detectors and electronics.

4.3.6 **Vacuum Chamber**

The vacuum vessel will be fabricated in non-magnetic stainless-steel, which offers better strength than aluminum at smaller wall thickness. The carbon-fiber support box mounts inside the vacuum chamber on a pair of precision rails installed along the side walls of the chamber, as shown in Figure 4.3.6.1. Carriages attached to the support box glide on the rails to allow insertion and extraction of the tracker from the vacuum chamber.

To make space for this rail system without compromising acceptance, the walls of the chamber incorporate U-channels that extend into the magnet alcoves. These U-channels also stiffen the side walls against deflection when placing the chamber under vacuum, although further study is required to ensure that they are sufficiently braced so that motions induced by placing the chamber under vacuum do not damage the tracker or create alignment instabilities.

In addition to minimizing backgrounds, the vacuum acts to isolate the detector from the environment, which is important since conduction and convection would otherwise dominate the heat load and cooling requirements of the sensor modules.

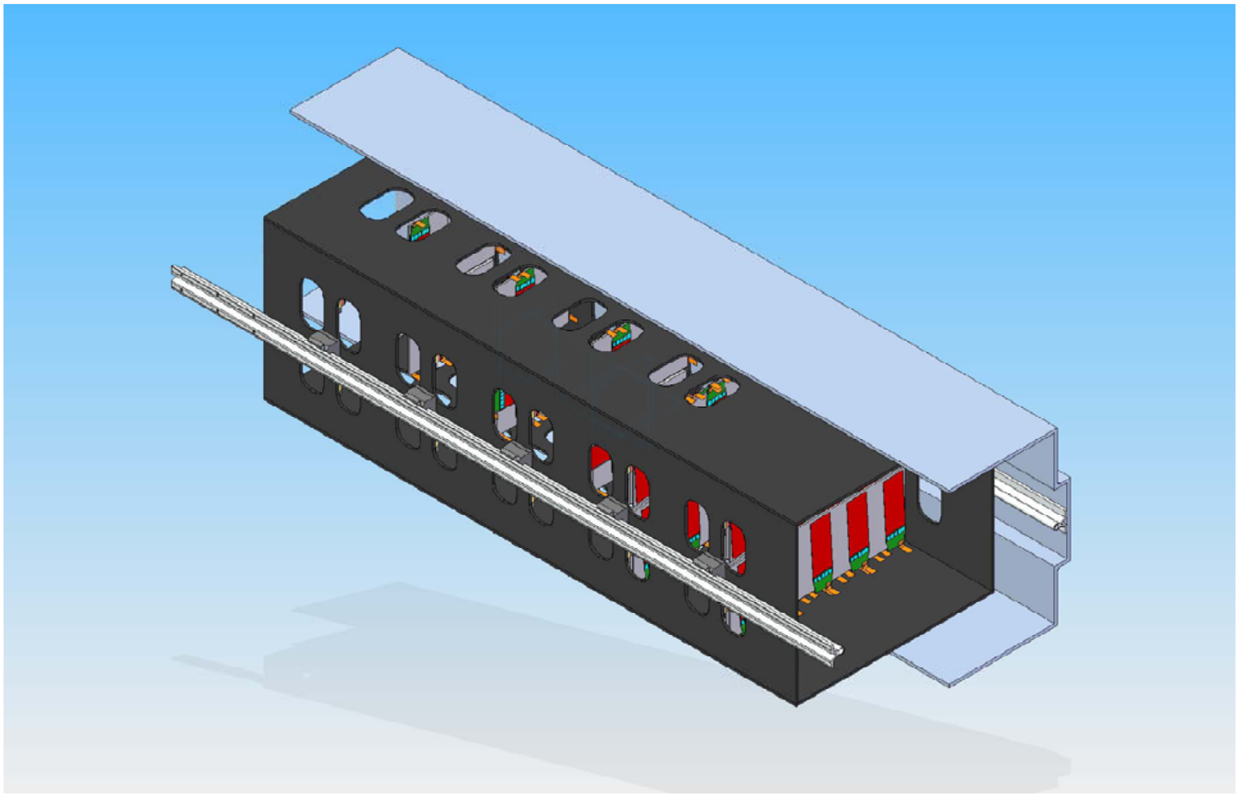

Figure 4.3.6.1: A rendering of the tracker highlighting the rail system that supports the tracker from the walls of the vacuum chamber. This allows the carbon fiber support box to be moved along the beamline with respect to the target.

In order to effectively eliminate these loads, a vacuum of 10^{-4} Torr or better must be maintained, so materials to be used inside the vessel will be chosen to minimize outgassing. In order to achieve acceptable cooling performance for the sensors given the minimal material budget, it will also be necessary to reduce the radiant heat load on the modules from the walls of the vacuum chamber. To minimize aging of the silicon and the possibility of thermal runaway, a shielding blanket of multi-layer insulation (MLI) will be wrapped around the tracker support box. This radiant barrier will reduce the heat load and resulting temperature drops by at least an order of magnitude. [12, 13].

The cables and cooling services for the tracker are routed to the upstream end of the vacuum chamber where a patch panel will be located. The design of this panel and the cooling and cable connections are of critical importance due to space constraints and the necessity of maintaining good vacuum. Further, since we will not be able to operate a sub-atmospheric cooling system inside the chamber, extra care will be required for all cooling connections and joints.

The rollers attaching the carbon fiber support box to the vacuum chamber will allow the entire tracker system to be rolled into and out of the magnet with relative ease. This arrangement will enable the tracker to be installed or serviced in a relatively short period of time with only removal of a relatively short spool piece in the upstream beamline. Figure 4.3.6.2 shows the tracker installed within the analyzing magnet.

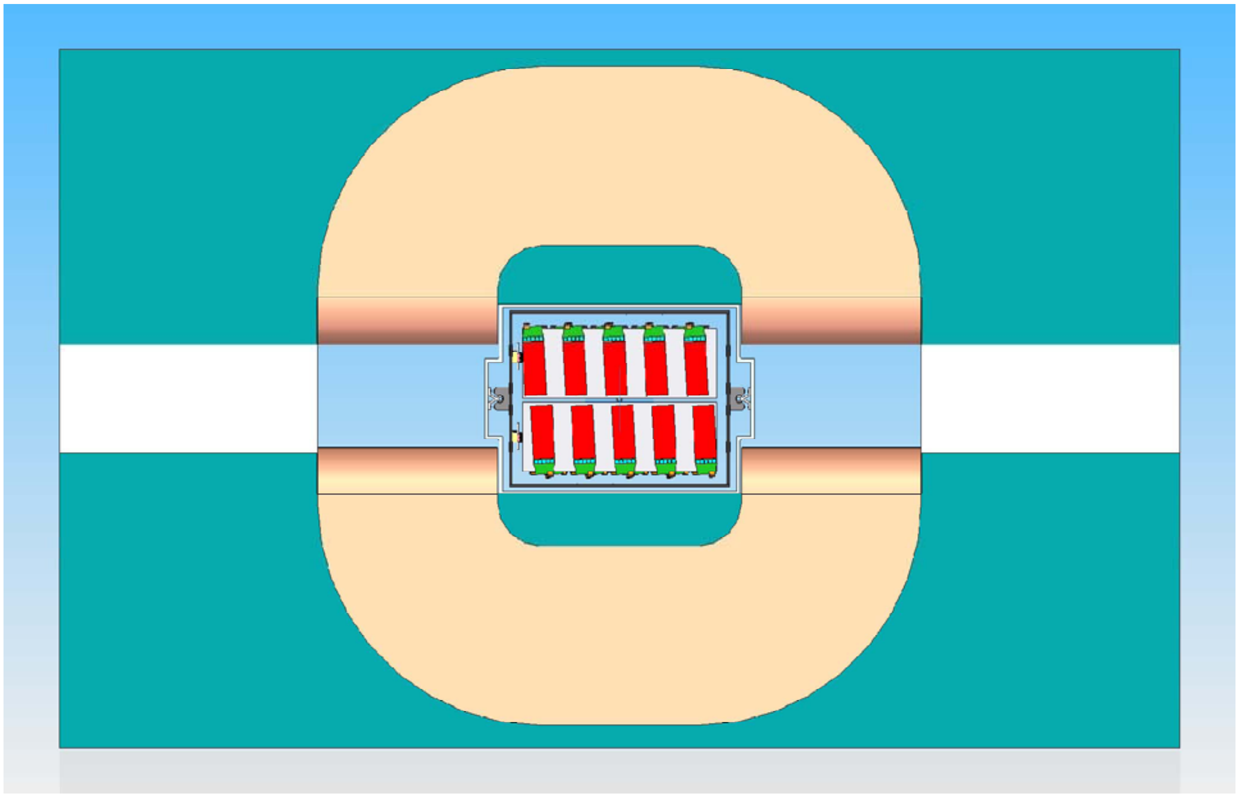

Figure 4.3.6.2: A rendering of the tracker installed within the analyzing magnet. There is significant additional space within the magnet alcoves to accommodate reinforcements to the walls of the vacuum chamber or other necessary services.

4.3.7 **References**

1. DØ Collaboration, *DØ Run IIb Upgrade Technical Design Report*, http://d0server1.fnal.gov/projects/run2b/Silicon/www/smt2b/Documentation/D0_Run2b_TDR_Silicon_Sept24_02.pdf
2. M.J. French et al., Design and results from the APV25, a deep sub-micron CMOS front-end chip for the CMS tracker, NIM A 466 (2001) 359–365.
3. P. Azzi et al., *Charge Deposition Model in Silicon*, CDF Internal Note CDF/DOC/TRACKING/CDFR/5080 (1999).
4. M. Friedl et al., Performance of a CMS silicon strip detector module with APV25 readout, NIM A 488 (2002) 175–183
5. M. Friedl et al., Performance of a CMS silicon strip detector module with APV25 readout, NIM A 488 (2002) 175–183
6. Y. Nakahama, Research and Development of a Pipeline Readout System for the Belle Silicon Vertex Detector, University of Tokyo Masters Thesis, (2006)
7. RWTH Aachen CMS Group, *The ARC System*, http://www.physik.rwth-aachen.de/institute/institut-iiib/forschung/cms/detektorentwicklung/arc/

8. U. Goerlach, *Industrial Production of Front-End Hybrids for the CMS Silicon Tracker*, 9th Workshop on Electronics for LHC Experiments, Amsterdam (2003)175-179
9. G. Lindstrom, Radiation damage in silicon detectors,NIM A 512 (2003) 30–43
10. I. Rachevskaiaa et. al, Radiation damage of silicon structures with electrons of 900 MeV, NIM A 485 (2002) 126–132
11. Panasonic Industrial Products Catalog, http://industrial.panasonic.com/www-data/pdf/AYA0000/AYA0000CE2.pdf
12. S. D. Augustynowicz, J. E. Fesmire, and J. P. Wikstrom, *Cryogenic Insulation Systems*, http://ntrs.nasa.gov/archive/nasa/casi.ntrs.nasa.gov/19990053342_1999081754.pdf
13. . D. Augustynowicz and J. E. Fesmire, *Cryogenic Insulation Systems for Soft Vacuum*, http://ntrs.nasa.gov/archive/nasa/casi.ntrs.nasa.gov/19990062736_1999085329.pdf

4.4 Electromagnetic Calorimeter

The electromagnetic calorimeter (ECal) will provide the trigger for data acquisition and will also be used for electron identification during the data analysis. The ECal will be positioned after the analyzing dipole magnet and will cover the full acceptance region of the silicon tracker. The energy of electrons of interest will be in the range 0.5-5.5 GeV. The ECal modules must have sufficient radiation lengths to absorb the full energy of these scattered electrons.

The calorimeter will consist of two parts, beam-up and beam-down (see Figure 4.4.1). The gap between upper and lower halves is necessary to avoid the beam electrons, as well as those which have radiated in the target and the bremsstrahlung photons they have produced.

To optimize the performance and cost of the detector we have chosen a hybrid calorimeter design which combines lead tungstate ($PbWO_4$) crystals read by avalanche photodiodes (APD) and lead-glass or “SHASLYK” type modules with conventional PMT photodetectors. Since the area near the beam plane is under the highest radiation load, the modules near it must be radiation resistant and should have finer granularity. The lead tungstate crystals that we are planning to use are from the CLAS inner calorimeter (IC) and they fully meet the latter requirements. The outer three rows in each half will be covered by larger, lead-glass or “shashlyk" type, modules as shown in 4.4.1.

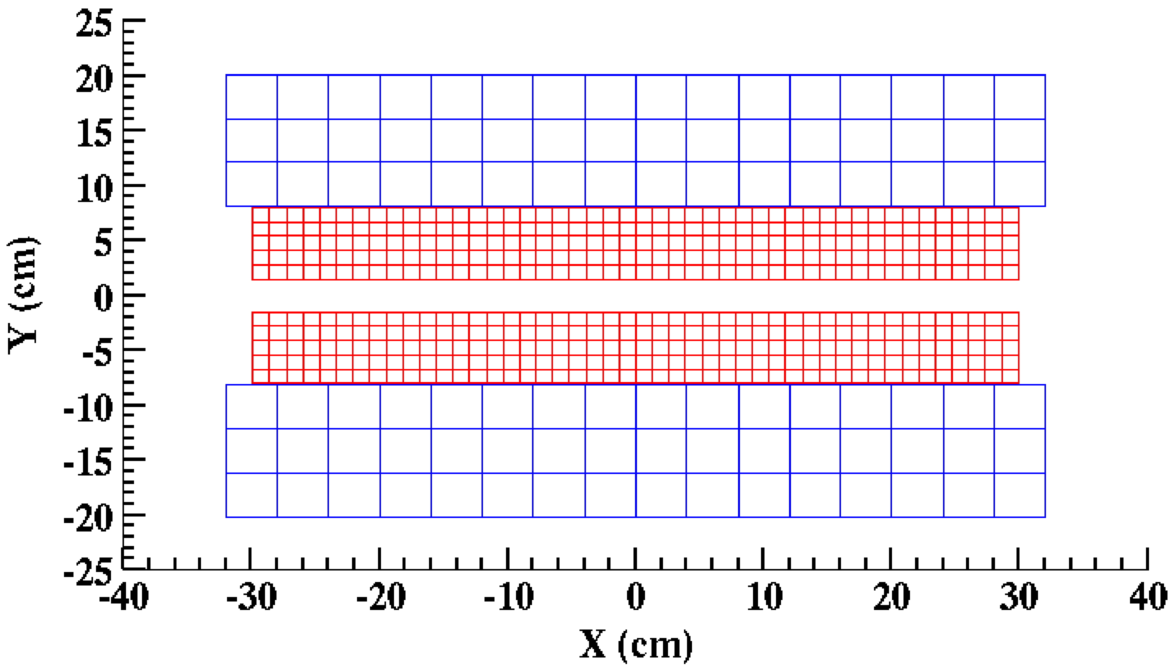

Figure 4.4.1. Beam's eye view of the electromagnetic calorimeter. Red squares represent lead-tungstate modules, blue squares are lead-glass or "shashlyk" type modules.

A rendering of the calorimeter system is show in Figure 4.4.2. The calorimeter is separated from the beam vacuum by a 1 cm thick aluminum vacuum exit window (made transparent in the figure). The beam goes through a continuous vacuum from the vacuum box in the magnet to a vacuum enclosure made from 1 cm aluminum plates which is inserted between the top and bottom calorimeters. A different configuration, where the beam exited through a thin vacuum window into a region filled with helium for the calorimeter, was rejected due to the increased background rates. To further reduce the background rates without diminishing the structural integrity, a small area of the aluminum plates is cut out where the most intense part of the electron beam exits to the beam dump.

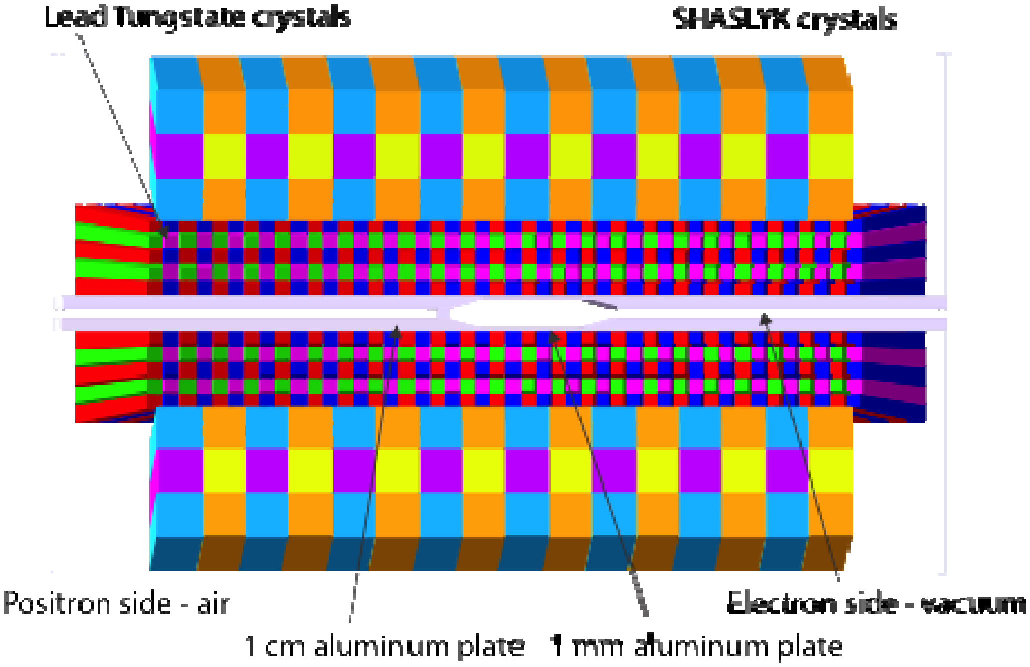

Figure 4.4.2. A rendering of the electromagnetic calorimeter setup looking down the beam line. The front exit window and side plates are rendered transparent to permit a view of the crystals and the vacuum plates.

4.4.1 **The Inner Calorimeter**

The inner part of the ECal will be built out of 460 lead-tungstate crystals, from the same crystals that were used in the IC. The IC calorimeter was assembled from 424 lead-tungstate tapered crystals with dimensions of 13.3 × 13.3 mm^2 (front face), 16 × 16 mm^2 (rear face) and 160 mm length. There are about 40 more spare crystals that can be used for the ECal. The crystals were fabricated with very tight tolerances: $\sigma = 19$ μm for 13.3 mm dimension and $\sigma = 13$ μm for the 16 mm dimension. Each crystal is wrapped in VM2000 multilayer polymer mirror film and has a plastic fiber holder glued on its front face for light monitoring.

Avalanche Photodiodes (APD) S8664-55 produced by Hamamatsu Corp. are used as photodetectors. They have a 5 × 5 mm^2 active area and a high quantum efficiency (about 75 %). Single APDs were centered on the back ends of the crystals using MeltMount 1.7 glue. The low-amplitude signals of APDs are amplified using custom-made preamplifier boards. A schematic view of the IC module assembly is presented in Figure 4.4.1.1.

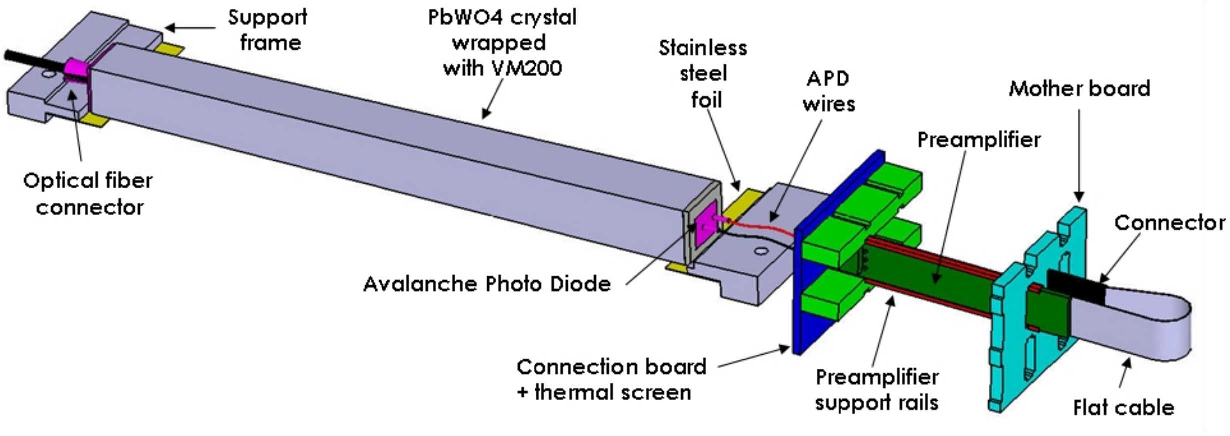

Figure 4.4.1.1. Schematic view of IC module assembly.

In order to maintain stable performance of the $PbWO_4$ calorimeter, the temperature in the ECal enclosure must be stabilized within 0.1 ^{0}C. The expected energy resolution of the system (from operational experience with the IC) is $\sigma_E/E \sim 4.5\%/\sqrt{E}$ (GeV).

4.4.2 **The Outer Calorimeter**

For the outer layers of the ECal we are planning to use either lead-glass modules (TF-1), available through the Yerevan collaboration, or “shashlyk” type sampling calorimeter modules, available from the Two Photon Exchange (TPE) experiment in Hall B (25 such modules will be used to measure the intensity of e+/- beams during the TPE experiment).

The size of the lead-glass module is 40x40x400 mm^3. A schematic view of the detector assembly with the above modules is presented in Figure 4.4.2.1. These detectors have been used at JLAB.

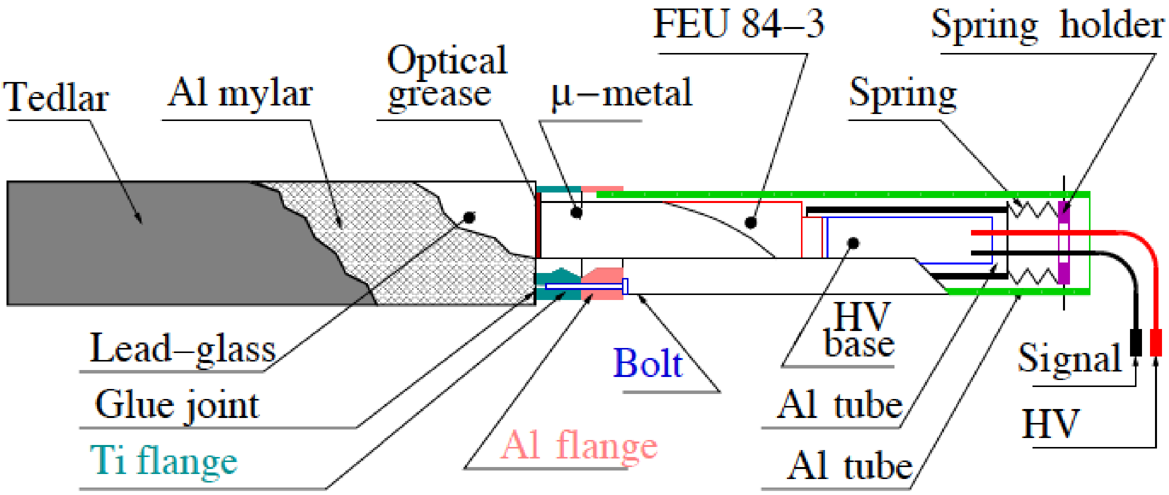

Figure 4.4.2.1. Lead-glass counter assembly used in previous JLAB experiments with the TF-1 module.

The “shashlyk” modules are assembled from 156 alternating layers of lead and scintillator plates and have size 38x38x600 mm^3, as shown in Figure 4.4.2.2.

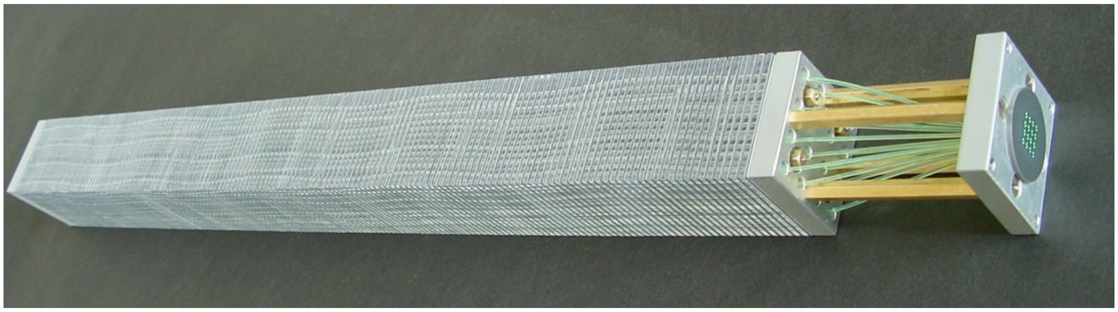

Figure 4.4.2.2. “Shashlyk” module assembly.

A total of 96 modules will be needed to construct the outer part of the ECal. The final decision on the type of the detector to be used for ECal will be made based on the results of final simulations and mechanical design. As for performance, both detectors have similar energy resolution, $\sigma_E/E \sim 5.5\%/\sqrt{E}$ (GeV), which satisfies the experimental requirements.

4.4.3 **ECal Assembly**

The ECal will be mounted behind the analyzing dipole magnet, after the vacuum chamber window, as shown in Figure 4.4.3.1. The distance from the front face of the calorimeter modules to the magnet center will be about 75cm. The ECal modules will be assembled inside a calorimeter box, which provides temperature stabilization. The upper and lower parts of the ECal will be separated by a vacuum chamber, which allows unimpeded beam transport to the beam dump and minimizes the material radiative electrons and photons will encounter. The calorimeter box will be sealed and will have thermal insulation to provide the required temperature stabilization (similar to the IC box assembly). As in the IC, $PbWO_4$ modules will be connected to a motherboard that will provide power to and transmit signals from individual APDs and pre-amplifier boards. PMT high voltages and signals for lead-glass or “shashlyk” modules will be transmitted through side walls of the ECal box assembly.

The CLAS IC box assembly, crystal support frames, pre-amplifier boards and the motherboard were designed and fabricated by the Orsay (France) collaboration in CLAS. That group is interested in participating in this experiment and will carry most of the load in the design and construction of the ECal.

4.4.4 **Electronics**

Existing low and high voltage systems for the IC will be used for the lead-tungstate part of the ECal. For the PMTs of the lead-glass or “shashlyk” modules, the CLAS PMT HV system can be used. Signals from each module will be sent to a signal splitter (similar to the IC readout), then one of outputs of the splitter will be fed to a discriminator and then to a TDC channel, while the second one will be sent to the FADC. The trigger from the ECal will be based on FADC information as described in Section 4.6.5.

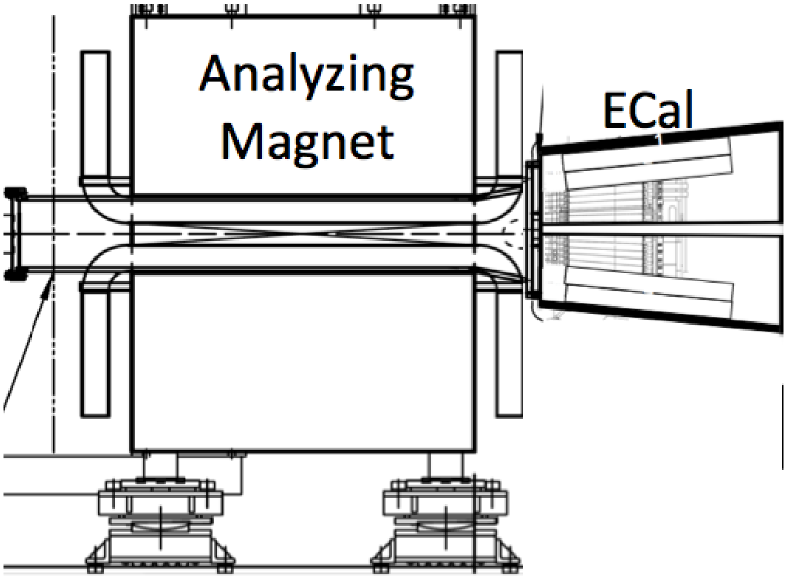

Figure 4.4.3.1. Ecal placement behind analyzing magnet

4.5 Muon System

Searching for the A′ in its di-muon decay mode has the advantage of having greatly reduced electromagnetic backgrounds for triggering. The muon detection system will be installed behind the ECal which absorbs most of the electromagnetic background produced in the target. The remainder will be attenuated by the first absorber layer of the muon system. Remaining backgrounds will arise from photoproduction of π+ and π- pairs in the target, which aren't fully absorbed in the ECal or absorber. The muon detector will be about 1 meter long and will consist of layers of scintillator hodoscopes sandwiched between iron absorbers. The number of layers and the thickness of absorbers will determine the π/μ rejection factor.

4.5.1 Simulation of the Muon System

In order to optimize the setup, charged pions and muons were simulated from upstream of the ECal (lead-tungstate part only) in the momentum range from 1 GeV/c to 4 GeV/c using the GEANT-3 model for the CLAS Inner Calorimeter (IC). Five layers of iron absorbers interlaid with layers of 1 cm thick scintillator planes were positioned 1 meter from the front face of the IC, as shown in Figure 4.5.1.1. The figure shows a few of the simulated π+ events. Most pions will shower in the IC and in the iron absorbers and will not reach all way to the last layers of the scintillation hodocopes, while most muons will leave mip traces in the scintillator and, depending on their momenta, will pass through most or all of the layers of the system.

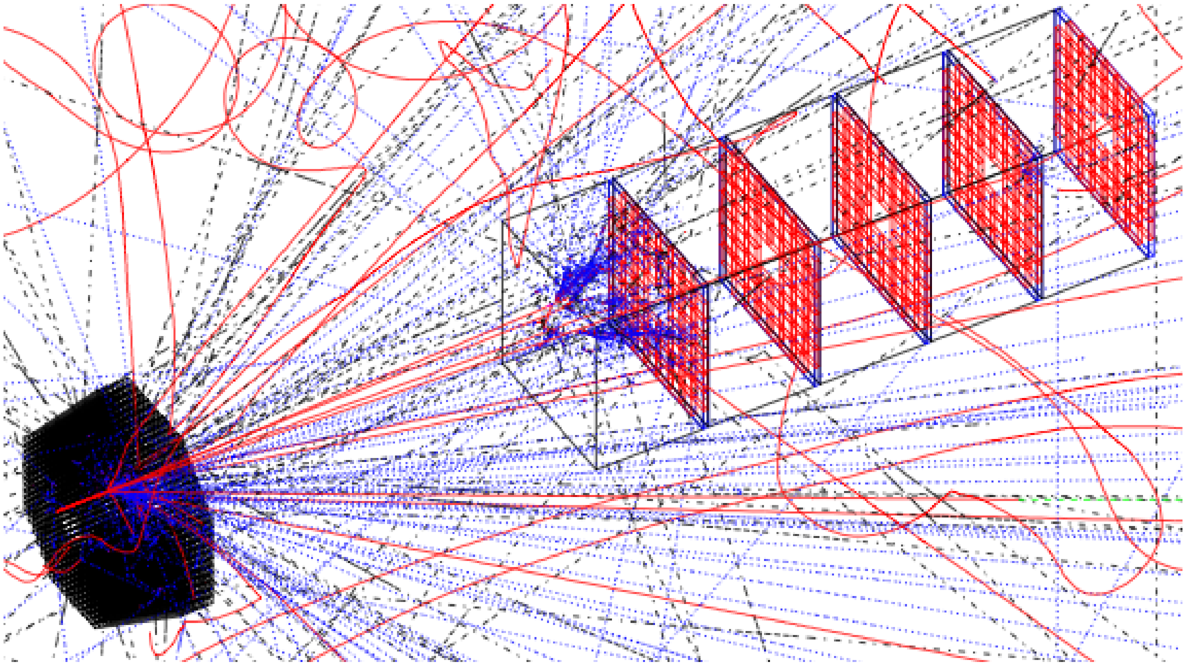

Figure 4.5.1.1. Simulated pion events in GEANT-3 model of IC and in five layers of iron absorbers and scintillators.

The distribution of the deposited energy for muons (top graphs) and pions (bottom graphs) in the 16 cm long lead-tungstate crystals (left graphs) and in 1 cm thick scintillator layers (right graphs) are shown in Figure 4.5.1.2. Detection efficiencies for pions and muons were defined as the ratio of the number of particles that passed through cuts on energy deposition in IC, $\Delta E > 100$ MeV, and in hodoscope layers, $\Delta E > 0.4$ MeV, to the number of simulated events.

In Figure 4.5.1.3, the dependence of pion (open squares) and muon (filled squares) detection efficiencies on the total thickness of the iron absorber is shown. The muon detection efficiency decreases slightly for up to a meter of the total absorber length, while the detection efficiency for pions shows exponential drop up to an absorber thickness of 75 cm.

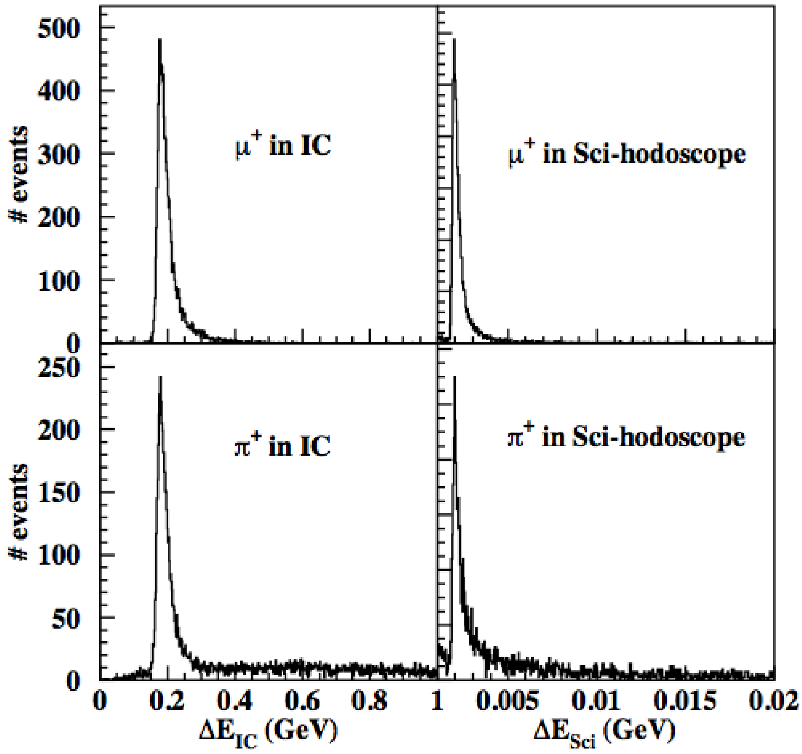

Figure 4..5.1.2. Energy deposition of muons (top graphs) and pions (bottom graphs) in IC (left) and in scintillation hodoscopes (right).

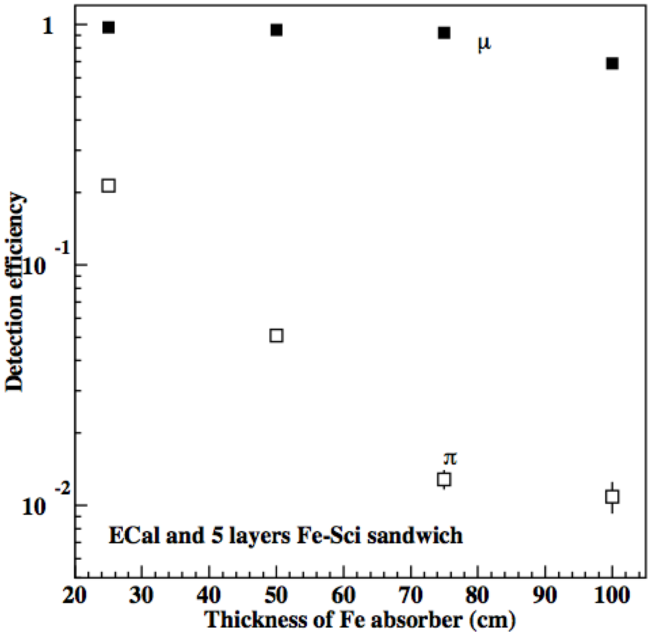

Figure 4.5.1.3. Efficiency of pion and muon detection as a function of total iron absorber thickness in five-layer configuration.

In Figure 4.5.1.4, the rejection factor for charged pions is presented. As can be seen from the figure, for particles from 1 GeV to 4 GeV, the optimal thickness of the iron absorber for pion rejection is ~75 cm (after 16 cm of lead-tungstate). In the efficiency calculation for low energy particles (< 1.7 GeV), not all the layers were considered. Depending on the momentum, particles were not traced behind the third, fourth or fifth absorber.

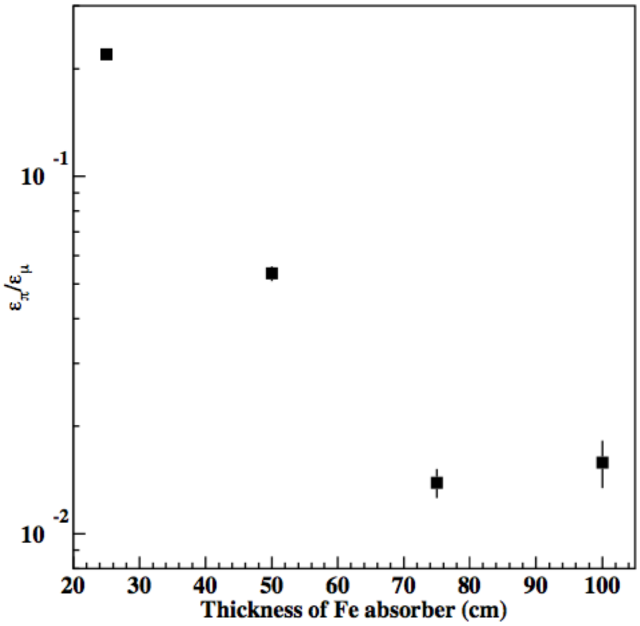

Figure 4.5.1.4 Pion-muon rejection factor as a function of the iron absorber thickness.

4.5.2 Detector Concept

Based on the above simulation, the muon detector is proposed as a system of four iron absorbers (total length of 75 cm) and four scintillator planes positioned after each absorber layer. The first absorber will be 30 cm long; the other three will have equal lengths of 15 cm. The muon detector will be mounted behind the ECal, see Figure 4.5.2.1. The pion rejection ($\varepsilon^\pi/\varepsilon^\mu$) of the proposed system as a function of particle momentum is shown in Figure 4.5.2.2. For the determination of particle detection efficiencies, only signals in the first three layers of the hodoscope were used for momenta < 1.7 GeV/c. In the full momentum range from 1 to 4 GeV/c, $\varepsilon^\pi/\varepsilon^\mu$ varies from 10^{-2} to $2\text{x}10^{-2}$ and therefore the pion pair suppression factor of the system will be $< 4\text{x}10^{-4}$. Similar to the Ecal, the muon detector will consist of two halves, one above and one below the beam. The vertical gap between the first hodoscope layers of the two halves is about 3 cm. The cross section of each half of the first hodoscope is 63x39 cm^2. Each half of the last hodoscope layer is 74x46 cm^2.

The simplest, most economical solution for the hodoscopes is to use layers of extruded scintillator strips with embedded wave-shifting fiber readout. The scintillator strips will be oriented horizontally. The light will be detected from both ends of the strip using multi-anode photomultipliers. With 5 cm vertical segmentation, a total of 144 readout channels are needed (9x16 channels multi-anode PMTs). Signals from each channel will be sent to a TDC and to a FADC. The FADC information will be used to construct the muon trigger. The TDC information together with information from FADC will be used in offline analysis to measure the hit position along the strip.

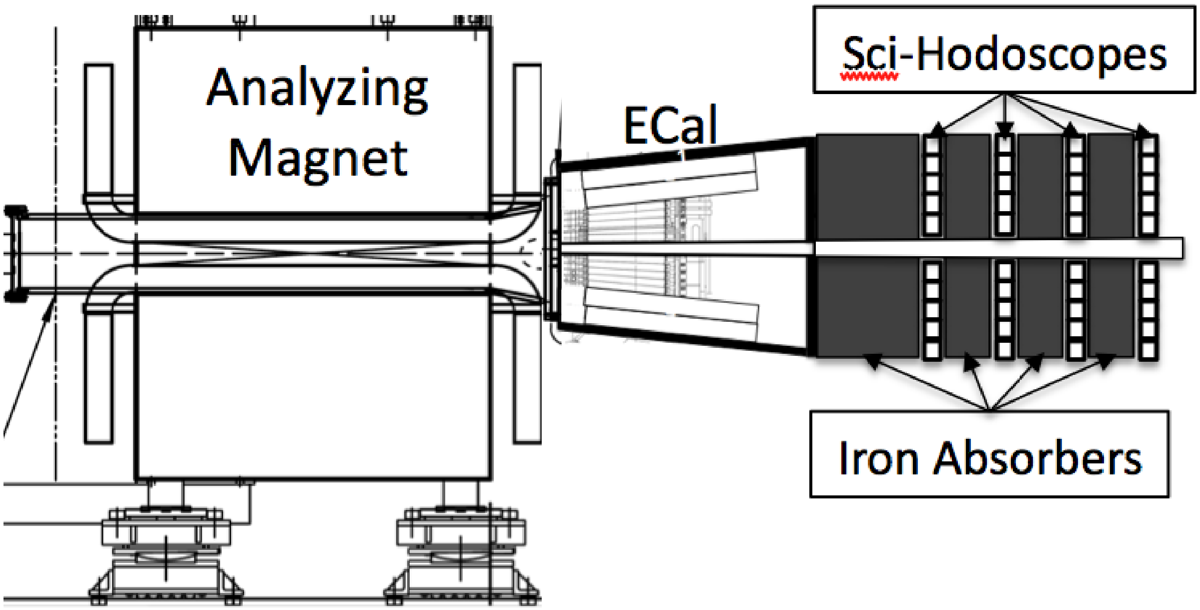

Figure 4.5.2.1. Schematic view of the HPS detector with muon detection system.

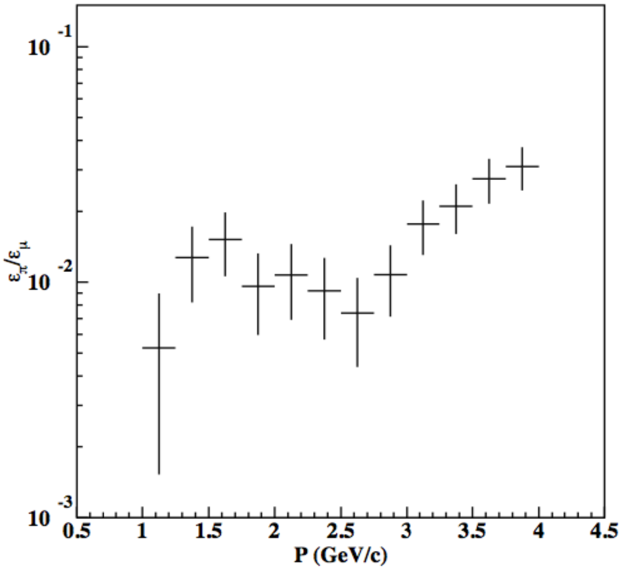

Figure 4.5.2.2 Pion rejection factor in the proposed muon detector system.

4.6 Electronics and DAQ

There are three front-end electronics systems, an Electromagnetic Calorimeter (ECal) system, a Silicon-Vertex Tracker (SVT) system, and a Muon system. A level 1 hardware trigger selects events to be read out. Only the ECal and the Muon system provide inputs to the Level 1 trigger system. The triggered events from the three sub-systems are acquired and processed in the data acquisition and processing system. The events are down-selected in a Level 3 filter processing farm and the remaining events are transferred to the offline storage. The generic scheme for the HPS DAQ system hardware is shown in Fig.4.6.1. This system will be described in detail in the following sections.

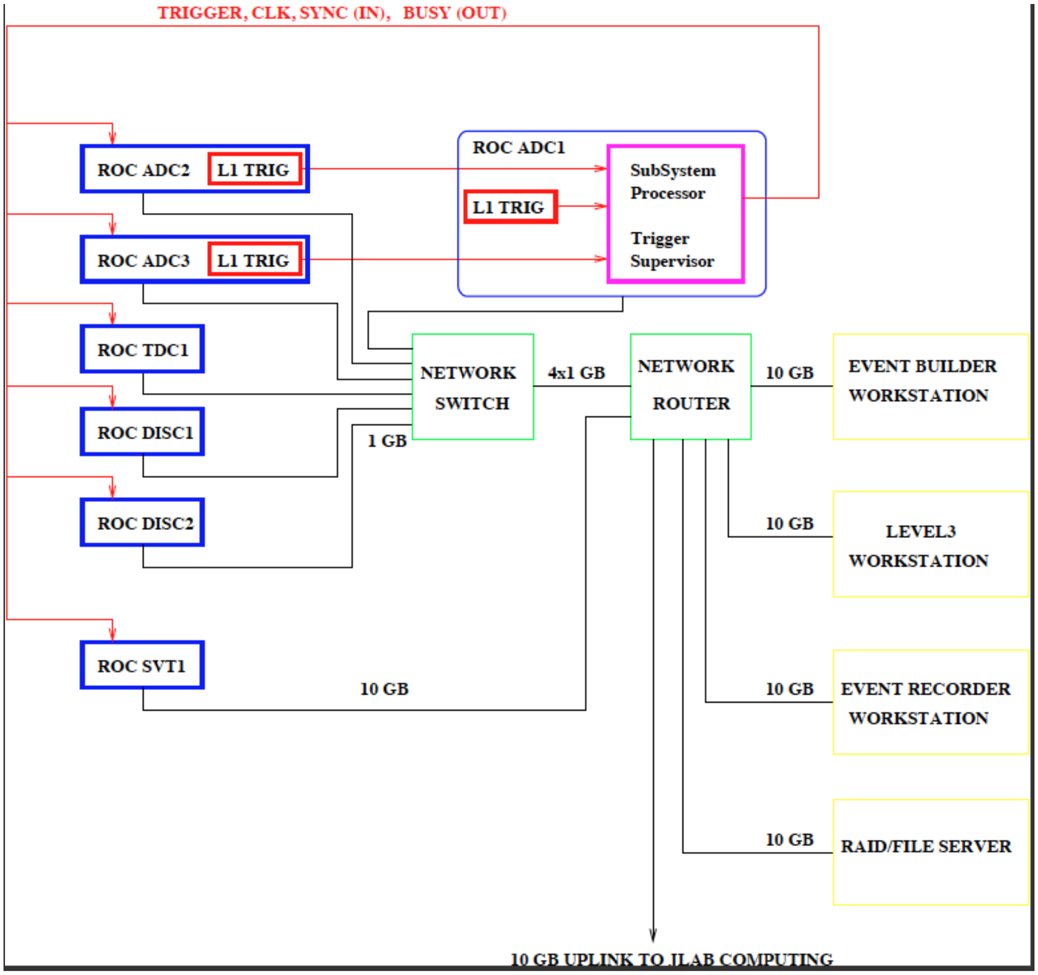

Fig.4.6.1. Readout and processing system block diagram

4.6.1 Electromagnetic Calorimeter Systems

4.6.1.1 Front-end

The Electromagnetic Calorimeter has 556 channels. The system described below can handle up to 560 channels for the ECal plus 144 channels for the Muon System. The charge from APD devices is amplified and shaped in existing JLAB front-end electronics as described in Section 4.4.1. Amplified signals from APDs and anode signals from PMTs will be sent to a splitter. The splitter output will feed FADCs and TDCs.

4.6.1.2 Readout

One of the outputs from every splitter channel is connected to a Flash ADC (FADC) channel packaged in 16-channel VXS modules. Three VXS crates will be used to accommodate 35 16-channel ADC boards plus 9 boards for the Muon System, as shown in Figure 4.6.1.1.

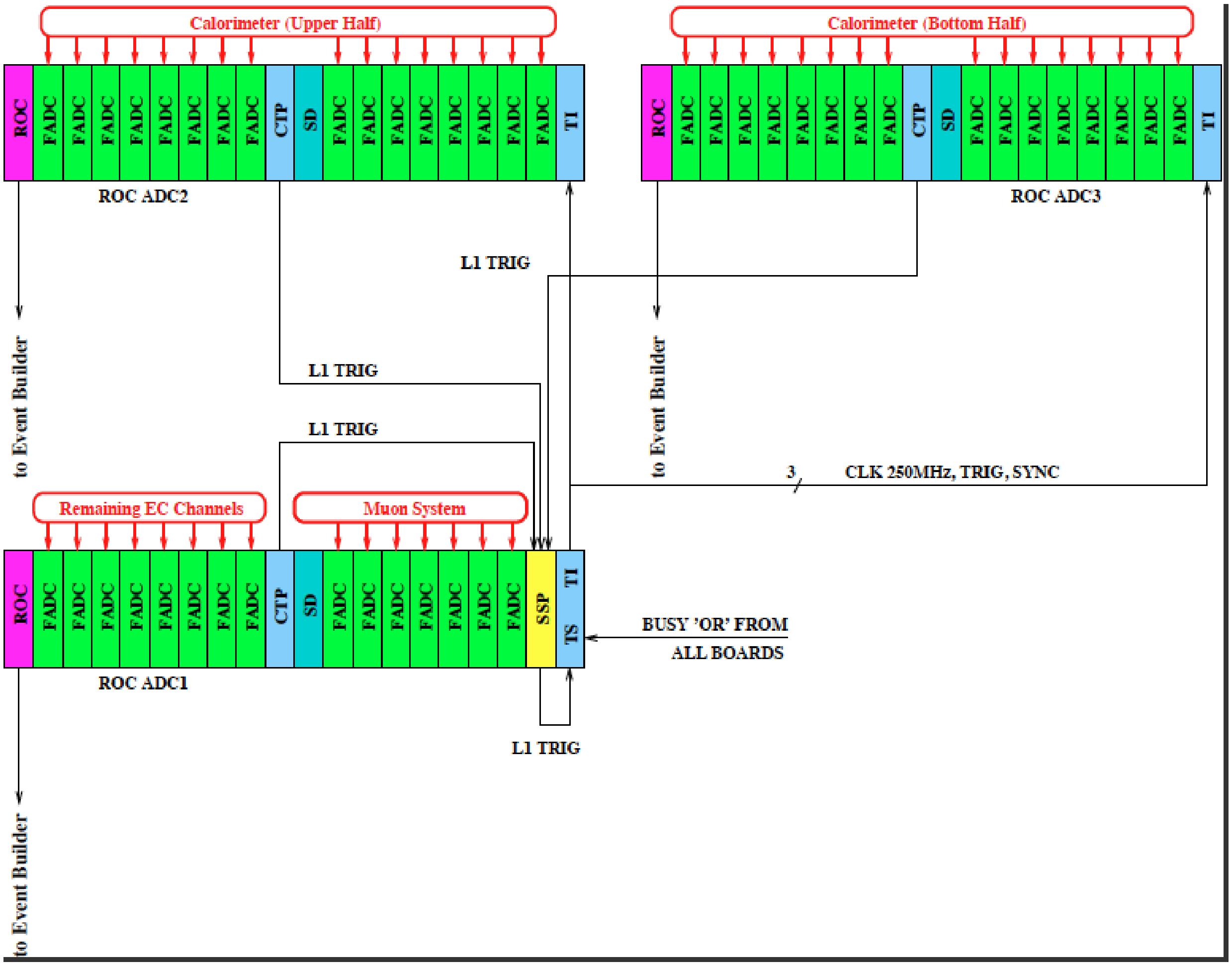

Fig.4.6.1.1 Calorimeter data acquisition and trigger system.

The 16-channel JLAB-made 12-bit 250-MHz Flash ADC boards are still under development and will be in production by the end of 2010 calendar year.

4.6.1.3 **Trigger**

The FADCs are a significant part of the trigger system and will send signal information to the Crate Trigger Processor (CTP) board installed in the same crate. The signal information will include energy for every channel above threshold. A threshold will be applied to the energy sum of several consecutive hits in the same FADC channel as described below. Information will be sent to the CTP board over the back-plane serial bus every 16 ns. The CTP board will perform cluster finding and form the trigger decision. There are three CTP boards in three VXS crates working in parallel searching for clusters in the ECal. Results are reported to the Sub System Processor (SSP) board installed in one of the VXS crates. The SSP board does additional cluster finding on the boundaries between different VXS crates, and forms the final trigger decision.

4.6.2 Silicon Vertex Tracker System

The SVT readout system is shown schematically in Figure 4.6.2.1.

4.6.2.1 **Front – End Hybrid**

There are a total of 106 silicon strip sensors, each one connected to a hybrid holding five 128-channel APV25 integrated circuits. The APV25 provide amplification and analog storage for trigger accepted events. There are 5 analog outputs for each 640-channel hybrid. Each hybrid will be connected via a multi-twisted-pair cable to a readout board.

4.6.2.2 **Readout**

The SVT readout system is shown in Figure 4.6.2.1. The outputs of up to 10 hybrids are digitized on ATCA (Advanced Telecommunication Computing Architecture) readout boards. At least 10-bit ADC's are used to digitize the APV25 outputs at a rate of ~40 MHz (system clock of 250 MHz/6 = 41.666 MHz). The board will also contain FPGA's and will be designed at SLAC. Nine of the ATCA readout boards are housed in one 14-slot ATCA chassis. The ATCA crate will be equipped with commercial CPU board and custom TI (Trigger Interface) unit to communicate with JLAB DAQ and Trigger Systems. The TI card will also be designed at SLAC, using essentially the same circuit as the existing JLAB VME card but in an ATCA form factor. The data from the SVT boards will go over Ethernet to a tracker specific CPU board in the same ATCA crate. This board will process the data and send it in one transfer to the rest of the DAQ system.

The destination host and TCP port will be obtained by the CPU board from run control and passed to all SVT readout boards. Also, the CPU board will propagate DAQ commands (download, prestart, go, end etc) to SVT boards.

The crate also contains an existing 10-G switch card, the CIM (Cluster Interconnect Module) which acts as a switch to connect the 10 readout board, the TI, and the CPU to the JLAB network switch shown in Figure 4.6.1.

The trigger and clock and synchronization signals are received by the TI module and distributed via the ATCA backplane to all the modules.

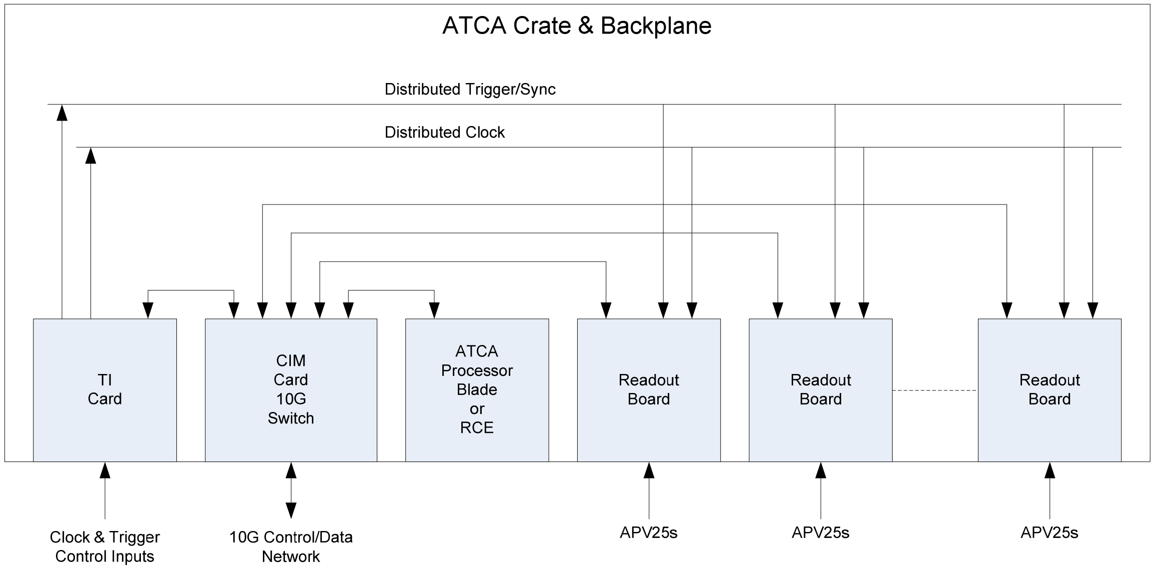

Fig.4.6.2.1. SVT Readout System

4.6.2.3 **Trigger**

The SVT does not provide signals for the Level 1 trigger decision.

4.6.3 **Muon System**

There will be 144 channels which will be read out and also take part in the Level 1 hardware trigger. The data will be input to additional FADC modules, like the ECal System described above.

4.6.4 **System Timing**

All crates receive the 250-MHz master clock. SVT will divide it by 6 for internal use. The ECal and Muon system signals are digitized at 250 MHz (every 4 ns) with a trigger signal generated every 16 ns. The phase of the SVT clock will be latched when the trigger signal is received to correct for the phase of the divide by 6 clock compared to the trigger time.

4.6.5 Level 1 Trigger

4.6.5.1 Trigger System Timing and Layout

Trigger logic will search for a coincidence between different signals every 16 ns; i.e., a single trigger operation takes 4 clocks x 4ns = 16ns.

The maximum trigger decision time (latency) is currently set to 3 μs for Level 1. That value is defined by the SVT readout APV25 chip. A preliminary FPGA algorithm analysis shows that 3 μs for Level 1 should be enough to complete cluster finding, energy reconstruction, and energy selection in the ECal.

It is important to make sure that logically connected regions of the calorimeter will not be wired to the disjoint components of the cluster finder logic, because this would make cluster reconstruction much more difficult. The CTP board contains one FPGA chip collecting information from all 16 FADC modules installed into one VXS crate. That layout should allow searching for clusters in the upper and lower parts of the ECal independently. Unfortunately the total number of channels is slightly bigger than two VXS crates can accommodate. The remaining calorimeter channels will be connected to the FADCs in the third VXS crate, and cluster finding on the boundaries will be performed during the final trigger decision stage in the SSP board, where all the information from three VXS crates will be collected.

4.6.5.2 Level 1 Trigger

The Level 1 trigger system is based on the information which has been input to the ECal Flash ADCs. The first stage components of the trigger logic are incorporated into the Flash ADC board's FPGAs, while the final decision is made in a Crate Trigger Processors (CTPs). Three CTP boards and SSP board will collect data from two parts of the ECal (upper and lower) and from the Muon system, and perform cluster finding independently for those two parts. The trigger decision will be sent to the Trigger Supervisor implemented as a part of one of the TI boards. The Trigger Supervisor generates all necessary signals, and controls the entire DAQ system readout through the Trigger Interface units. The Trigger Interface (TI) units installed in every crate participate in the readout process. The system is free-running and driven by a 16 ns global clock with internal FPGA 4 ns clock.

As mentioned, the VXS crates shown in Figure 4.6.1 contain two trigger system components: processing units on the FADC boards (Figure 4.6.5.1) and Crate Trigger Processor (CTP) boards collecting data from the Flash ADCs over fast serial lines. The CTP boards search for clusters in the ECal, and send the results to the next stage of the trigger system. A signal processing algorithm running in the FADC board processing unit is shown in Figure 4.6.5.2.

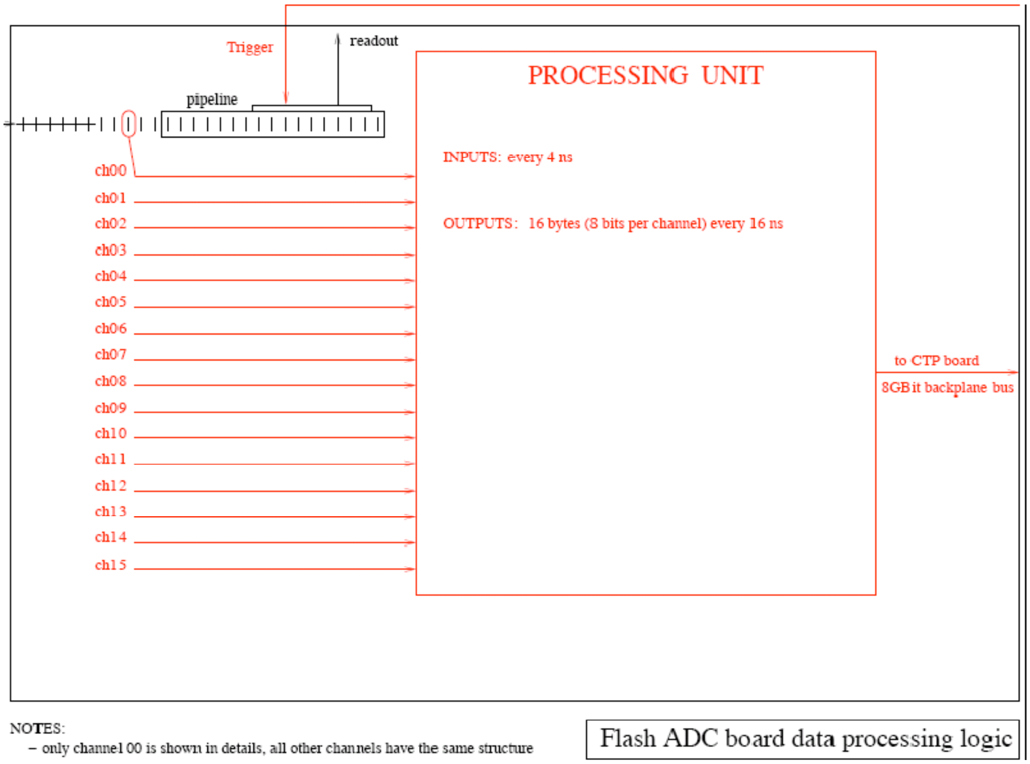

NOTES:
– only channel 00 is shown in details, all other channels have the same structure

Fig. 4.6.5.1 Processing unit on the FADC board

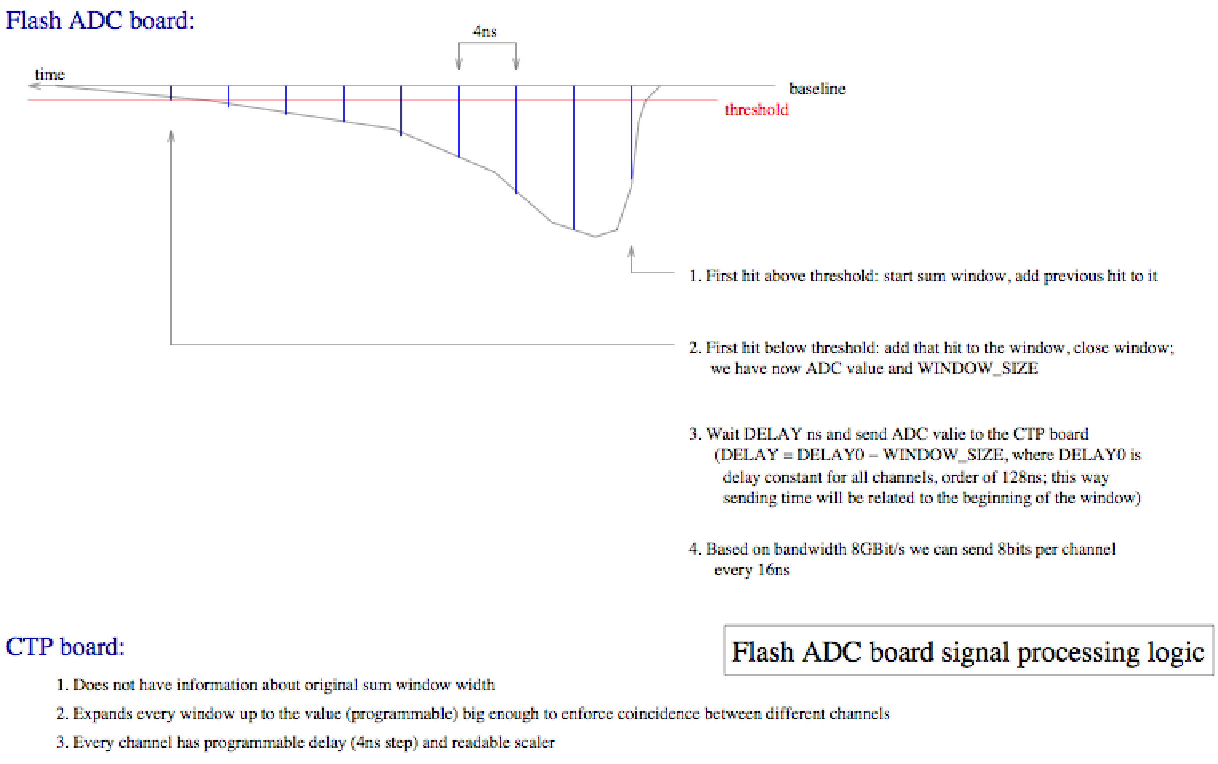

1. First hit above threshold: start sum window, add previous hit to it
2. First hit below threshold: add that hit to the window, close window; we have now ADC value and WINDOW_SIZE
3. Wait DELAY ns and send ADC valie to the CTP board (DELAY = DELAY0 – WINDOW_SIZE, where DELAY0 is delay constant for all channels, order of 128ns; this way sending time will be related to the beginning of the window)
4. Based on bandwidth 8GBit/s we can send 8bits per channel every 16ns

CTP board:

1. Does not have information about original sum window width
2. Expands every window up to the value (programmable) big enough to enforce coincidence between different channels
3. Every channel has programmable delay (4ns step) and readable scaler

Fig.4.6.5.2.Signal processing algorithm on the FADC board

4.6.5.3 Trigger Rate

The maximum trigger accept rate is 50 KHz.

4.6.5.4 Occupancy and Number of Samples for each Trigger

The assumption is that the system will run at 3 times the noise threshold. The occupancy is thus 0.135%. The above occupancy results in 92 SVT channels over threshold. Background studies show the average track multiplicity in an event is 10. On average, each track produces two "hit" strips in each of the two detectors constituting a layer. So there are 10(tracks) x 2(strips/track) x2 (detectors/layer) x 6 (layers) = 240 samples. Adding the noise pulses, gives 332 samples. Each of these channels over threshold results in 6 digitized values, which record the pulse heights in time bins adjacent to the hit in question, for subsequent pulse shape reconstruction and timing. Thus an average event has 332 x 6 = 1992 samples for each level 1 trigger signal.

4.6.6 Trigger Deadtime

The proposed trigger system is nearly deadtimeless. The trigger decision goes to the Trigger Supervisor every 16ns. The Trigger Supervisor can apply deadtime if necessary, for example on 'busy' or 'full' condition from the front end electronics. There is a limitation on the FADC board on the number of triggers received within a short time interval. For example, if four triggers arrived during about 200ns then the FADC will stop receiving new triggers until at least one of four is processed. We are not expecting to hit that limitation with our expected event rate ~50kHz.

4.6.7 Dataflow

4.6.7.1 SVT Data Rate and Volume

The amount of data for a ~40 MHz clock and a 50 KHz rate (APV25) is estimated as:

- Structure
  - Each chip 12-bit header (3 start, 8-bit address, 1 error) plus 10 bits/channel if 10-bit ADC is used
  - For each ASIC need additional 9 bit chip address
- Number of bits for each hit
  - 9-bit chip address (16-bit)
  - 12-bit header (16-bit)
  - 6 times 10-bit ADC value (72-bit) (assume 10-bit ADC for now since need bare minimum 8 bits)
  - 13 bytes (104 bits) (81 bit minimum)
- Data volume and rate

- 332 ASICs x 2 bytes chip address: 664 bytes
- 332 hits x 2 bytes header: 664 bytes
- 332 hits x 6 samples x 1.5 bytes: 2988 bytes

The resulting data rate is 4316 bytes x 50 KHz = 215.8 Mbytes/sec.

4.6.7.2 ECal Data Rate and Volume

A single FADC event contains 8 bytes of header for each FADC board, plus 4 bytes per accepted hit (hit means here integral over entire pulse).

With an estimate of 10 % acceptance rate, for each 16-channel ADC board that results in 8 bytes plus 1.6 x 4 bytes = 14.4 bytes average. At a trigger rate of 50 KHz the data rate is then 720 kbytes/sec for each board. A crate holding 16 FADC boards produces 11.5 Mbytes/sec. The limitation will be at the level of 50MB/s data rate from each VXS crate, so there is adequate headroom.

The total data rate from the ECal consisting of 35 FADC boards is 35 x 14.4 bytes x 50 KHz or 25.2 Mbytes/sec. (The total acceptance rate assumed is 10% of 640 channels or 64 channels for each trigger).

4.6.7.3 Muon Data Rate and Volume

The total data rate from the muon system which consists of 9 FADC boards is 9 x 14.4 bytes x 50 kHz, or 6.5 Mbytes/sec. (The total acceptance rate assumes 10% of 144 channels or 14 channels for each trigger.)

4.6.7.4 Event builder

The event builder is a program running on a server assembling the calorimeter, tracker, and muon data into complete events belonging to the same trigger event

4.6.8 Level 3 Sofware Filter

Level 3 will perform full event reconstruction on the Level 3 workstation. The level 3 filter must reduce the data rate received from the Eventbuilder from the expected ~ 215 + 25 + 6 = 246 Mbytes/sec incoming data rate to the less than 100 Mbytes/sec which is the maximum rate to tape. A factor of 4 is the minimum safety margin which should be planned for since the incoming rate is an estimate. In other words the level 3 filter needs to reduce the incoming rate by a factor of 8. An event recorder workstation serves as the event buffer before the events are transmitted to the computer center tape systems.

4.6.9 Monitoring and Calibration

Four practically independent monitoring systems are currently used in JLAB: Nagios-based computer and network monitoring, SmartSocket-based DAQ and Online monitoring, EPICS-based slow controls monitoring, and data monitoring. In addition, a few smaller hardware-specific systems are used. The data monitoring system includes visualization only with almost no alarm capabilities.

4.6.10 Readout Controllers, Computing and Network

Readout Controllers (ROCs) are installed in every VME, VME64X, VXS and ATCA crate. The ROCs are collecting data from the front-end boards, processing it and sending it to the Event Builder over the network. Currently mvme6100 controllers with a prpmc880 or pmc280 co-processor modules are employed. That configuration is fast enough to meet the HPS requirements. By the time of HPS startup, a new generation of multi-processor and multi-core ROCs will be available. ATCA crates will be equipped with commercially available multi-core CPU module.

A Foundry Router is currently used as the backbone of the DAQ system, providing 1GBit and 10GBit connections between components and to the JLAB Computer Center. The Event Builder, Event Recorder, and other critical DAQ components are running on 4-CPU Opteron-based servers, and that configuration is sufficient for HPS as well. ROCs are linked to the Foundry Router through smaller 1GBit switches with 4GBit uplinks. The HPS data storage system (RAID5) is sufficient for up to a 100~MByte/sec data rate. The performance of the link to the JLab Computer Center tape storage will be increased from current 30-40MByte/s to 100MByte/s.

5 Simulated Detector Performance

5.1 Trigger Simulations

The decision to process recorded data in ADCs and TDCs will come from a fast analysis of clusters and hits in the ECal and in the muon detector, respectively, by a Level-1 trigger processing system. Details of the Level-1 trigger electronics and organization were presented in the previous section. Here we discuss the trigger algorithm and the expected Level-1 trigger rate based on GEANT-4 simulations of the detector.

In the experiment, the search for the heavy photon will be conducted in (e^+e^-) or ($\mu^+\mu^-$) final states. The heavy photon is produced predominantly in the direction of the beam and therefore, for the most part, pairs of oppositely charged leptons will be well separated in opposite segments of the ECal. The level-1 trigger algorithm will search for two clusters of energy in opposite segments of the ECal (with respect to the beam direction). Similarly, the Level-1 trigger algorithm will look for minimum ionizing hits in muon hodoscopes in opposite sides from the beam direction. It is expected that the trigger rate from the ECal will be orders of magnitude higher compared to the muon system, and therefore only the ECal trigger selection process is discussed here.

The Bethe-Heitler process will generate most of the electron pairs, however, due to high rates (high accidental coincidences) and overlapping phase space, processes such as elastic scattering, photon bremsstrahlung and Moller scattering will contribute in the trigger (accidental final states (γe^-) and (e^-e^-)). The coincidence time used by the clustering algorithm for grouping hits in individual counters into clusters will play a crucial role in reducing the trigger rate.

5.1.1 GEANT-4 simulations of the ECal

For the study of the calorimeter and the trigger, a full GEANT4 model of the experiment was initiated. This model makes use of a modified version of the Gemc code [1] which is currently being developed to simulate the CLAS12 detector at Jefferson Laboratory. The Gemc code obtains all the geometry information for building up the virtual detector from a set of MySQL database tables, allowing for a very flexible framework to simulate any detector and making it easy to reconfigure the experiment. Many improvements made to the code for this project are ported back into the original Gemc code so both programs benefit from this development.

The current version of the full experiment simulation is stored in an svn repository [2] and freely available. All the key elements of the experiment are implemented: the first steering magnet and main analyzing magnet, the target, the silicon trackers, the main components of the vacuum system and the electromagnetic calorimeter. Figure 5.1.1.1 shows a rendering of the analyzing magnet, the tracker, and the ECal as used in the trigger studies.

Several geometry options have been investigated for the electromagnetic calorimeter in order to optimize its performance. Different arrangements of the calorimeter crystals were tried, with the final version having 5 rows of 46 lead-tungstate crystals and 3 rows of 16 lead-glass or "shashlyk" type calorimeter blocks for each of the top and bottom halves of the calorimeter. The calorimeter is separated from the beam vacuum by a 1 cm thick aluminum vacuum exit window (made transparent in the figure). The beam goes through a continuous vacuum from the vacuum box in the magnet to a vacuum enclosure made from 1 cm aluminum plates which is inserted between the top and bottom calorimeters. A different configuration, where the beam exited through a thin vacuum window into a region filled with helium for the calorimeter, was rejected due to the increased background rates. To further reduce the background rates without diminishing the structural integrity, a small area of the aluminum plates is cut out where the most intense part of the electron beam exits to the beam dump. A rendering of the simulated calorimeter is shown in Figure 5.1.1.2.

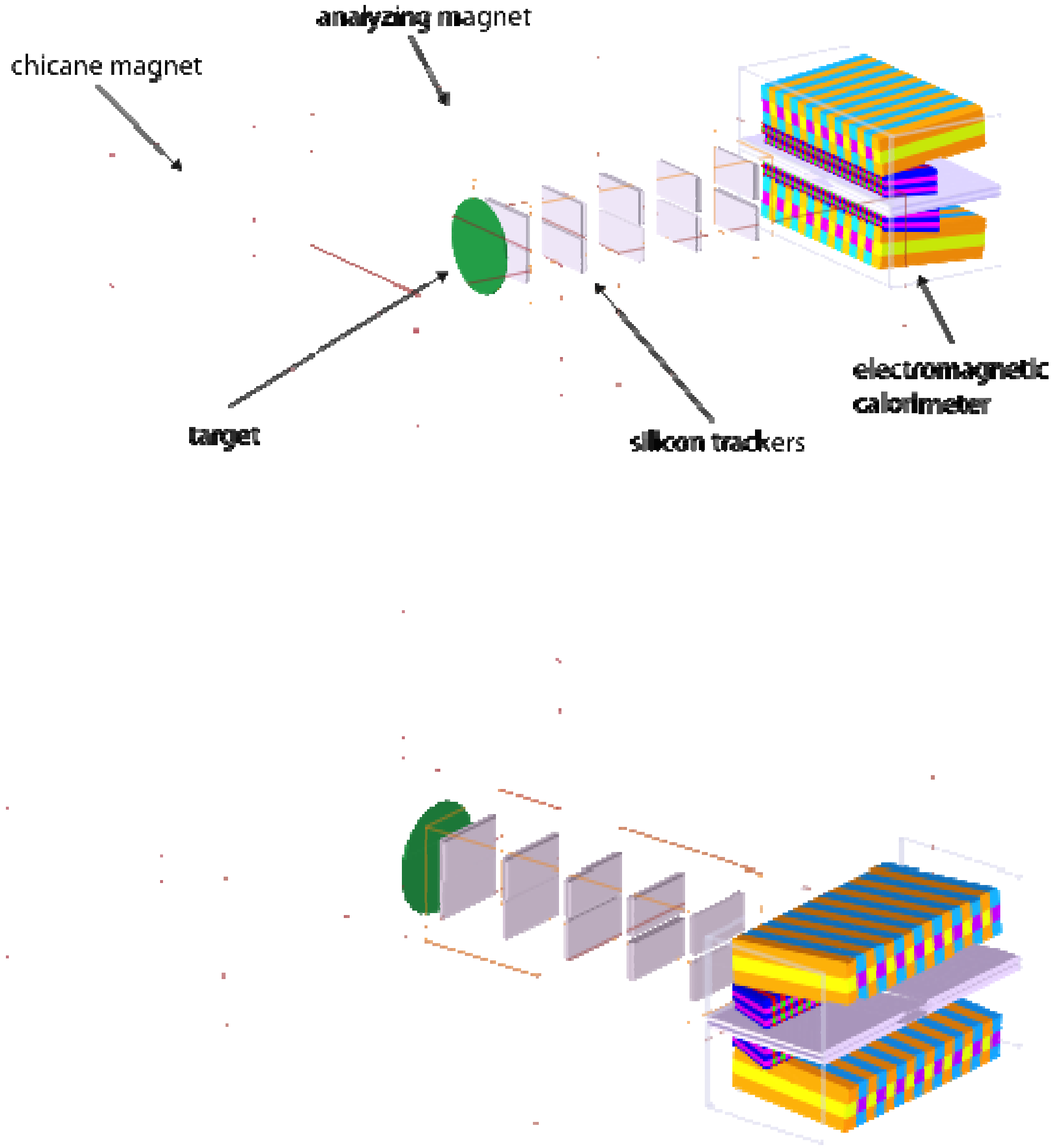

Figure 5.1.1.1. Rendering of the detector simulation used for trigger studies. The red boxes represent the magnets (outlined only), the green circle the target position, the gray rectangles represent a preliminary version of the silicon tracking layers, and the larger blue-gray rectangle represents the vacuum exit window (outlined only). The final object shows the calorimeter, with the crystals colored in alternate colors for clear visibility.

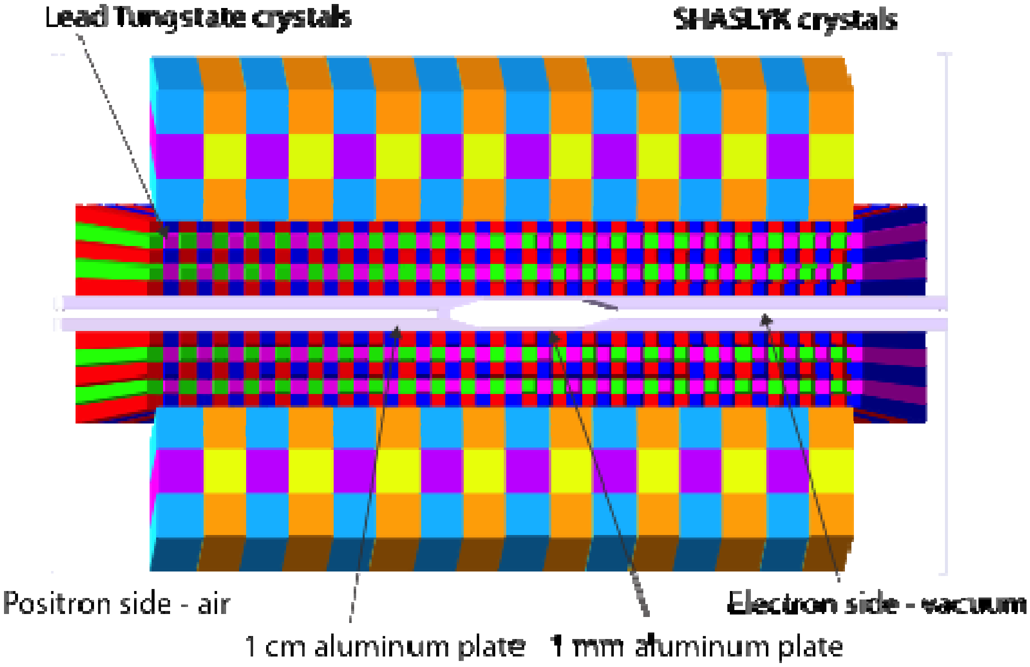

Figure 5.1.1.2. A rendering of the electromagnetic calorimeter setup looking down the beam line. The front exit window and side plates are rendered transparent to permit a view of the crystals and the vacuum plates.

To study the performance of the calorimeter and the trigger logic a large number of background events were simulated. Background events were generated by sending 10,000 5.5 GeV electrons through the 0.25% X_0 tungsten target (equivalent to 4ns of a 400 nA beam) and letting the GEANT4 physics models generate the expected backgrounds (scattered electrons, produced photons and other particles). The physics models used in this simulation include all electromagnetic and hadronic processes implemented in GEANT4. To simulate longer integration time, several events were added together. A significant amount of simulation data was also generated with a 25 ns time window and consistency was checked between the two data sets.

For the trigger studies, input events were used that were generated with MadGraph/MadEvent. These events simulated A′ masses of 50 MeV, 100 MeV, 200 MeV, 250 MeV, 300 MeV, 400 MeV, 500 MeV and 600 MeV. The output files of these simulations could be merged with the background simulation output files to create realistic data samples for different scenarios.

5.1.2 Calorimeter Performance

Two aspects of the calorimeter performance were studied with the simulation. The hit rates on the individual crystals were looked at to make sure these rates will be within a reasonable range for the expected running conditions, and the expected trigger rates for simulated A′ particles and for background events were studied to make sure they do not exceed the maximum allowable DAQ trigger rate. This section details the hit rates, the next section the trigger rates.

As one would expect, the highest rates occur on the crystals that are closest to the exiting electron beam. A map of the percentage of events with at least one hit, the hit occupation, for each crystal, using a time integration window of 32 ns and a hit threshold of 10 MeV, is shown in Figure 5.1.2.1. The maximum hit occupation occurs for crystal number 4 in the first row, with nearly 100% occupancy.

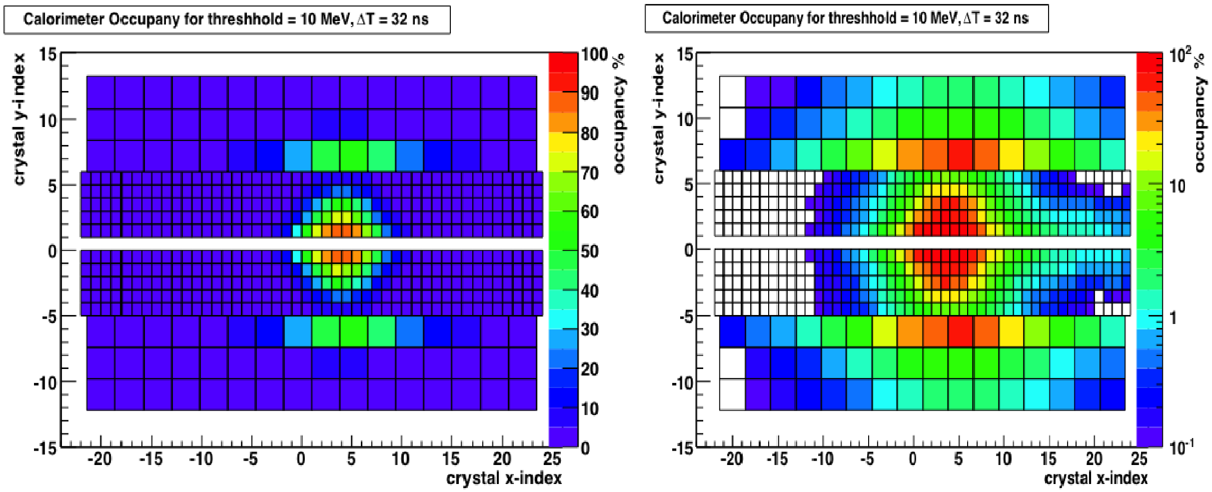

Figure 5.1.2.1 Hit occupancies in the electromagnetic calorimeter for a time window of 32 ns and a threshold of 10 MeV. The figure on the left has a linear z-scale, the figure on the right is identical except for the logarithmic z-scale. Note that the x and y axis are the index of the crystal, not the position. The figure clearly shows that only a few crystals in the first row around the beam exit see very high occupancies.

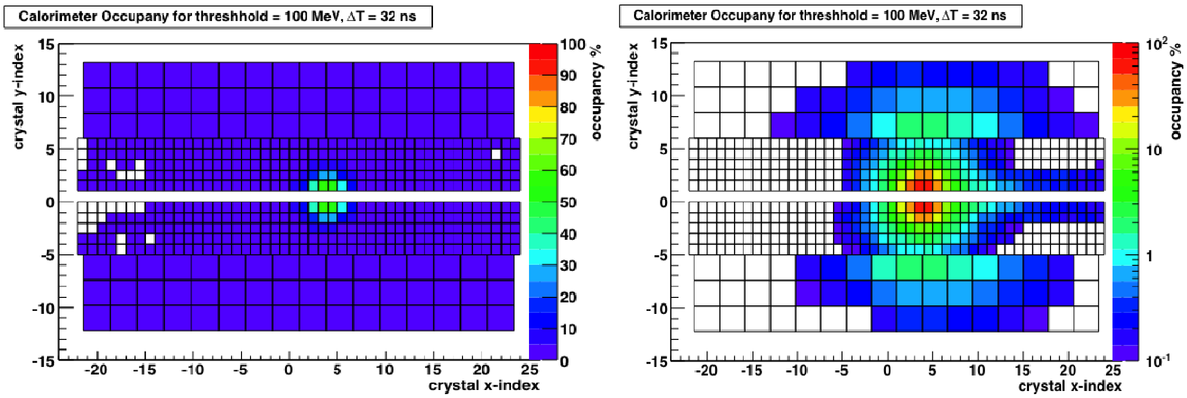

Figure 5.1.2.2 Hit occupancies in the electromagnetic calorimeter for a time window of 32 ns and a threshold of 100 MeV. The figure on the left has a linear z-scale, the figure on the right is identical except for the logarithmic z-scale. Note that the x and y axis are the index of the crystal, not the position. The increased threshold reduces the occupancies on the hottest crystal (#4 row 1) to around 50%.

Increasing the threshold on the crystals improves the occupancy significantly, as can be seen in Figure 5.1.2.2. If the time integration window is also reduced, the crystal occupancies come down to reasonable levels, even for the hottest crystal, see Figure 5.1.2.3.

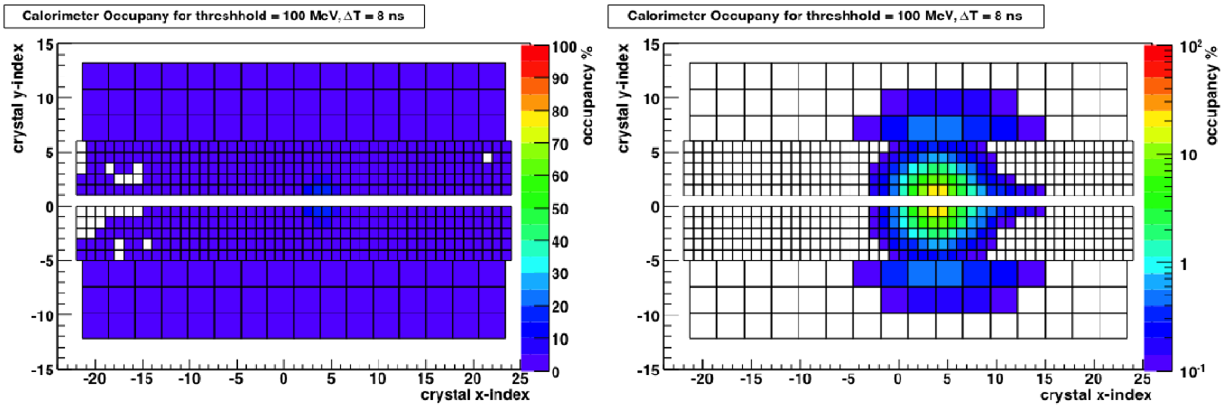

Figure 5.1.2.3 Hit occupancies in the electromagnetic calorimeter for a time window of 8 ns and a threshold of 100 MeV. The figure on the left has a linear z-scale, the figure on the right is identical except for the logarithmic z-scale. Note that the x and y axis are the index of the crystal, not the position. The reduced time integration window further reduces the occupancies on the crystals to a maximum around 20%. If experimental conditions dictate it, the threshold could be increased further on individual crystals.

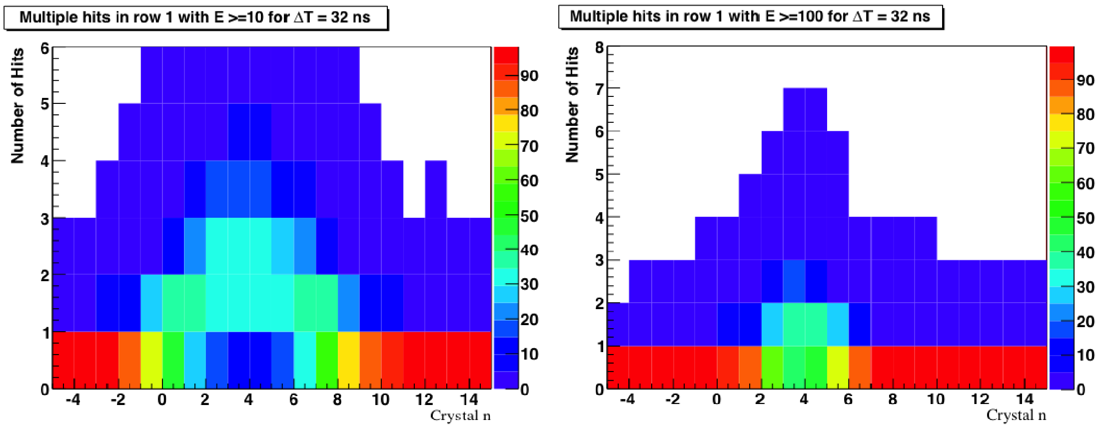

Figure 5.1.2.4 Hit multiplicities for the first row of crystals around the area of the beam exit. The left plot is for a threshold of 10 MeV, the right plot for threshold of 100 MeV. The y-axis shows the number of hits in the 32 ns time window, the z-axis (colors) shows the percentage of events with this hit occupancy.

A more detailed picture of the running conditions for the crystals of the electromagnetic calorimeter can be obtained by looking at the hit multiplicities, the number of hits in a specified time window with energies above some threshold. Figure 5.1.2.4 shows the multiplicity for crystals in row 1 and a time window of 32 ns, with a threshold of 10 MeV (left) and a threshold of 100 MeV (right). The y-axis indicates the number of hits in an event with the specified time window, and the color indicates the percentage of the events where the crystal had that many hits, thus a sum over a column of the histogram adds up to 100%. One can see that for a threshold of 10 MeV and a time window of 32 ns, crystals number 3 and 4 have 2 hits per event for 30% of the time, and 3 hits for as many as 15% of the events. When the threshold is raised to 100 MeV, the number of events with 2 hits is reduced to fewer than 20%. A plot of the projection on to the y-axis for crystal 4 is shown in Figure 5.1.2.5 (light blue line.) This figure illustrates how reducing the time window reduces the multiplicity on the crystal, exactly as expected. At a threshold of 100 MeV and time integration windows shorter than 16 ns, the multiplicities on the hottest crystal are reasonable, less than 5% of the events.

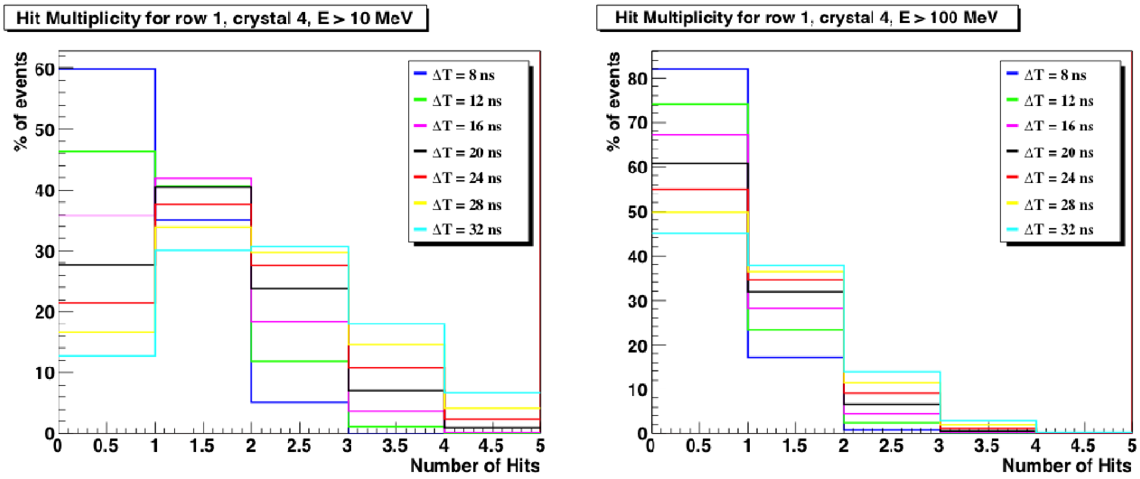

Figure 5.1.2.5. Projection onto the y-axis of the multiplicities of figure 5 for crystal number 4 (light blue), and similar projections for shorter time windows.

5.1.3 Level 1 trigger simulations

To accurately estimate trigger rates, a Level 1 trigger algorithm was developed and optimized using simulated background data and simulated A' events with masses ranging from 50 MeV to 700 MeV. The events were processed with the full GEANT4 based simulation described in the previous section. For the background events, two simulated 4 ns events at 400 nA were summed to simulate a single 8 ns event. This allowed for the simulation of background events with a trigger coincidence window of 8 ns.

To accomplish the short coincidence timing, the CTP will run in a modified mode. In the standard operational mode, with a predefined integration time and delay, the time of the hit reported to the CTP will have about 16 ns jitter. With a 16 ns time resolution for each channel, a reasonable minimum time window for triggering cannot be less than 32 ns (2 trigger time buckets). To shorten the trigger time window the CTP can use 6 bits for the energy sum (FADC sum), instead of the standard 8 bits, leaving two remaining bits of an 8 bit word to determine the 4 ns clock cycle when summing started. In this arrangement, time jitter at the CTP for each channel will be 4 ns and the coincidence time between channels can be reduced to two 4 ns clock cycles, 8ns. Differences in signal propagation times between channels can be accommodated using internal delays in CTP (with 4 ns steps).

The first step in the Level 1 trigger algorithm is the identification of clusters in the electromagnetic calorimeter. A very simple cluster finding algorithm was used which maximized the number of clusters that would be found. The cluster finding algorithm followed the following logic steps:

1) For each hit in the calorimeter with at least 50 MeV of energy,
2) Search the 3x3 square around the hit for other hits (smaller regions for hits on borders).
3) If a hit with more energy is found, the original hit is not the cluster center,
4) Else add up the energies of the hits in the 3x3 square if these hits were within 8 ns of the center hit.

The resulting cluster samples were then studied to define the most effective trigger, for which the criteria are the largest acceptance of simulated A′ events and the highest rejection of background events. Thus the ratio of accepted A′ events to background events was maximized, with the additional constraint that the background trigger rate would not exceed 20 kHz.

At the lowest level, a trigger required two good clusters in opposite quadrants of the calorimeter. Many events would have multiple clusters in at least one of the two quadrants, in which case all combinations of clusters were tried for trigger candidates. This double counting is not shown in the first row of the table, and eliminated in the last step. Table 5.1.3.1 shows each of the subsequent cuts and their effect on the number of accepted A′ trigger candidates together with the effect on the background trigger candidates. The simulated A′ mass used was 250 MeV. Numbers are given as a percentage of the total number of simulated events. A more detailed description of each trigger selection cuts follows.

Trigger Cut.	A′ Acceptance	Background Acceptance	Estimated Background rate
Events with least two opposite clusters	44.6%	1.26%	1.6 MHz
Cluster energy > 500MeV and < 4400 MeV	46.4 %	0.239%	0.3 MHz
Energy sum < 5100 MeV	46.4 %	0.0959%	120 kHz
Energy difference < 3200 MeV	46.1 %	0.0823%	102 kHz
Lower energy - distance slope cut	45.4%	0.0601%	75 kHz
Clusters coplanar to 45°	44.6%	0.0344%	43 kHz
Eliminate crystals in row 1, column 0,3,4	41.3 %	0.0158%	20 kHz
Not counting double triggers	38.1%	0.0135%	17 kHz

Table 5.1.3.1.Trigger selection cuts and their effect on the A’ acceptance and background rate, as a percentage of the total number of simulated events. An A’ mass of 250 MeV was used for this illustration.

As the table shows, a large fraction (1.26%) of the background events have at least two clusters in opposite quadrants of the detector. A further refinement requires each of the clusters to have an energy of at least 500 MeV, but no more than 4.4 GeV. This eliminates low energy background hits and hits from electrons with energies close to the beam energy, while having little effect on the A′ acceptance. (Note that in the table the counting of the double triggers give the false impression that the acceptance is slightly higher after this cut.) The fraction of accepted background events now drops to 0.239%.

Next a two dimensional cut is made in the energy (of the hit) – distance (of the hit from the beam) plane. These distributions are shown in Figure 5.1.3.1. The previously mentioned lower energy cut for the clusters is shown as the vertical red line. The histograms show that an additional cut for the least energetic cluster along the red sloped line (E+5d < 1000), effectively eliminates background events, reducing the background acceptance to 0.06%.

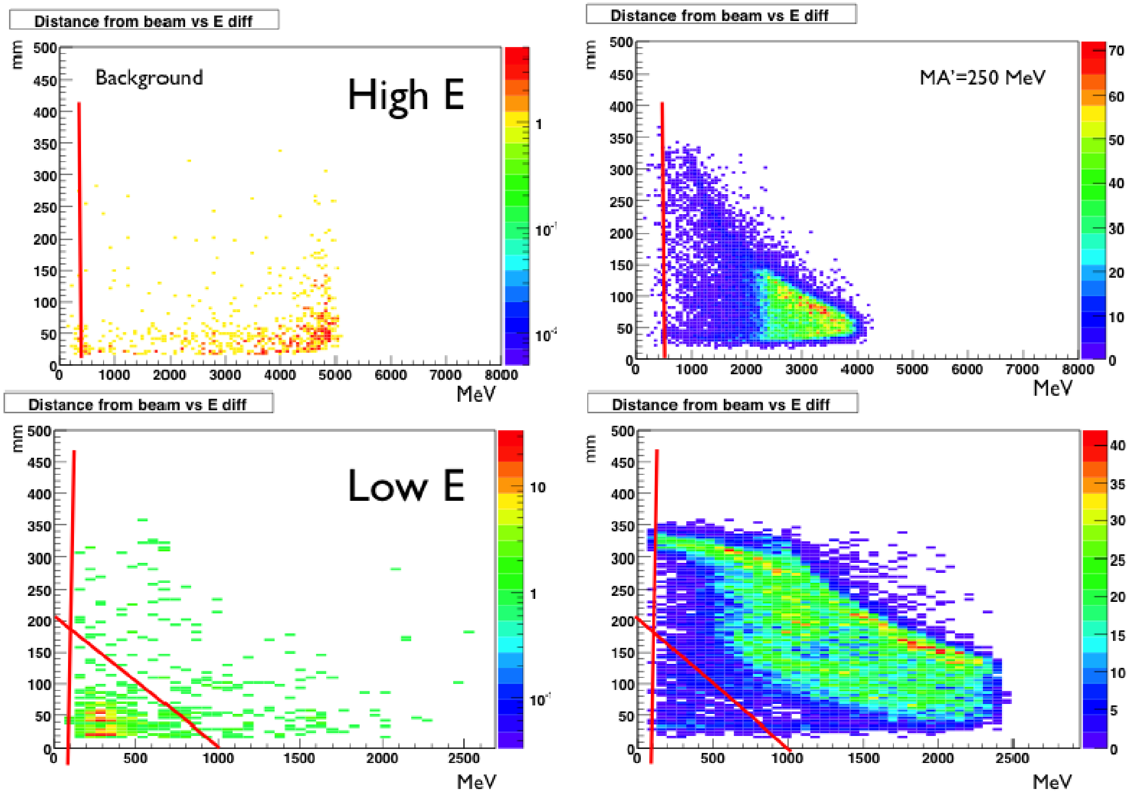

Figure 5.1.3.1. The distance of the cluster center to the beam is plotted versus the energy of the cluster for the most energetic cluster of the trigger pair (top) and least energetic pair (bottom). The left column plots background events, the right hand column plots simulated A' events with a mass of 250 MeV. As can be seen from the plot, an effective cut to eliminate background events without affecting the A' acceptance is indicated by the red lines.

The requirement that the two clusters are coplanar with the beam within 45 degrees further eliminates background events, leaving 0.034%.

These cuts still leave us with a trigger rate of 43 kHz, which is too close to the maximum allowable trigger rate of 50 kHz. Removing the crystals with the highest occupancies from the trigger (crystals in row 1, columns 0, 3 and 4) reduces the trigger acceptance 0.016%. Without counting the double triggers in the same 8 ns, the final acceptance is 0.0135%, which corresponds to a trigger rate of 16.9 ± 1.0 kHz.

The same trigger algorithm was run on simulated data for a number of different A′ masses. The resulting acceptance estimates are listed in Table 5.1.3.2. The proposed trigger algorithm retains high efficiency for signal events and suppresses the background triggers by almost a factor of 100.

A′ Mass (MeV)	50	100	200	250	300	400	500	600
Ecal	3.1%	18.5%	33.7%	38.1%	40.5%	36.3%	30.3%	25.1%

Table 5.1.3.2. Trigger acceptance estimates for different A' masses.

The trigger rates for trident backgrounds (Sec 3.2 and 3.3) were estimated using radiative and Bethe-Heitler events generated with MadGraph/MadEvents and incoherent (two-step) trident events generated with EGS5. Although these trident processes have a large cross section, a large fraction of events do not satisfy the trigger conditions either because electrons/positrons are produced in a small polar angle or the energies are soft. Table 5.1.3.3 summarizes the trident trigger rates.

Trident	Estimated trigger rate
Coherent trident	
Bethe-Heitler	6.0 kHz
Radiative	130 Hz
Incoherent trident	230 Hz

Table 5.1.3.3 Trident trigger rates

5.1.4 References

1. See http://clasweb.jlab.org/wiki/index.php/Gemc
2. Anonymous checkout of all the code: “svn checkout svn://gourd.unh.edu/Aprime/trunk”.

5.2 Tracker Occupancies and Acceptance

Figure 5.2.1 shows the distribution of charged particle hits in Si tracker layer 1 which is located 10 cm from the target as generated by EGS5. The target thickness is 0.25% X_0, and the beam axis is at x=y=0. Multiple Coulomb scattered beam electrons are confined within 0.5 cm of the beam axis, while the low energy Moller electrons are distributed in a parabolic shape. There are very few positrons. From these distributions, the detector occupancy in the horizontal Si strip sensor in the 7.5 ns time window is calculated for a 400 nA beam current and five different target thicknesses, 1.0% X_0, 0.5% X_0, 0.25% X_0, 0.1% X_0, and 0.05% X_0, and is shown in Figure 5.2.2. As described in Section 4.3.4, the dead zone is defined by using a criterion that the maximum occupancy in Layer 1 is 1%. For a 0.25% X_0 target and 400 nA beam, the occupancy is 1% at a distance of 1.5mm from the beam in Layer 1, which corresponds to a dead zone of ± 15 mrad. As long as the product of target thickness (T) and beam current (I) is constant, the same A′ production rate is maintained. Since the multiple scattering and hence the effective beam size is reduced in a thinner target, it is advantageous to use a thinner target and a higher current. Using the constraint that the occupancy is 1% at 15 mrad, we find the beam current I which gives this occupancy for each of several potential target thicknesses T. The quantity $(I \cdot T)^{1/2}$, which is approximately proportional to the sensitivity $S/\sqrt{B}$, is given in Table 5.2.1, showing how the sensitivity improves as the target thickness decreases. Hall B is limited to maximum currents of about 800 nA, which limits how thin a target is practical.

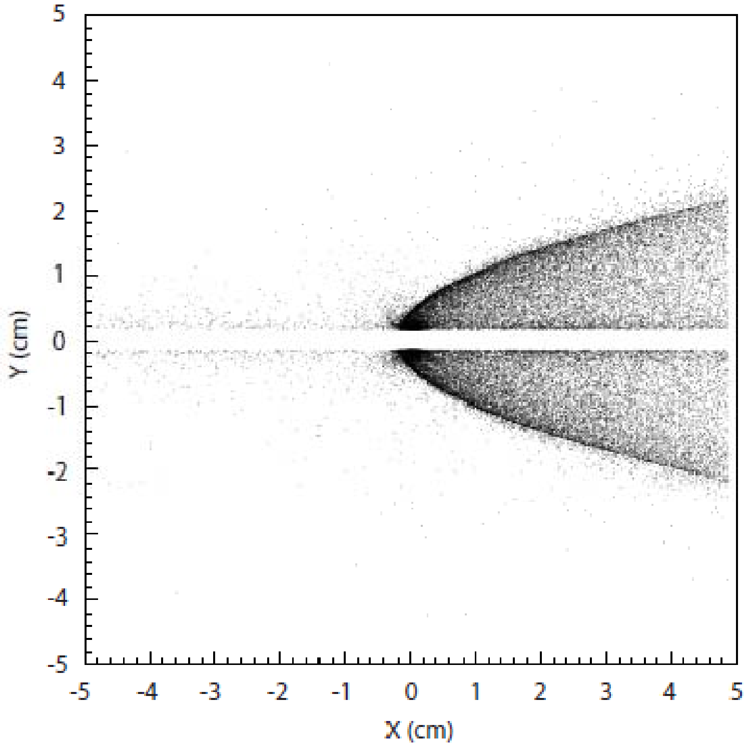

Figure 5.2.1 Charged particle distribution in layer 1

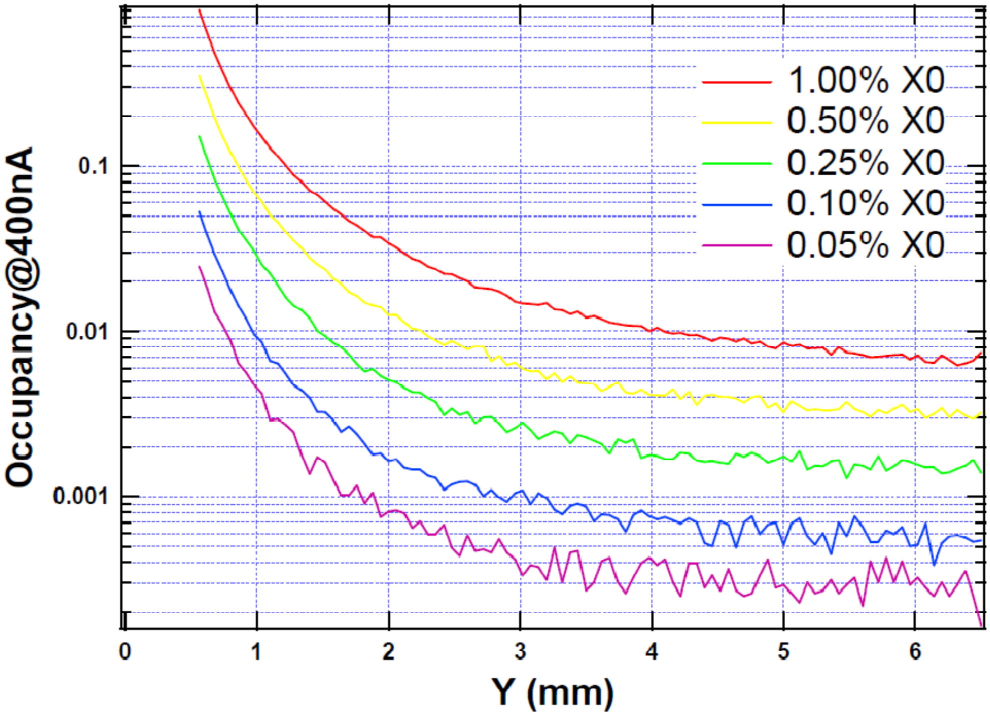

Figure 5.2.2 Silicon sensor layer 1 occupancy at 400 nA vs distance from the beam in mm.

Target thickness (% X_0)	Beam Current (nA)	$\propto S/\sqrt{B}$
1.0	62	4.63
0.5	142	4.98
0.25	400	5.92
0.10	1200	6.48
0.05	2400	6.48

Table 5.2.1. Beam current yielding 1% occupancy in Silicon sensor layer 1 for various target thicknesses, and the relative experimental sensitivities which result.

Once the dead zone is determined, the tracker acceptance can be calculated by requiring that both e+ and e- from A′ decay are detected in the first five silicon layers. The tracker parameters given in Table 4.3.4.1 are used. Figure 5.2.3 shows the tracker acceptance as a function of A′ mass at a beam energy of 5.5 GeV for several A′ decay lengths, including when the A′ decays at the target (Zv = 0 cm). The tracker has useful acceptance from 50 MeV to 1000 MeV at 5.5 GeV; lower (higher) beam energies can probe A′s of lower (higher) mass. At the lower mass side, the acceptance is limited by the dead zone, while the transverse tracker size limits the acceptance at the higher mass side. As the A′ decay distance becomes longer, the first-five layer acceptance gets smaller as the A′ decay products remain within the dead zone at Layer 1. To detect these long-lived A′ decays, the last four silicon layers can be used. Figure 5.2.3 shows the last-four layer acceptance when A′ decays at 10 cm and 20 cm from the target. The tracker design based on six silicon layers has a large acceptance over a wide range of decay lengths.

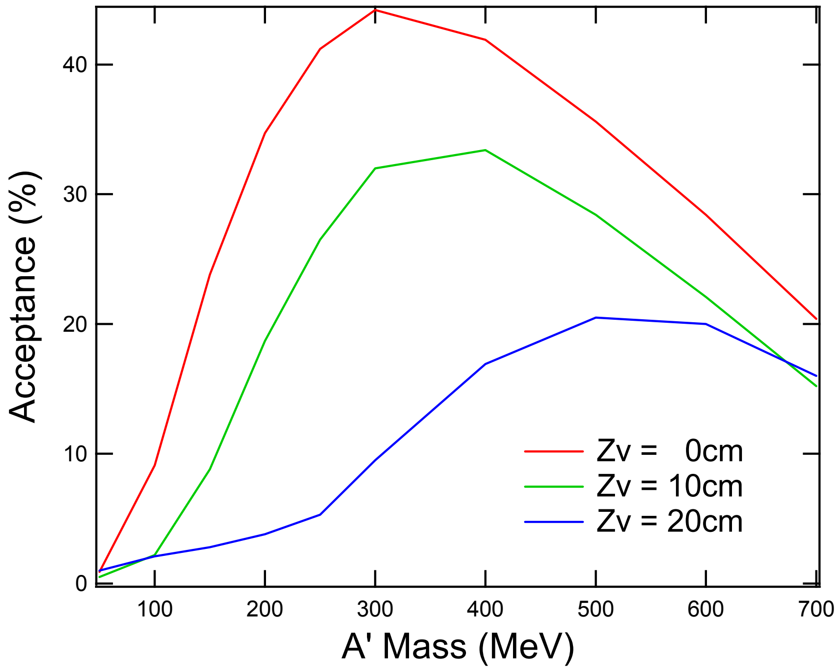

Figure 5.2.3 Tracker acceptance as a function of A' mass for several A' decay lengths. The beam energy is 5.5 GeV.

5.3 **Tracking Performance**

We use a GEANT4 Si tracker simulation based on SLAC's org.lcsim infrastructure for full simulation of the passage of charged and neutral particles through the target and tracker. It creates realistic energy deposits in the silicon microstrip detectors, accounts for dead material, accurately digitizes energy deposits into strip hits, creates clusters, and performs track finding and reconstruction. This simulation is used to get realistic estimates of tracking pattern recognition efficiencies and purities in the presence of all the expected electromagnetic backgrounds, and to evaluate momentum, invariant mass, and vertex resolution.

The standard pattern recognition algorithm is designed to find tracks efficiently using strip hits in the tracker. The first step in track finding is to convert the digitized hits into a common hit format. This format encapsulates all the information needed by the standard pattern recognition algorithm, while insulating the track finding from differences and changes in the digitization algorithms. We consider two types of hits: axial strip hits that have one measured coordinate and one bounded coordinate and stereo hits formed from a pair of strip hits in the same tracker plane. Track finding is controlled by a set of strategies. A strategy consists of the list of detector layers to be used, the role of each layer (seed, confirm, or extend), kinematic constraints (momentum, impact parameters), requirements on the number of hits, and the χ^2 cut.

The track finding algorithm is exhaustive in the sense that all combinations of hits that could potentially lead to a successful track fit are considered. The algorithm proceeds in four steps:

1. The first step is to form a 3-hit track seed candidate by taking all 3-hit combinations possible among the 3 seed layers. A helix fit is performed on the seed candidate, and those seeds that fail the χ^2 cut are eliminated. The helix is defined by five parameters: the curvature, angle and distance from the z-axis at the DOCA (ω, ϕ_0, and d_0 respectively) describing the circular part of the helix, and the slope and point on the a-axis at the DOCA ($\tan\lambda$ and Z_0) describing the trajectory in the s-z plane.
2. The second step tries to "confirm" the seed by adding additional hit(s) from the confirm layer(s). A helix fit is performed on the new seeds and those that fail the χ^2 cut are eliminated. Typically, it is found that good performance is achieved with one confirmation layer.
3. The third step seeks to "extend" a confirmed seed by trying to add additional hits from the extend layers. Each time a new hit is considered, a helix fit is performed and the hit is discarded if it fails the χ^2 cut. If no hits in a given extend layer give a satisfactory helix fit, then the original track seed is kept and the next extend layer is tried.
4. Track seeds that meet the strategy's requirement on the minimum number of hits are merged to form a list of distinct tracks. Two track candidates are allowed to share a single hit, but if a track candidate shares more than one hit with another candidate, an arbitration scheme is used to select the better candidate. Precedence is given to the candidate with the greatest number of hits, while the candidate with smaller χ^2 is selected when the number of hits is equal.

Consistency checks and hit sorting algorithms are used to minimize the number of helix fits performed, substantially improving the performance of the algorithm. Furthermore, a "bad hit " χ^2 cut is used to identify track candidates with an outlier hit and allows preference to be given to track candidates without an outlier hit. A key component of the pattern recognition algorithm is a fast helix fitter. The helix fitter takes as input 3 or more tracker hits. The hits can be any combination of axial strip or stereo hits in the barrel. The fast fitter is used to estimate the helix parameters and helix fit χ^2. First, a circle fit to the x,y coordinates of all hits is performed using the Karimäki algorithm to determine the helix parameters ω, ϕ_0, and d_0. If there are two or more stereo hits, then a line fit in the s-z plane is used to determine the Z_0 and $\tan\lambda$¸ helix parameters.

For all of the particles we will be measuring, the multiple scattering errors will exceed the intrinsic hit resolution. Multiple scattering errors for both the active and dead materials are estimated and included in the helix fit. Correlations in the multiple scattering errors are ignored, leading to an under-estimate of the helix parameter errors by a factor of ≈1.5. For stereo hits, full account is taken for the separation between the two stereo layers in the calculation of both the hit position and hit covariance matrix.

The performance of the standard pattern recognition algorithm is shown in the sections below. Unless otherwise noted, the tracking strategies require 1 confirmation hit, stereo hits in at least the first four tracker planes (the last plane is added if it passes the extend criteria), $0.5 < P_z < 5.5$ GeV/c, and both the x and y distance of closest approach to the beam axis are less than 0.5 mm.

In order to study the tracking performance of the detector (described below), we use samples of A′ events at a variety of energies and decay lengths. On top of each event, we overlay backgrounds produced by the passage of beam electrons equivalent to 400nA in 7.5ns on a 0.25% X_0 target, with a beamspot of radius 10um. Most of the studies have been performed with a large sample of 200 MeV A′ events decaying at the target.

5.3.1 Tracking Efficiency, Pattern Recognition and Fake Rates

Due to the requirements imposed on the tracks, the efficiency for finding tracks in the geometric acceptance is not 1. The plot below (Figure 5.3.1.1) shows the efficiency to find an electron (or positron) from an A′ decay which deposits energy in all six planes of the tracker, and thus should be found by the tracking algorithm, as a function of track momentum. The bulk of the inefficiency comes from the cut on the total χ^2. The average track reconstruction efficiency is 85%.

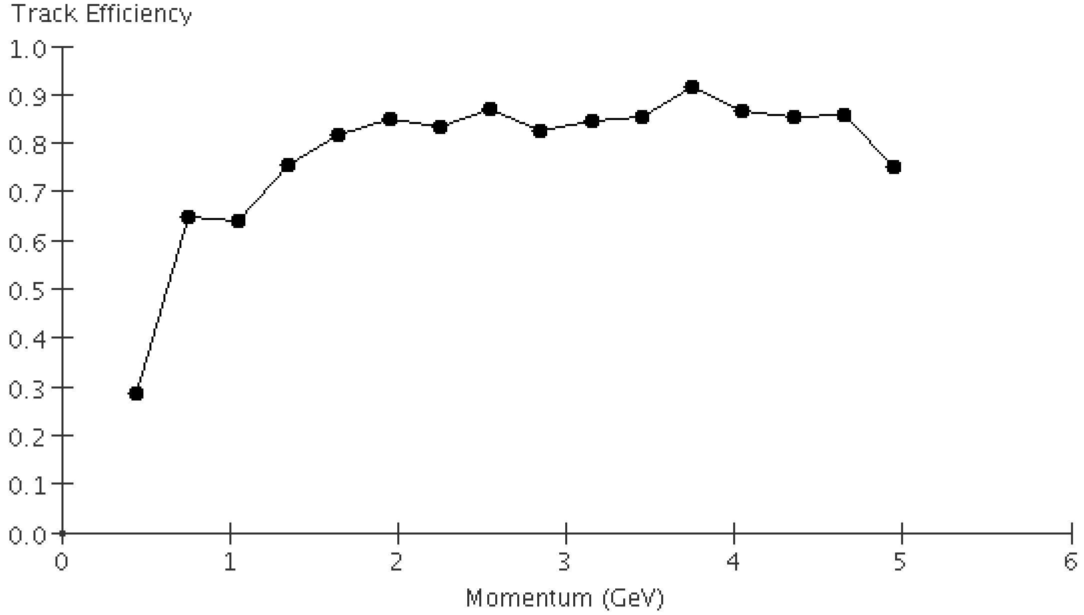

Figure 5.3.1.1: Track finding efficiency versus momentum for electrons in the detector.

Of the reconstructed tracks, a small percentage of them include a hit that is not from the correct electron. These "bad" hits may be from one of the high energy beam electrons scattered from the target into the detector or from a lower energy secondary. The upper plot of Figure 5.3.1.2. shows the number of bad hits/track for both the electron and positron from the A′ decay. The number of tracks with 0 bad hits is >95% and the positrons are slightly cleaner since occupancy of the positron side of the detector is smaller. The lower plot of Figure 5.3.1.2 shows the layer number of the bad hit. They tend to be in the closer layers, although there are more in layer 3 (a non-bend plane layer) than in layer 2. We'll show how these bad hits affect the track parameters in the next section.

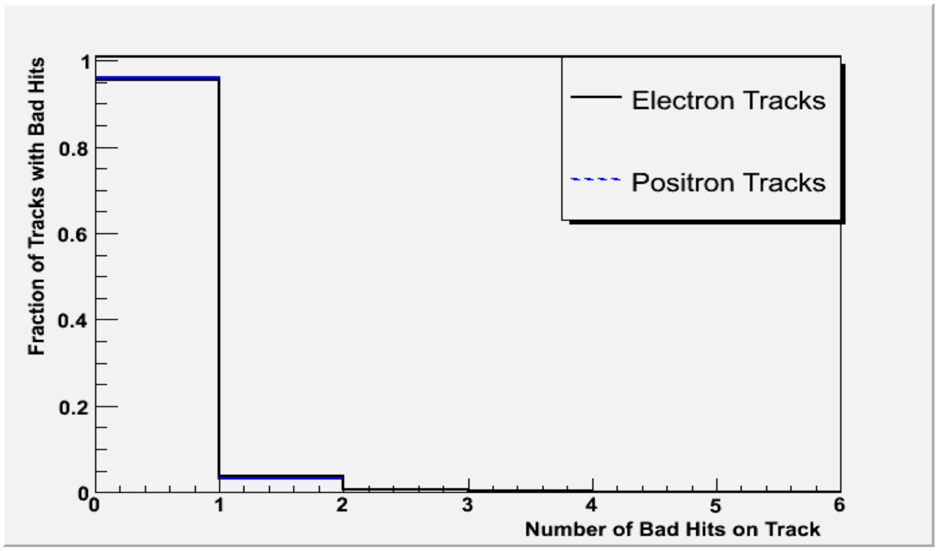

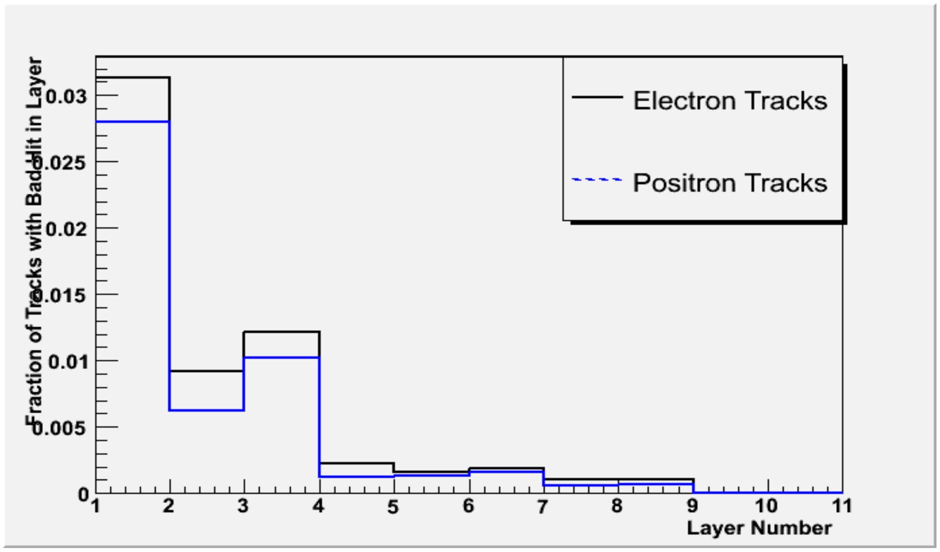

Figure 5.3.1.2: The number of bad hits (top) and the layer number of the bad hit (bottom) for electron (black) and positron (blue) tracks prior to vertex selection.

5.3.2 Track Momentum and Spatial Resolution

The momentum resolution is shown in Figure 5.3.2.1 as a function of momentum for tracks with 0 bad hits and for tracks with one or more. The momentum resolution for well reconstructed tracks is σ_P = 0.01p + .008 (GeV/c) Generally, tracks with only bad hits in the non-bend layers have the same momentum resolution as well reconstructed tracks; only bad hits in the bend layers affect the momentum.

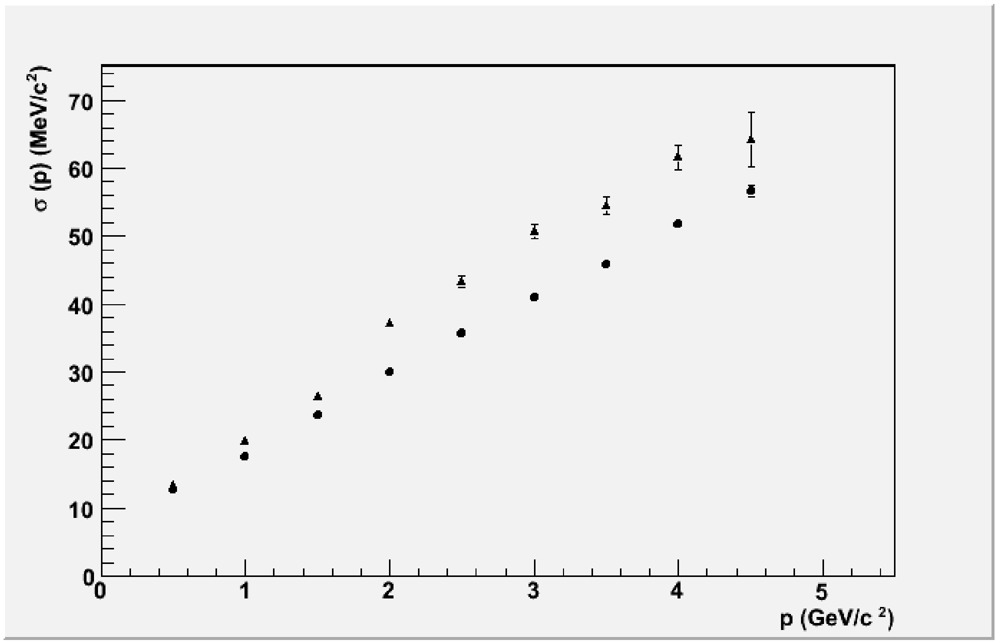

Figure 5.3.2.1: Momentum resolution versus momentum for 0 bad hit tracks (circles) and tracks with 1 or more bad hits (triangles). NOTE: redo this plot with tracks with bad hits in bend-plane layers.

One quantity we use to determine track quality is the distance of closest approach to the beam axis. We use this instead of DOCA to the target beam spot since we are interested in long lived decays and tracks from those will not point back to the target. We separate the distance into the bend plane (XOCA) and non-bend plane (YOCA) distances. Below, in Figure 5.3.2.2, is the resolution of these quantities as function of momentum for tracks with 0 bad hits and for tracks with 1 or more bad hits. The resolution for well-reconstructed tracks is ~50μm (30 μm) in XOCA (YOCA) and increases at low momentum.

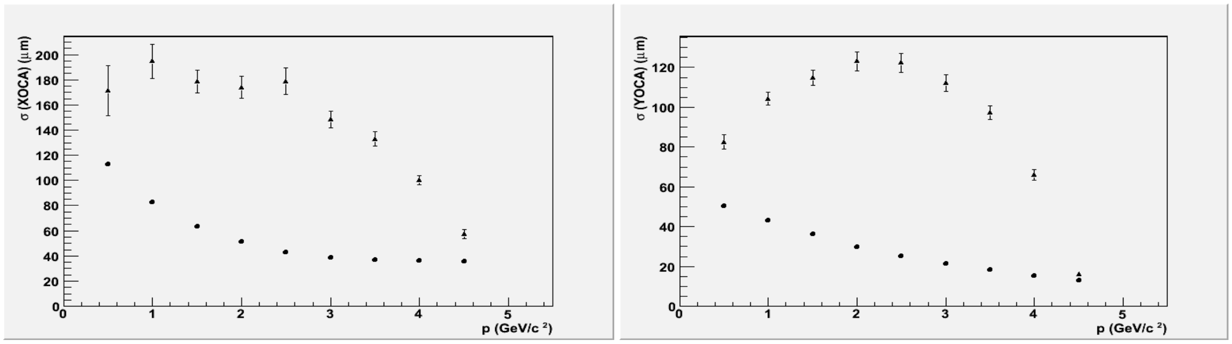

Figure 5.3.2.2: XOCA (left) and YOCA (right) resolution versus track momentum for 0 bad hit tracks (dots) and 1-or-more bad hit tracks (triangles).

For each electron/positron pair reconstructed in the tracker, we compute the invariant mass based on the measured momenta of the tracks. The mass resolution depends on the invariant mass of the pair and is shown in Figure 5.3.2.3.

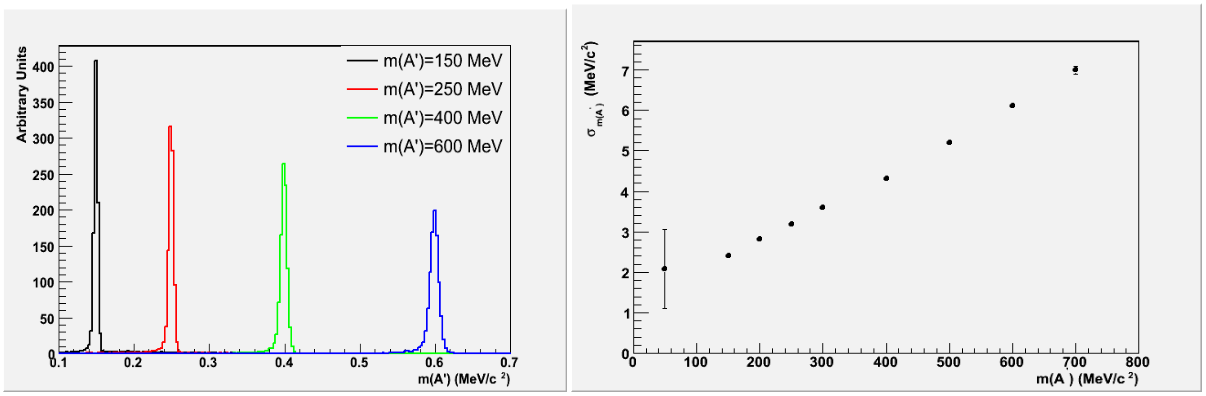

Figure 5.3.2.3 The mass (right) and vertex (left) resolution as a function of the A' mass, decaying at the origin.

For long lived A′ decays, the position of the decay vertex is an important discriminating variable. The dominant background to A′ production is radiative events which originate in the target. Distinguishing A′ decays from the background therefore depends on the vertex resolution and in particular on the tails of the vertex distribution. In order to study the tails we use a sample of ~200 million 200MeV A′ events decaying promptly overlaid on top of the simulated beam background events.

The vertex position of each pair is calculated using a method derived from the SQUAW kinematic fitting program. The method uses the measured helix parameters and their correlations to determine the most likely decay position of the A′. In addition, the vertex is constrained to be consistent with the A′ trajectory, which originates in the 10um beamspot at the target, and moves off in the direction given by the measured A′ momentum.

Even for prompt decays, the z vertex position (V_z) distribution of all reconstructed e+e− pairs (solid black histogram, Figure 5.3.2.4) shows a long tail, still significant beyond 5cm. This tail is primarily comprised of events where one or both of the tracks use one or more bad hits. Fortunately there are a number of quantities we can use to minimize the tails. Namely, for purposes of this proposal, we make the following cuts:

- The χ^2 of each track is less than 20
- The total momentum of the A′ candidate is less than the beam energy
- A very loose cut on the reconstructed vertex position $|V_x|<400$um and $|V_y|<400$um
- A χ^2 cut on the vertex fit of less than 15

These cuts remove all of the tail past ~1.5cm (points with errors in Figure 5.3.2.4) while retaining ~60% of the e^+e^- pairs from the A′ candidate. The RMS of the final resolution distribution is 1.14cm while the high side tails of the distribution (i.e. the background for the long lived A′ decays) contain $3.6\text{x}10^{-3}$ (>4mm) and $2\text{x}10^{-7}$ (>1cm) of the events. The bulk of the events on the tail come from vertices where there are one or more bad hits on the track (represented by the blue histogram in Figure 5.3.2.4). The rejection of tracks with bad hits depends strongly on the precision of the virtual A′ trajectory, which in turn depends on the size of the beamspot. For vertices reconstructed beyond 1 cm, the rejection factor with a 100 μm beamspot is ~10 times worse than for the 10μm spot. Having a small beamspot is very important.

The vertex resolution depends on the invariant mass of the particles being vertexed. Lower masses have worse Gaussian resolutions as shown in Figure 5.3.2.5. This is expected since the error on the opening angle (θ), due to multiple scattering, scales like: $\sigma(\theta)/\theta \sim (1/E)/(m/E) \sim 1/m$. Interestingly, even the tails of the resolution appear to also scale by 1/m as shown in Figure 5.3.2.6, which shows the fraction of reconstructed A′ candidates greater than a given Z value. The x-axis of Figure 5.3.2.6 is normalized such that Z_{norm}=(m(A′)/125MeV) Z_{cut}. There is little beam-energy dependence on the resolution.

In practice, there is much more we can do to clean up the vertex and mass resolution both at the track level (e.g. require isolated hits in the silicon; remove hits that are clearly from scattered beam electrons) and at the vertex level (momentum constraint). These will be pursued in the near future.

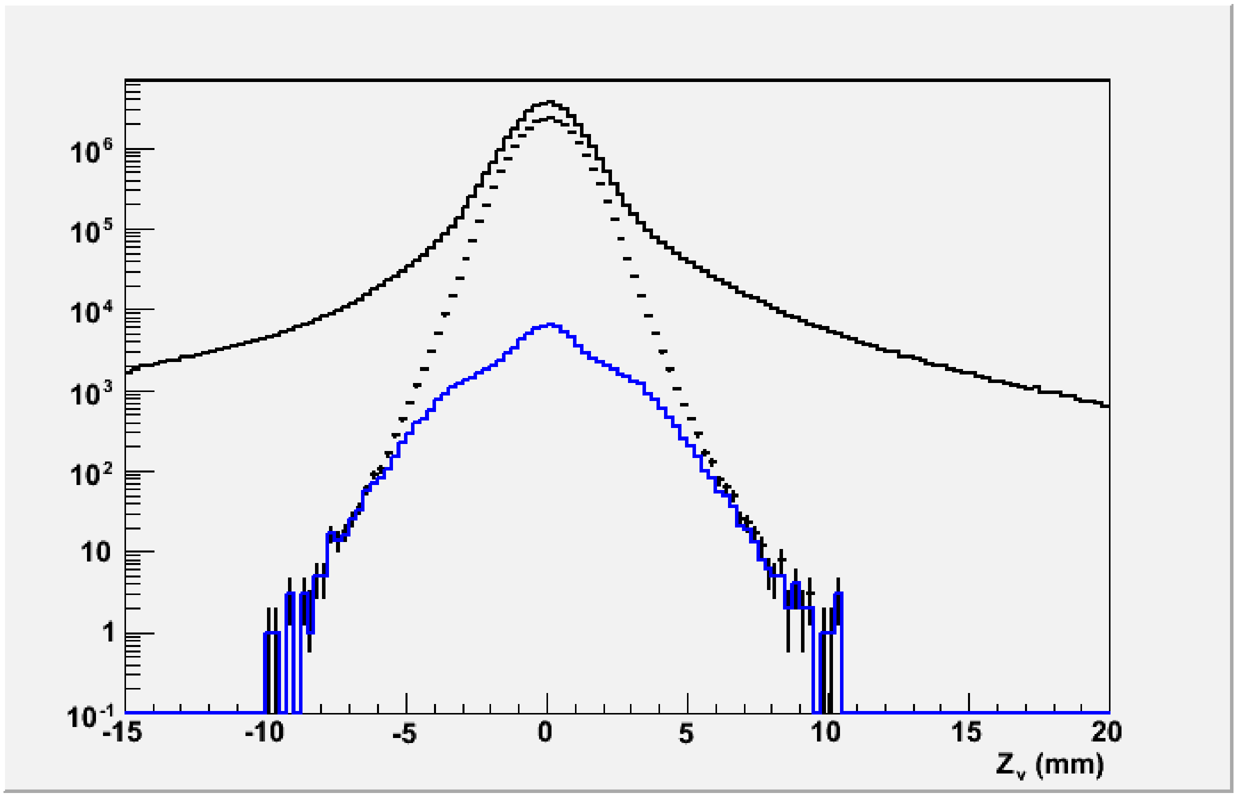

Figure 5.3.2.4: Distribution of reconstructed vertex position before (solid black) and after (points with errors) selection. The blue histogram shows the distribution for pairs that have at least one mishit after selection.

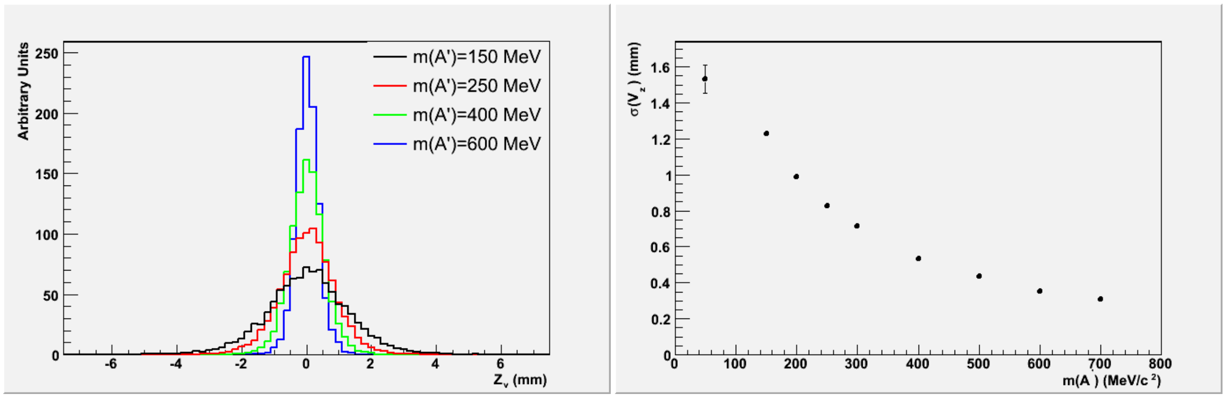

Figure 5.3.2.5: Left: The distribution of reconstructed vertex positions for A' different masses. Right: The (Gaussian) resolution dependence versus A' mass for signal-only events.

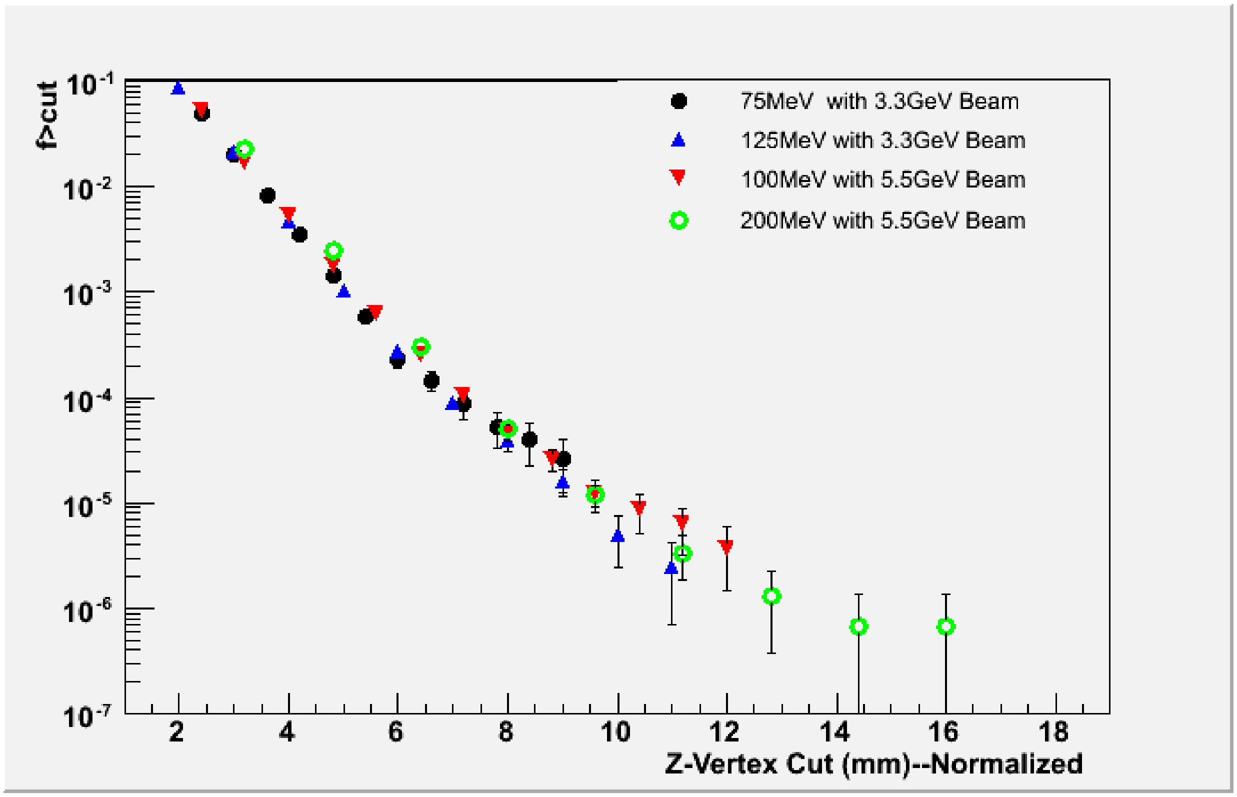

Figure 5.3.2.6: Fraction of V0 candidates with reconstructed Z-vertex position greater than the given cut.

6 Experimental Reach

The search channel for this experiment is, $A' \to e^+e^-$, with or without a displaced vertex, depending on the magnitude of the coupling α'. As such, the primary irreducible background is QED trident production, with rate given by the diagrams shown in Figure 3.2.1. Trident events can be usefully separated into ``radiative'' diagrams (Figure 3.2.1(a)), and ``Bethe-Heitler'' diagrams (Figure 3.2.1(b)), that are separately gauge-invariant.

The contribution from the radiative diagrams (Figure 3.2.1(a)) alone is a useful guide to the behavior of A' signals at various masses. In particular, the kinematics of A' signal events is identical to that of radiative trident events restricted to an invariant mass window near the A' mass. Moreover, the rate of the A' signal is simply related to the radiative trident cross-section within a small mass window of width $\delta m_{A'}$ by [1],

$$\frac{\mathrm{d}\sigma\left(\mathrm{e}^-\mathrm{Z}\to\mathrm{e}^-\mathrm{Z}\,(\mathrm{A}'\to\mathrm{e}^+\mathrm{e}^-)\right)}{\mathrm{d}\sigma\left(\mathrm{e}^-\mathrm{Z}\to\mathrm{e}^-\mathrm{Z}\,(\gamma^*\to\mathrm{e}^+\mathrm{e}^-)\right)} = \left(\frac{3\pi\epsilon^2}{2\,N_{eff}\,\alpha}\right)\left(\frac{m_{A'}}{\delta m_{A'}}\right) \tag{6.1}$$

where N_{eff} counts the number of available decay states. A fraction ϵ_{bin} of signal events will have reconstructed masses within the mass window, because of the finite mass resolution (for a $2.5 \times \sigma$ mass resolution window, $\epsilon_{bin} = 0.8$). Equation (6.1) corrected for ϵ_{bin} allows us to conveniently express the sensitivity to A' signals in terms of the radiative portion of the total QED trident statistics, which we will do shortly.

The Bethe-Heitler process has a much larger total cross-section than either the signal or the radiative trident backgrounds, but it can be significantly reduced by exploiting its different kinematics. In particular, the A' carries most of the beam energy (see the discussion in Section 3.2) while the recoiling electron is very soft and scatters to a wide angle. In contrast, the Bethe-Heitler process is not enhanced at high pair energy. Moreover, Bethe-Heitler processes have a forward singularity that strongly favors asymmetric configurations with one energetic, forward electron or positron and the other constituent of the pair much softer. These properties are discussed further in the Appendix of [1]. The geometric acceptance and trigger requirements select the region of phase space where signal is dominated, and the Bethe-Heitler background is smallest, as illustrated by Figure 3.2.2 (it should be emphasized, however, that even in this region the Bethe-Heitler background rate exceeds that of radiative tridents by roughly a factor of 5).

To compute the reach of the HPS experiment, we simulate the production of irreducible trident reactions in the detector. We additionally apply a mock-up of the geometric acceptance for the tracking and of the trigger requirements. In addition, high-statistics Monte Carlo samples at particular invariant masses have been used to estimate the background rejection efficiency for a vertex-based search.

We produce generator-level events using MadGraph and MadEvent [2] to compute the full matrix elements for $e^- Z \to e^-(e^+e^-)Z$ in leading order QED, but neglecting the effect of nuclear excitations on the kinematics in inelastic processes. We use the QED nuclear elastic and inelastic electric form-factors in [3]. The MadEvent code was modified to properly account for the masses of the incoming nucleus and electron in event kinematics.

We use a "reduced-interference" approximation that simplifies our analysis and is much less computationally intensive. In this approximation, we treat the recoiling e^- and the e^- from the produced pair as distinguishable. Furthermore, we separate trident processes into the radiative diagrams (Figure 3.2.1(a)) and the Bethe-Heitler diagrams (Figure 3.2.1(b)), and we calculate the cross-section for both of these diagrams separately. Within the acceptance and signal region for the HPS experiment, the Bethe-Heitler reactions dominate the trident rate by 4:1. We have checked that the "reduced-interference" approximation does not correct the trident cross-section by more than 10% in a representative kinematic region [4].

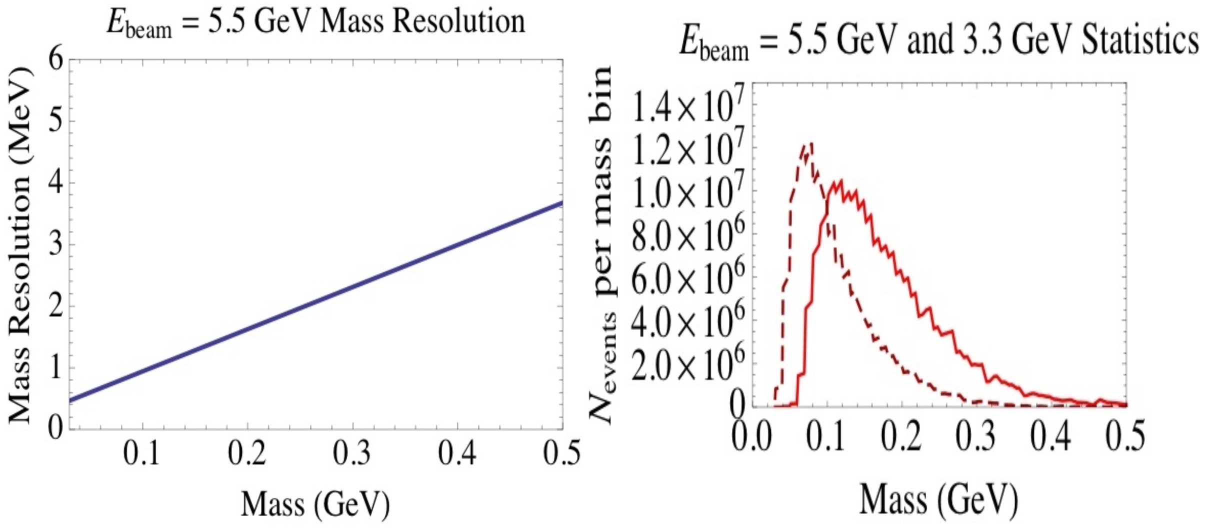

Figure 6.1.1. Left: Mass resolution $\sigma(m_{A'})$ assumed for reach calculations, estimated from momentum resolution achieved in Monte Carlo and expected angular resolution when using a 10μm beam spot constraint (this constraint has not been implemented in the calculations described in Section 5.3). Right: Distribution of statistics in full resonance search. The curves indicate the number of background QED trident events expected in a resolution-limited mass window of width $\delta m_{A'} = 2.5\,\sigma(m_{A'})$. The red curve corresponds to the distribution of statistics for a 3×10^6s run at 5.5 GeV beam energy, with a current of 400 nA on a 0.25% X_0 target, while the dashed maroon curve corresponds to 3.3 GeV beam energy and a 0.125% X_0 target.

6.1 Resonance Search

Equation (6.1) is used to compute the reach for a resonance search in the e^+e^- or $\mu^+\mu^-$ final state. We start by simulating radiative and Bethe-Heitler trident events and require that e^+e^- or $\mu^+\mu^-$ pairs pass the detector acceptance cuts. We additionally require that the total energy exceed 80% or the beam energy and that each track have at least 0.5 GeV of energy. We will refer to these cuts collectively as the "detector/trigger mock-up". We compute the total differential cross section, as a function of invariant mass, for radiative and Bethe-Heitler trident events to pass the detector/trigger mock-up cuts, and from this the final statistics is computed assuming a run duration of 3×10^6s, beam current of 400 nA, and a 0.25% X_0 target (0.125% X_0 for the 3.3 GeV setting). The assumed mass resolution and the background statistics expected in each resolution-limited mass window are shown in Figure 6.1.1.

To quantify statistical sensitivity, we assume that the continuum background in the resonance search can be modeled by a smoothly varying function and subtracted off. Exclusion power is then determined by the ratio of the signal within an invariant mass window to $\sqrt{N_{bin}}$, where N_{bin} is the total background statistics in the same window.

Using equation (6.1), the sensitivity for a resonance search is determined by

$$\left(\frac{S}{\sqrt{B}}\right)_{bin} = \left(\frac{N_{radiative}}{N_{total}}\right)\sqrt{N_{bin}}\left(\frac{3\pi\epsilon^2}{2\,N_{eff}\,\alpha}\right)\left(\frac{m_{A'}}{\delta m_{A'}}\right)\epsilon_{bin} \qquad (6.2)$$

Here, $\left(\frac{N_{radiative}}{N_{total}}\right)$ is the fraction of radiative reactions among all QED trident events in the search region. This quantity is determined by simulation as described below. N_{bin} is the total number of QED trident events residing in a given invariant mass search bin, and is determined by

$$N_{bin} \equiv \epsilon_{reco}^2 \times \epsilon_{stat}(m_{A'}) \times \sigma_{trigger} \times L.$$

Here L is the integrated luminosity, $\sigma_{trigger}$ is the trigger cross section, $\epsilon_{stat}(m_{A'})$ is the fraction of the total statistics in an invariant mass window centered on $m_{A'}$ of size $\delta m_{A'} = 2.5\,\sigma(m_{A'})$, and $\epsilon_{reco} \cong 0.85$ is the efficiency for reconstructing each track that is within the geometric acceptance of the detector.

6.2 Displaced Vertex and Resonance Search

A search for resonances that decay with cm-scale displaced vertices opens up sensitivity to much smaller couplings than can be observed through a resonance search alone. The vertex reconstruction and quality selection is discussed in Section 5.3. The track and vertex quality cuts retain only about ϵ_{vtx}=70% of both signal and background events. For the purpose of computing reach, the vertex quality requirements reduce the signal efficiency by a factor ϵ_{sigeff} discussed below, which includes this. Likewise we use the high-statistics Monte Carlo studies described in Section 5.3 to model the tails of the vertex distribution for decays at the target. These vertex distributions have been generated for e+e- invariant masses of 100 MeV and 200 MeV with 5.5 GeV beam energy, and 75 MeV and 125 MeV with 3.3 GeV beam energy. The vertex distributions thus obtained scale linearly with invariant mass. Away from these masses, we parameterize the background rejection factor $\epsilon_{rejection}(zcut)$, the fraction of events with a fake vertex beyond a beam line distance of $zcut$, by a smooth interpolation.

In Figure 6.2.1, we show the distribution of fake vertices in the z-direction along the beam line, as well as the distributions for signals corresponding to $\frac{\alpha'}{\alpha} = 10^{-8.5}$ and $10^{-9.5}$, as well as for true muonium (see Section 6.4).

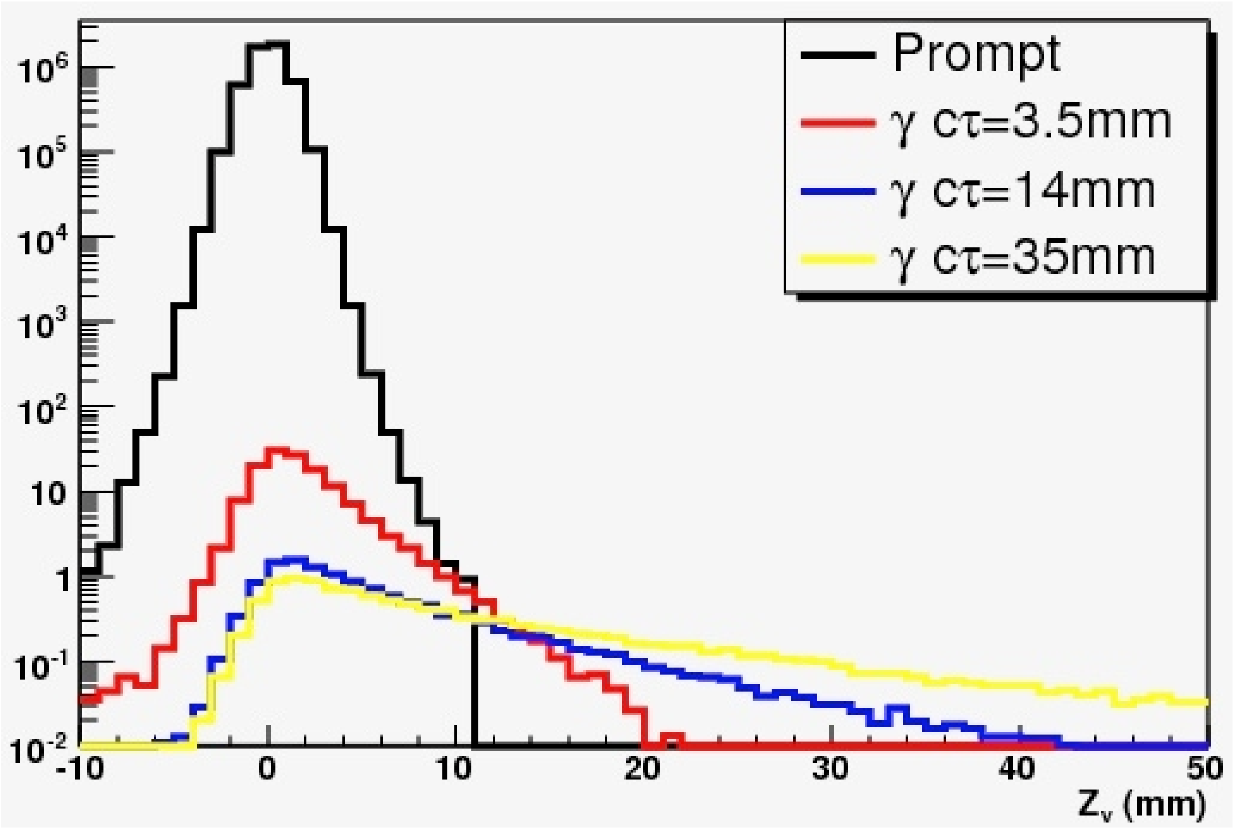

Figure 6.2.1 Signal and background vertex distributions in a resolution-limited invariant mass window, over the 3×10^6s run period at 5.5 GeV. The black curve represents the fake vertex distribution from trident events with mass in a $2.5\sigma(m_{A'})$ window about 200 MeV. The red and yellow curves are the vertex distributions for signal events from an A' of the same mass, with $\alpha'/\alpha = 10^{-8.5}$ ($\gamma c\tau = 3.5\ mm$) and $\alpha'/\alpha = 10^{-9.5}$ ($\gamma c\tau = 35\ mm$), respectively. The blue curve corresponds to the rate and vertex distribution expected from $l = 1$ (triplet) state of true muonium, with $\gamma c\tau = 14.2\ mm$ (see Section 6.4).

Because the fake vertex distribution falls quite rapidly, the greatest sensitivity is achieved far on the vertex tail, where less than one background event is expected. For the purpose of computing reach, we have determined a mass-dependent choice of $zcut(m_{A'})$ such that the expected background in each resolution-limited mass window $\delta m_{A'}$, with reconstructed vertices beyond this cut, does not exceed 0.5 events in the 3×10^6s run period. This requires rejection $\epsilon_{rejection}(zcut)$ of background events from the target at the level of 10^{-6} to 10^{-7}, achieved for $zcut \sim 5 - 30$ mm (see Figure 6.2.2). It should be noted that the vertexing for the 3.3 GeV configuration has not been fully optimized, so results for this setup are quite preliminary but we believe they are conservative.

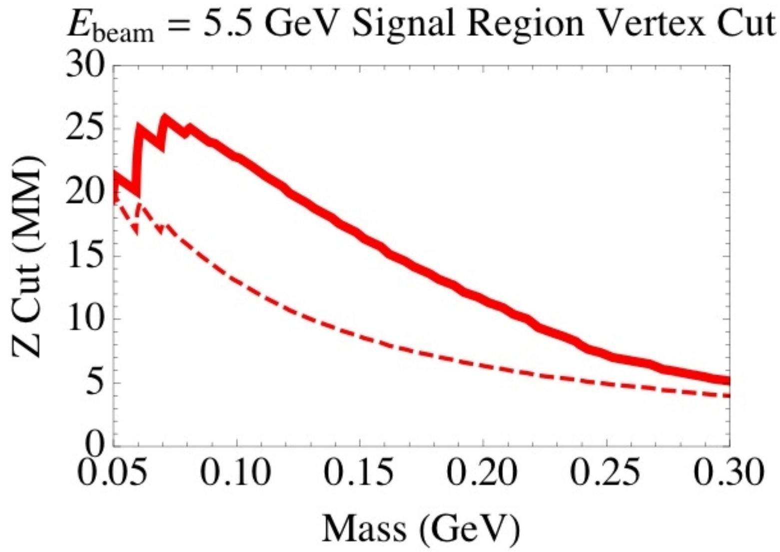

Figure 6.2.2 The minimum vertex displacement zmin (in mm) along the beamline, required for the vertex-based resonance search at 5.5 GeV. These are chosen to bring the expected background to 0.5 events in each resolution-limited mass window, over a 3×10^6s run. The solid curve corresponds to the vertex requirement that would achieve this rejection, assuming the tracking performance that has been achieved thus far in Monte Carlo studies. The thinner dashed line indicates the weaker requirement that could be imposed, with no loss in background rejection, if further tracking improvements can be used to reject vertices from tracks with mis-hits.

The geometric acceptance falls off at large decay lengths, as shown in Figure 5.2.3. For simplicity we compute reach using the geometric acceptance for z=0, but only considering decays with $z < zmax$=20 cm, so that the fraction of signal events included in the vertex search is

$$\epsilon_{sigeff}(zcut) \cong \epsilon_{vtx} \times \left(e^{-\left(\frac{zcut}{\gamma c\,\tau}\right)} - e^{-\left(\frac{zmax}{\gamma c\,\tau}\right)} \right)$$

Accounting for the reduced acceptance of both signal and background events, the statistical significance expected for a given value of can be computed from that of the pure resonance search as an expected signal can be computed by

$$\left(\frac{S}{\sqrt{B}}\right)_{bin,zcut} = \left(\frac{S}{\sqrt{B}}\right)_{bin} \frac{\epsilon_{sigeff}(zcut)}{\sqrt{\epsilon_{rejection}(zcut)}} > 2, \qquad (6.3)$$

Where $\left(\frac{S}{\sqrt{B}}\right)_{bin}$ is given by (6.2). For the small expected background rate (0.5 events/bin), however, this formula becomes irrelevant, as the exclusion sensitivity of the experiment is limited by the probability of a downward fluctuation in the signal. Thus, for the vertex reach contours in Figures 6.3.1 and 6.3.2, we additionally require an expected signal

$$S_{bin,zcut} = \left(\frac{N_{radiative}}{N_{total}}\right) N_{bin} \left(\frac{3\pi\epsilon^2}{2\,N_{eff}\,\alpha}\right) \left(\frac{m_{A'}}{\delta m_{A'}}\right) \epsilon_{sigeff}(zcut) > 2.4 \text{ events} \qquad (6.4)$$

6.3 Results for Reach Calculations

In this section, we present the expected reach of the HPS experiment, in both a full resonance search and the vertexing resonance search. We also discuss the impact on reach of further rejection of tracks with mis-hits, which presently dominate the tails of the background vertex distribution.

Figure 6.3.1 illustrates the expected reach in a 3×10^6s run period, with 5.5 GeV beam energy and 400 nA on a 0.25% X_0 target, as well as the regions excluded by past searches and the expected sensitivities of other possible searches. The upper thick red curve is the lower-limit of 2σ sensitivity for the full resonance search, while the lower thick red contour is the outer limit of sensitivity for the vertex-based resonance search, corresponding to 2.4 events in a resolution-limited mass window, where the vertex requirement has been chosen so that 0.5 background events are expected. The dashed maroon curves correspond to similar sensitivities, for a beam energy of 3.3 GeV and a 0.125% X_0 target. We stress however, that the latter curves are based on **very preliminary** performance estimates.

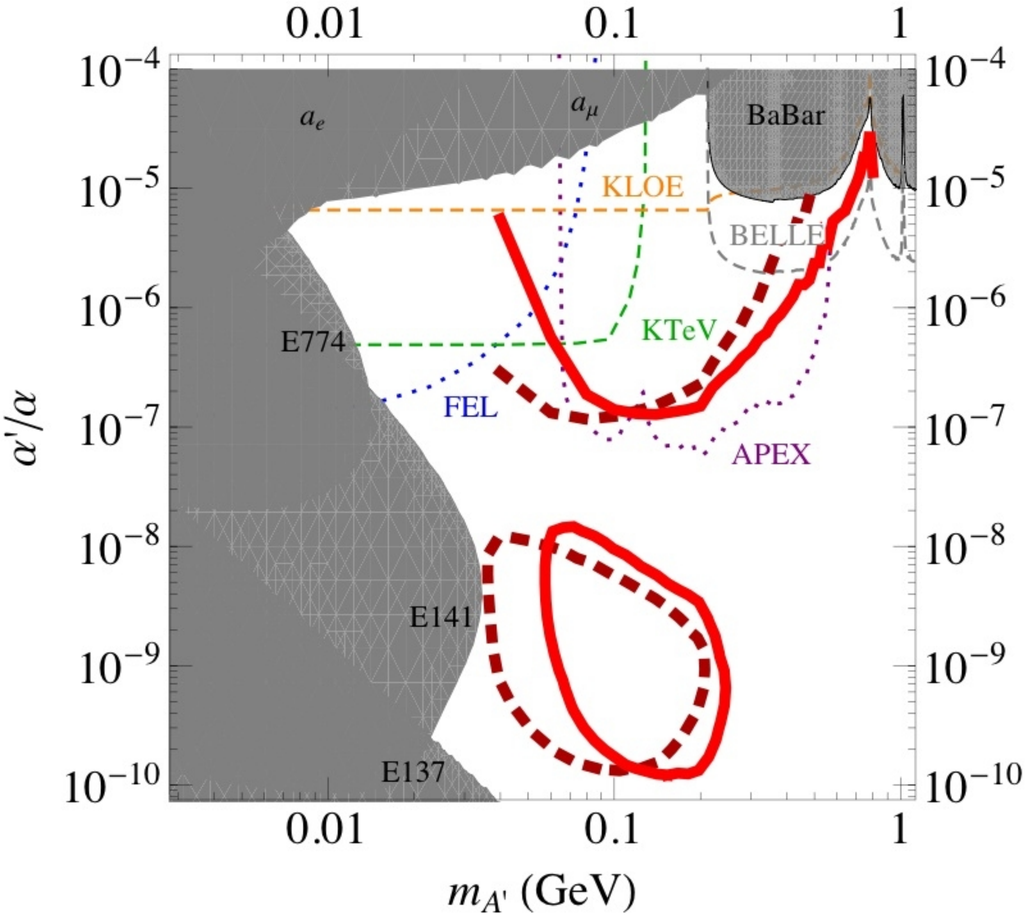

Figure 6.3.1 Anticipated reach in α'/α for the Heavy Photon Search (HPS) experiment (red and maroon lines), with existing constraints on an A' and potential sensitivities of A' searches in both existing data and

other proposed experiments as in Figure 2.3.1. The thick curves in the upper region of the plot correspond to the 2σ sensitivity of a full resonance search with 5.5 GeV beam energy and a 0.25% X_0 target (red), along with a preliminary estimate of sensitivity for a 3.3 GeV beam energy and a 0.125% X_0 target (dashed maroon). In each case a 3×10^6s run period with 400 nA beam current are assumed. The lower contours in the same colors denote the sensitivity of a vertex-based resonance search. Here the lines correspond to 2.4 signal events where the vertex requirement was chosen to have 0.5 expected background events in each resolution-limited mass window. To determine the vertex requirement needed to suppress background to this level, we have used the Monte Carlo results discussed in Section 5.3.

In Figure 6.3.2, we show the sensitivity of the vertex reach as a function of ε for a fixed mass of $m_{A'}$ = 150 MeV, which represents a one-dimensional vertical slice through the lower contours in Figure 6.3.1. This plot shows that the significance of the reach is highest towards the center of the contour, and drops off for higher and lower values of ε. This illustrates why the contour are closed curves.

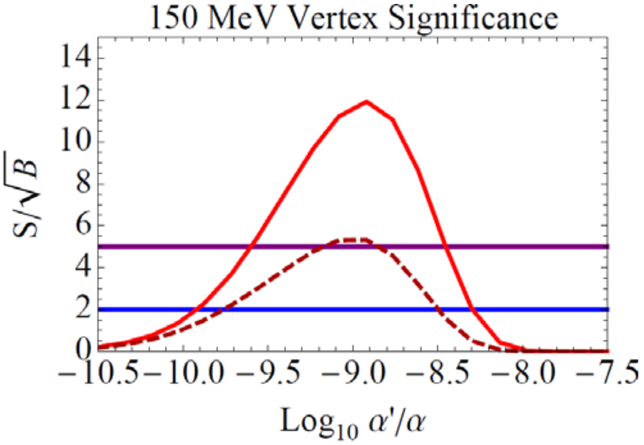

Figure 6.3.2 The sensitivity of the vertex reach as a function of ε for a fixed mass of $m_{A'}$ = 150 MeV, which represent a one-dimensional vertical slice through the lower contours in Figure 6.3.1. The solid red (dashed maroon) line corresponds to the 5.5 GeV (3.3 GeV) contour with the same assumptions as in Figure 6.3.1. The blue (purple) line corresponds to a significance of S/√B of 2 (5), which corresponds to about 2.4 (7) events in a resolution-limited mass window, where the vertex requirement has been chosen so that 0.5 background events are expected. This shows how the sensitivity is highest towards the center of the contours, and illustrates why the contours are closed curves.

As noted in Section 5.3, the tails of the fake vertex distribution are dominated by tracks with mishits in the first tracking layer. Several improvements to the tracking algorithm are being considered to improve rejection of these mis-hits. This would allow the same level of background rejection with a significantly lower choice of z_{min} (see Figure 6.2.2), resulting in improved sensitivity at higher couplings (shorter decay lengths) as shown in Figure 6.3.3.

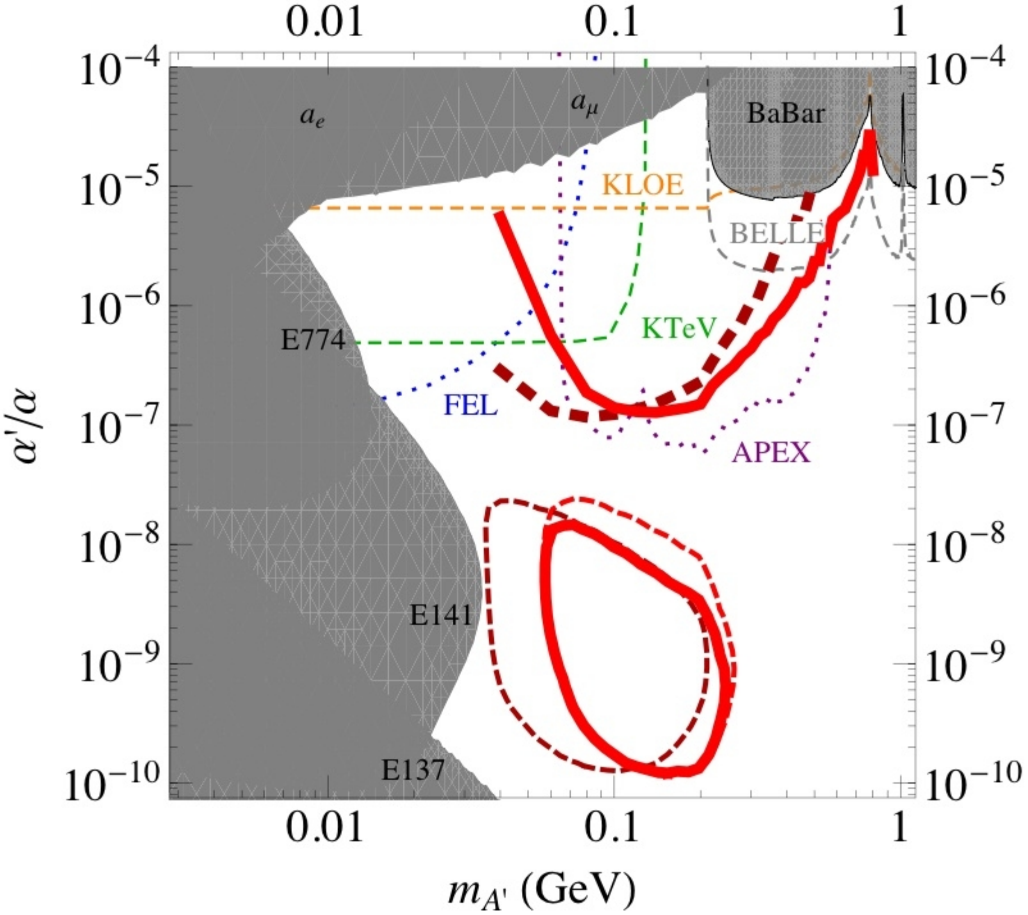

Figure 6.3.3 Impact of improved mishit rejection on sensitivity. All curves are as in Figure 6.3.1, except for the vertex-based resonance search sensitivity curves. The thinner dashed contours indicate the improved performance at 5.5 GeV (red) and 3.3 GeV (maroon) if all mis-hits can be rejected. For reference, the sensitivity for 5.5 GeV beam energy with the level of mishit rejection presently achieved in simulation is also shown as the thick red curve.

6.4 Potential for Discovering True Muonium

The proposed experiment has the potential to discover ``true muonium”, a bound state of a $\mu^+\mu^-$ pair, denoted here by $(\mu^+\mu^-)$. In this section, we review the motivation for such a search and discuss the experimental design considerations.

Positronium and muonium, bound states of (e^+e^-) and (μ^+e^-) pairs, respectively, have been produced and studied [5,6,7], but true muonium, or dimuon, has not yet been detected (see e.g. [8-16]). Together with tauonium $(\tau^+\tau^-)$ and tau-muonium $(\tau^\pm\mu^\mp)$, true muonium is the most compact pure QED system. While $(\tau^+\tau^-)$ and$(\tau^\pm\mu^\mp)$ are difficult to detect since the τ has a weak decay that competes with the QED decay, the μ is very long lived so that the decay of true muonium is purely a QED process. The detection of true muonium would be a great discovery and would constitute a further important test of QED.

The $(\mu^+\mu^-)$ ``atom" can be produced by an electron beam incident on a target such as tungsten [8,9], although we will see below that high Z targets are not important. The $(\mu^+\mu^-)$ atom has an infinite number of states with different binding energies; these states are distinguished by different values for the principal quantum number n. The binding energy of these states are E = -1407 eV/n^2, while their production cross-section scales as 1/n^3, so that higher-n states will be more difficult to produce [10]. In addition to states being distinguished by different principal quantum numbers, they are also produced either in a triplet or singlet state with very different decay properties. The singlet states decays to $\gamma\gamma$ with a rest frame lifetime of 0.602 n^3 ps, or 0.181 mm, while the triplet states decays to e^+e^- with a rest frame lifetime of 1.81 n^3 ps, or 0.543 mm. The triplet state thus decays exactly like an A′, and can be searched for in the same way. Of course, since its mass is known to be $2m_\mu$ within resolution, a precise search window can be specified. We will not consider the singlet state any further in this proposal, focusing exclusively on the triplet state.

The triplet production cross-section is given by [8]

$$\sigma_{triplet} = 1.20\,Z^2\frac{\alpha^7}{m_\mu^2}\left(1.79\ln\left(\frac{\mathrm{E_{beam}}}{\mathrm{m_\mu}}\right)-6.12\right) \tag{6.5}$$

$$\sim 4.6\,Z^2 10^{-41}\ \mathrm{cm}^2(\text{for } \mathrm{E_{beam}} = 5.5.\,\mathrm{GeV}) \tag{6.6}$$

We see that this cross-section scales like Z^2. However, the true muonium bound state breaks up very easily inside the target with a dissociation cross-section that is not only very large but also scales like Z^2 [8]

$$\sigma_{diss} \sim 1.3\,Z^2 10^{-23}\ \mathrm{cm}^2 \tag{6.7}$$

This means that only the bound states produced in the last fraction of the target actually make it out of the target before breaking up, and that the total production rate is effectively independent of Z. The effective thickness of not breaking up in the target is

$$t_b = \frac{1}{N\,\sigma_{diss}} \tag{6.8}$$

where N is the number density of atoms in the target. The choice of target thickness is not an important parameter when designing an experiment to search for true muonium. Target thicknesses larger than t_b do not help to increase the production rate of true muonium pairs, since those created at the beginning simply will not make it out the back end of the target before breaking apart. Of course, while the use of target thicknesses greater than t_b does not hurt the production of true muonium, it would hurt the production of the A′ which does scale linearly with target thickness, at least for thin enough targets. Note that for tungsten, t_b = 2.2 μm (0.064% r.l.), while for Carbon graphite, t_b = 190 μm (0.01% r.l.).

Using the triplet production and dissociation cross-sections, the total production rate of true muonium states is [8]

$$Rate_{(\mu^+\mu^-)} = 0.021\left(1.79\ln\left(\frac{\mathrm{E_{beam}}}{\mathrm{m_\mu}}\right) - 6.12\right)\ I\,(mA). \tag{6.9}$$

For the nominal running conditions of $\mathrm{E_{beam}}$ = 5.5 GeV, 400 nA beam current, 3×10^6 s and a single foil, this experiment would produce about 20 n=1 triplet true muonium states. The typical decay length of these states would be 1.4 cm. The optimal search for true muonium follows the approach of Section 6.3, requiring a vertex cut at about 1.5 cm to reject almost all QED background events, then searching for a resonance at 2 $\mathrm{m_\mu}$. Accounting for all efficiencies as discussed in 6.2 and 6.3, we would expect to see only about 2 true muonium events (we caution that the acceptance parametrization here is uncertain at the 50% level).

The production of true muonium events can be increased in several ways. While increasing the target thickness does not help (as discussed above), the production rate scales linearly with both the current and the number of target foils (spaced by 2 or more cm so that true muonium decays between foils). Using 800 nA and 2 or 3 target foils, instead of a single foil would produce 80 – 120 events, of which about 8-12 would be detectable in a vertex search.

Seeing the *n=2* state (which has a very large decay length of about 11.4 cm) will be more difficult, as we would produce only 1/8 as many of these states.

6.5 References

1. J. D. Bjorken, R. Essig, P. Schuster, and N. Toro, New Fixed-Target Experiments to Search for Dark Gauge Forces, Phys. Rev. D80 (2009) 075018, [0906.0580].
2. J. Alwall *et al.*, MadGraph/MadEvent v4: The New Web Generation, JHEP 0709 (2007) 028
3. K. J. Kim and Y.-S. Tsai, Improved Weizsäcker-Williams methos and its application to lepton and W-boson pair productions, Phys. Rev. D8 (1973) 3109
4. We thank M. Freytsis, G. Ovanesyan, and J. Thaler for independently verifying our cross-section calculation and for computing the full-interference trident cross-section for a representative kinematic region.
5. M. Deutsch, Phys. Rev. 82, 455 (1951).
6. J.I. Friedman and V.L. Telegdi, Phys. Rev. 105, 1681 (1957).
7. V.W. Hughes, D.W. McColm, K. Ziock and R. Prepost, Phys. Rev. Lett. 5, 63 (1960).
8. E. Holvik and H.A. Olsen, Creation of Relativistic Fermionium in Collisions of Electrons with Atoms, Phys. Rev. D35 2124 (1987).
9. N. Arteaga-Romero, C. Carimalo and V.G. Serbo, Phys. Rev. A 62, 032501 (2000) [arXiv:hep-ph/0001278].
10. S.J. Brodsky and R.F. Lebed, Production of the Smallest QED Atom: True Muonium $(\mu^+\mu^-)$, Phys. Rev. Lett. 102 , 213401 (2009), arXiv: hep-ph/0904.2225.

11. S. Bilen'kii, N. van Hieu, L. Nemenov, and F. Tkebuchava, Sov. J. Nucl. Phys., 10, 469 (1969).
12. V.W. Hughes and B. Maglic, Bull. Am. Phys. Soc. 16, 65 (1971).
13. J. Malenfant, Phys. Rev. D 36, 863 (1987).
14. S.G. Karshenboim, U.D. Jentschura, V.G. Ivanov and G. Soff, Phys. Lett. B 424, 397 (1998).
15. D.A. Owen and W.W. Repko, Phys. Rev. A 5, 1570 (1972).
16. U.D. Jentschura, G. Soff, V.G. Ivanov and S.G. Karshenboim, arXiv:hep-ph/9706401; Phys. Rev. A 56, 4483 (1997) [arXiv:physics/9706026]; S.G. Karshenboim, V.G. Ivanov, U.D. Jentschura and G. Soff, J. Exp. Theor. Phys. 86, 226 (1998) [Zh. Eksp. Teor. Fiz. 113, 409 (1998)].

7 Costs, Manpower, Schedule

Cost estimates for engineering, designing, fabricating, assembling, testing, and installing the Heavy Photon Search experiment in the Hall B alcove at JLab are given below. The costs reflect considerable savings coming from the donation of about 160 silicon microstrip sensors from Fermilab, the use of a refurbished analyzing magnet from SLAC, and many contributions from JLab, including $PbWO_4$ calorimeter crystals, chicane magnets, and magnet power supplies. Much of the calorimeter readout electronics utilizes designs which are already in place for the Hall B 12 GeV upgrade, eliminating engineering and design expense. Some of the calorimeter readout modules will be used in other JLab experiments. Collaborating institutions will donate engineering and design efforts for the ECal and Muon systems, affording additional savings.

The costs are given in an accompanying WBS summary table, below, which itemizes the major items subsystem by subsystem, and indicates whether JLab (J) or SLAC (S) takes responsibility for construction. Engineering, design, and technician labor rates include lab overheads, and differ between the two laboratories. Contingencies have been set at 30% for labor and 35% for M&S at SLAC, and somewhat lower at JLab, since full engineering designs are not yet available for the SLAC items, and many of the JLab items are similar to items recently constructed. The contingency for commercial items is generally about 10%. No overheads have been applied to M&S at either laboratory. A 10% overhead on the M&S would add roughly $150k to the cost of the project.

7.1 Subsystem Costs

The beamline will require some engineering and design, included in the WBS given below, in addition to the assembly of three girders, which hold the quadrupoles, BPMs, corrector magnets, viewers, and harps. The other major expenses include the bending magnet support stands, beam pipes and windows, analyzing and chicane magnets, power supplies, and power leads. Installation of the beamline elements is included explicitly. Including the labor for installation and contingencies, the beamline will cost about $590k.

The silicon tracker/vertexer requires design and fabrication of sensor modules, CF support structures and a CF support box, a vacuum chamber, and power supplies, a cooling system, and motors and controls. Including engineering, design, and prototyping, the tracker/vertexer will cost $830k.

The EM calorimeter is just downstream of the tracker. It utilizes existing $PbWO_4$ crystals and APD readout, but includes in addition Shashlyk or PB glass counters as well. Costs for the new counters and for adapting the existing crystals to the present experiment are included. A new temperature-controlled enclosure is required, as is a vacuum box to allow beam transport. Readout boards, cables, and power supplies complete the list of needed items. We assume engineering and design is done by an HPS collaborator, but include the cost of supporting a visiting physicist at JLab to do this work. The cost, including technician time for calorimeter assembly and testing, is $260k.

The muon system costs include iron absorber; the beam transport vacuum chamber; scintillator, wavelength shifting fibers, and PMTs; support stands; and cables and connectors. Again we assume engineering and design is done at JLab by a visiting physicist, but include technician labor for system fabrication. The total is about $180k.

This experiment relies on very fast data transmission and high trigger rates. JLab systems will provide the calorimeter and muon system readout and trigger, and define the overall DAQ architechture. A SLAC system will readout the silicon tracker/vertexer at ~40 MHz, select triggered events, and interface to the overall data stream. The SLAC SVT system will cost about $650k. The JLab ECal and trigger will cost about $600k, and JLab will absorb the overall system DAQ costs with its existing infrastructure.

Altogether, the HPS experiment will cost approximately $3.1M, including Lab overheads on labor and contingencies. That estimate assumes that collaborating institutions will help engineer and design the calorimeter and muon systems, and it reflects considerable savings arising from using existing apparatus and donations of major components.

The costs associated with storing and accessing the data and with data analysis expenses at collaborating institutions are not included.

7.2 Technical Manpower Needs

The estimated technical manpower at SLAC and JLab needed to prepare the HPS experiment are given in the WBS, and are summarized in Table 7.2.1 below. Needs are given in FTE years.

Subsystem	**Engineering**	**Design**	**Technician**	**Physicist**	**Grad Student**
Beamline	0.1	0.3	1.6		
Tracker	0.4	0.15	0.7	.3	.2
ECal	0.5*	0.5*	0.24		
Muon	0.5*	0.5*	0.1		
DAQ	0.5	0.5	0.9		

Table 7.2.1. FTE years of technical labor needed to engineer, design, fabricate, and install HPS. Engineering and design marked with an asterisk (*) is assumed provided by visiting scientists at JLab.

7.3 Timetable

The goal of the experiment is to be ready to take beam in Spring 2012. We feel it is very important to commission HPS before the shutdown for the 12 GeV Upgrade, so that we can react to experimental surprises during the shutdown. This leads us to an aggressive schedule, but one we have considered in some detail and think is feasible.This schedule of course depends critically on getting support for this experiment as early as possible in FY2011.

WBS	Component	Number	Unit	Materials	MContingency	Labor	LContingency	MTotal	LTotal	Total	Comment
1	Heavy Photon Search at JLab	1	each	1,263,220	329,419	1,182,980	320,156	1,592,639	1,503,136	3,095,775	
1.1	Beamline (J&S)	1	each	178,000	45,400	292,850	71,025	223,400	363,875	587,275	
1.1.1	Mechanical Engineer(J)	200	man hour	0	0	88	18	0	21,120	21,120	Design
1.1.2	Mechanical Designer(J)	480	man hour	0	0	60	12	0	34,560	34,560	Layout
1.1.3	Girder Construction (J)	1	each	90,000	22,500	47,700	9,540	112,500	57,240	169,740	
1.1.3.1	Girder #1 M&S	1	each	30,000	7,500	0	0	37,500	0	37,500	
1.1.3.2	Girder #2 M&S	1	each	30,000	7,500	0	0	37,500	0	37,500	
1.1.3.3	Girder #3 M&S	1	each	30,000	7,500	0	0	37,500	0	37,500	
1.1.3.4	Mechanical Technician(J)	900	man hour	0	0	53	11	0	57,240	57,240	Fabrication
1.1.4	Support Stands (J)	1	each	35,000	8,750	15,900	3,180	43,750	19,080	62,830	
1.1.4.1	Support Stand M&S	1	lot	35,000	8,750	0	0	43,750	0	43,750	
1.1.4.2	Mechanical Technician(J)	300	man hour	0	0	53	11	0	19,080	19,080	Fabrication
1.1.5	Beam Pipes and Windows (J)	1	each	20,000	5,000	15,900	3,180	25,000	19,080	44,080	
1.1.5.1	Beam Pipes and windows M&S	1	lot	20,000	5,000	0	0	25,000	0	25,000	
1.1.5.2	Mechanical Technician(J)	300	man hour	0	0	53	11	0	19,080	19,080	Fabrication
1.1.6	Analyzing Magnet (S)	1	each	18,000	5,400	124,550	37,365	23,400	161,915	185,315	
1.1.6.1	Parts to Refurbish Magnet	1	each	8,000	2,800	0	0	10,800	0	10,800	
1.1.6.2	Ship Analyzing Magnet to JLab	1	each	6,000	1,200	0	0	7,200	0	7,200	
1.1.6.3	Analyzing Magnet Support Frame	1	each	4,000	1,400	0	0	5,400	0	5,400	
1.1.6.4	Mechanical Designer(S)	160	man hour	0	0	130	39	0	27,040	27,040	
1.1.6.5	Mechanical Technician(S)	830	man hour	0	0	125	38	0	134,875	134,875	
1.1.7	Chicane Dipoles (J)	2	each	0	0	0	0	0	0	0	JLAB provides
1.1.8	Magnet Power Supplies (J)	3	each	0	0	0	0	0	0	0	JLAB provides
1.1.9	Power Leads M&S (J)	1	lot	15,000	3,750	0	0	18,750	0	18,750	
1.1.10	Mechanical Technician(J)	800	man hour	0	0	53	11	0	50,880	50,880	Installation
1.2	Tracker/Vertexer (S)	1	each	310,000	108,500	315,450	94,635	418,500	410,085	828,585	
1.2.1	Sensor Modules	1	each	40,000	14,000	167,000	50,100	54,000	217,100	271,100	
1.2.1.1	Si Microstrip Sensors	156	each	0	0	0	0	0	0	0	Fermilab provides
1.2.1.2	Sensor Module M&S	1	lot	40,000	14,000	0	0	54,000	0	54,000	
1.2.1.3	Mechanical Engineer(S)	280	man hour	0	0	150	45	0	54,600	54,600	Design
1.2.1.4	Mechanical Technician(S)	1,000	man hour	0	0	125	38	0	162,500	162,500	Fabricate
1.2.1.5	Graduate Student	1,000	man hour	0	0	0	0	0	0	0	Test
1.2.2	Support Box	1	each	30,000	10,500	51,800	15,540	40,500	67,340	107,840	
1.2.2.1	Support Box M&S	1	lot	30,000	10,500	0	0	40,500	0	40,500	
1.2.2.2	Mechanical Engineer(S)	40	man hour	0	0	150	45	0	7,800	7,800	
1.2.2.3	Mechanical Designer(S)	160	man hour	0	0	130	39	0	27,040	27,040	
1.2.2.4	Mechanical Technician(S)	200	man hour	0	0	125	38	0	32,500	32,500	Fabricate
1.2.2.5	Graduate Student	210	man hour	0	0	0	0	0	0	0	Test
1.2.3	Vacuum Chamber	1	each	30,000	10,500	75,250	22,575	40,500	97,825	138,325	
1.2.3.1	Vac Chamber M&S	1	lot	30,000	10,500	0	0	40,500	0	40,500	
1.2.3.2	Mechanical Engineer(S)	360	man hour	0	0	150	45	0	70,200	70,200	
1.2.3.3	Mechanical Technician(S)	130	man hour	0	0	125	38	0	21,125	21,125	Fabricate
1.2.3.4	Mechanical Technician(S)	40	man hour	0	0	125	38	0	6,500	6,500	Test
1.2.3.5	Physicist	100	man hour	0	0	0	0	0	0	0	Test
1.2.4	Readout Board Cables	1	each	5,000	1,750	6,400	1,920	6,750	8,320	15,070	

Page 1 of 3

HPS WBS.wbs

WBS	Component	Number	Unit	Materials	MContingency	Labor	LContingency	MTotal	LTotal	Total	Comment
1.2.4.1	Readout Board Cables	1	lot	5,000	1,750	0	0	6,750	0	6,750	
1.2.4.2	Electronic Engineer(S)	40	man hour	0	0	160	48	0	8,320	8,320	Design
1.2.4.3	Graduate Student	40	man hour	0	0	0	0	0	0	0	Test
1.2.5	Power, Pressure, Temp Systems	1	each	205,000	71,750	15,000	4,500	276,750	19,500	296,250	
1.2.5.1	Si System Power Supplies & Cables	1	lot	130,000	45,500	0	0	175,500	0	175,500	
1.2.5.2	Si System Cooling Plant, Piping, Fittings	1	lot	50,000	17,500	0	0	67,500	0	67,500	
1.2.5.3	Si System Motors & Controls	1	lot	20,000	7,000	0	0	27,000	0	27,000	
1.2.5.4	Si System Monitoring	1	lot	5,000	1,750	0	0	6,750	0	6,750	
1.2.5.5	Mechanical Engineer(S)	100	man hour	0	0	150	45	0	19,500	19,500	Design PPT
1.2.5.6	Graduate Student	250	man hour	0	0	0	0	0	0	0	Installation
1.2.5.7	Physicist	250	man hour	0	0	0	0	0	0	0	Installation
1.3	EM Calorimeter (J)	1	each	137,940	28,869	75,440	15,088	166,809	90,528	257,337	
1.3.1	Enclosure with vacuum box	1	each	73,000	18,250	0	0	91,250	0	91,250	
1.3.2	PbWO4 Connection Board	1	each	6,500	1,625	0	0	8,125	0	8,125	
1.3.3	PbWO4 Motherboard	1	each	11,000	2,750	0	0	13,750	0	13,750	
1.3.4	PMT for Pb Glass	96	each	300	30	0	0	31,680	0	31,680	
1.3.5	Signal/HV Cables and Connectors	96	each	90	9	0	0	9,504	0	9,504	
1.3.6	Support Stand	1	each	10,000	2,500	0	0	12,500	0	12,500	
1.3.7	Mechanical Technician(J)	480	man hour	0	0	53	11	0	30,528	30,528	Assembly,Test
1.3.8	Physicist Visitor(J)	2,000	man hour	0	0	25	5	0	60,000	60,000	Design, Test
1.4	Muon System (J)	1	each	89,880	14,920	60,600	12,120	104,800	72,720	177,520	
1.4.1	Iron absorber	1	lot	30,000	4,500	0	0	34,500	0	34,500	
1.4.2	Vac adapter and window	1	each	10,000	2,500	0	0	12,500	0	12,500	
1.4.3	Scintillator and Fibers	72	each	40	10	0	0	3,600	0	3,600	
1.4.4	Muon System assembly parts	1	lot	5,000	1,250	0	0	6,250	0	6,250	
1.4.5	PMTs and dividers	9	each	2,000	200	0	0	19,800	0	19,800	
1.4.6	HV & Signal cables and connectors	1	lot	5,000	750	0	0	5,750	0	5,750	
1.4.7	Signal Splitters	3	each	3,000	300	0	0	9,900	0	9,900	
1.4.8	Support Stand	1	each	10,000	2,500	0	0	12,500	0	12,500	
1.4.9	Mechanical Technician(J)	200	man hour	0	0	53	11	0	12,720	12,720	Fabricate
1.4.10	Physicist Visitor(J)	2,000	man hour	0	0	25	5	0	60,000	60,000	
1.5	SVT DAQ (S)	1	each	104,900	26,505	395,600	118,680	131,405	514,280	645,685	
1.5.1	Hybrid Proto	1	each	3,900	1,305	99,200	29,760	5,205	128,960	134,165	
1.5.1.1	APV25 Readout Chip	10	each	30	5	0	0	345	0	345	
1.5.1.2	Hybrid Proto M&S	1	lot	3,600	1,260	0	0	4,860	0	4,860	
1.5.1.3	Electronic Engineer(S)	160	man hour	0	0	160	48	0	33,280	33,280	Design
1.5.1.4	Electronic Designer(S)	160	man hour	0	0	130	39	0	27,040	27,040	Layout
1.5.1.5	Electronic Technician(S)	480	man hour	0	0	110	33	0	68,640	68,640	Test
1.5.2	Hybrid Production	1	each	46,500	12,375	58,400	17,520	58,875	75,920	134,795	
1.5.2.1	APV25 Readout Chip	650	each	30	5	0	0	22,425	0	22,425	
1.5.2.2	Hybrid Production M&S	1	lot	27,000	9,450	0	0	36,450	0	36,450	
1.5.2.3	Electronic Engineer(S)	80	man hour	0	0	160	48	0	16,640	16,640	Design Mods
1.5.2.4	Electronic Designer(S)	80	man hour	0	0	130	39	0	13,520	13,520	Layout Mods
1.5.2.5	Electronic Technician(S)	320	man hour	0	0	110	33	0	45,760	45,760	Test
1.5.3	Readout Bd Proto	1	each	4,500	1,575	81,600	24,480	6,075	106,080	112,155	

Page 2 of 3

HPS WBS.wbs

WBS	Component	Number	Unit	Materials	MContingency	Labor	LContingency	MTotal	LTotal	Total	Comment
1.5.3.1	Readout Board Proto M&S	1	lot	4,500	1,575	0	0	6,075	0	6,075	
1.5.3.2	Electronic Engineer(S)	160	man hour	0	0	160	48	0	33,280	33,280	Design
1.5.3.3	Electronic Designer(S)	160	man hour	0	0	130	39	0	27,040	27,040	Layout
1.5.3.4	Electronic Technician(S)	320	man hour	0	0	110	33	0	45,760	45,760	Test
1.5.4	Readout Bd Production	1	each	18,000	6,300	29,200	8,760	24,300	37,960	62,260	
1.5.4.1	Readout Board Production M&S	1	lot	18,000	6,300	0	0	24,300	0	24,300	
1.5.4.2	Electronic Engineer(S)	40	man hour	0	0	160	48	0	8,320	8,320	Design Mods
1.5.4.3	Electronic Designer(S)	40	man hour	0	0	130	39	0	6,760	6,760	Layout Mods
1.5.4.4	Electronic Technician(S)	160	man hour	0	0	110	33	0	22,880	22,880	
1.5.5	T1 ACTA Proto	1	each	2,000	700	32,000	9,600	2,700	41,600	44,300	
1.5.5.1	T1 ACTA Proto M&S	1	lot	2,000	700	0	0	2,700	0	2,700	
1.5.5.2	Electronic Engineer(S)	80	man hour	0	0	160	48	0	16,640	16,640	Design
1.5.5.3	Electronic Designer(S)	80	man hour	0	0	130	39	0	13,520	13,520	Layout
1.5.5.4	Electronic Technician(S)	80	man hour	0	0	110	33	0	11,440	11,440	Test
1.5.6	ATCA Crate/ CPU	1	each	20,000	2,000	8,800	2,640	22,000	11,440	33,440	
1.5.6.1	ATCA Crate/CPU M&S	1	lot	20,000	2,000	0	0	22,000	0	22,000	
1.5.6.2	Electronic Technician(S)	80	man hour	0	0	110	33	0	11,440	11,440	
1.5.7	Server/DAQ	1	each	5,000	500	51,200	15,360	5,500	66,560	72,060	
1.5.7.1	Server	1	each	5,000	500	0	0	5,500	0	5,500	
1.5.7.2	Electronic Engineer(S)	320	man hour	0	0	160	48	0	66,560	66,560	DAQ Code
1.5.8	System Test	1	each	5,000	1,750	35,200	10,560	6,750	45,760	52,510	
1.5.8.1	Si System Test M&S	1	lot	5,000	1,750	0	0	6,750	0	6,750	
1.5.8.2	Electronic Technician(S)	320	man hour	0	0	110	33	0	45,760	45,760	
1.6	ECal Trigger, DAQ (J)	1	each	442,500	105,225	43,040	8,608	547,725	51,648	599,373	
1.6.1	Electronic Engineer(J)	200	man hour	0	0	88	18	0	21,120	21,120	JLAB provides
1.6.2	Electronic Technician(J)	480	man hour	0	0	53	11	0	30,528	30,528	JLAB provides
1.6.3	FADC Board	45	each	7,000	1,750	0	0	393,750	0	393,750	
1.6.4	TI Board	3	each	5,000	1,250	0	0	18,750	0	18,750	
1.6.5	SD Board	3	each	4,000	1,000	0	0	15,000	0	15,000	
1.6.6	CTP Board	3	each	6,500	1,625	0	0	24,375	0	24,375	
1.6.7	CPU Board	3	each	5,000	1,250	0	0	18,750	0	18,750	
1.6.8	VXS Crate	3	each	12,000	1,200	0	0	39,600	0	39,600	
1.6.9	Cal Cables and Misc	1	lot	30,000	7,500	0	0	37,500	0	37,500	
1.7	System (J)	1	each	0	0	0	0	0	0	0	
1.7.1	Network Switches/Routers	0	lot	0	0	0	0	0	0	0	JLAB provides
1.7.2	Event Builder	0	each	0	0	0	0	0	0	0	JLAB provides
1.7.3	File Server	0	each	0	0	0	0	0	0	0	JLAB provides
1.7.4	Level 3	0	each	0	0	0	0	0	0	0	JLAB provides
1.7.5	Event Recorder	0	each	0	0	0	0	0	0	0	JLAB provides

8 Run Plan

The search for heavy photons provides an exciting and topical research program for Jefferson Laboratory, one with the potential for important discoveries which should be pursued aggressively. The Heavy Photon Search experiment hopes to move rapidly to designing, building, commissioning, and running the HPS. The plan below is aimed at producing a critical mass of the HPS detector and beamline before the 2012 shutdown, so that critical technologies can be demonstrated, critical running conditions determined, the data acquisition system exercised, and enough test data taken to evaluate potential shortcomings and seed the development of analysis programs.

The plan discussed below has several steps. The first would occur late next spring, when we'd use available Hall B time to test the new front end electronics for the ECcal and muon system, and the Silicon Vertex Tracker (SVT). Next, we would utilize the long down scheduled for the Summer and Fall of 2011 for installation of the major HPS beamline components. Final HPS installation, commissioning, and a test run would occur in Spring, 2012. Some re-installation and commissioning of the completed detector will occur after the 12 GeV upgrade, and must be coordinated with installing and commissioning the upgraded CLAS12 detector.

The successful execution of this run plan depends on rapid approval and funding for the experiment.

8.1 Pre-run Test of Electronics

The front-end readout electronics for the ECal and the muon system, and for the level 1 trigger hardware will utilize electronics developed for JLAB 12 GeV upgrade project. The SVT will be readout and digitized using the APV25 hybrid and ATCA (Advanced Telecommunication Computing Architecture) readout boards developed at SLAC. We plan initial tests of both electronic systems in the spring of 2011.

The first set of JLab-made FADCs and trigger boards will be ready for test by January 2011. It is planned to build a setup consisting of one VXS crate with 12 FADC boards and a Crate Trigger Processing board, and a Trigger Interface board for the CLAS12 pre-shower calorimeter cosmic ray tests. This setup will be ready for testing during the spring of 2011. It will include a cluster finding algorithm, somewhat different from the one proposed for the HPS experiment, for the level 1 trigger system.

If prototype SVT sensors, hybrids, and readout are available, the SVT readout can be tested as well. This may be done in the Hall B magnetic pair spectrometer during the Hall B tagger calibration run, [1] or in parallel to CLAS physics running, downstream of the vacuum window in the tagger system. In the latter case, a few sensors could be installed within the helium bag through which the electron beam passes on the way to the tagger dump. They would be mounted somewhat off beamline, to catch the tails of the beam after it has multiple coulomb scattered in the initial radiator. This would allow demonstration of the SVT readout electronics, and allow the possibility of preliminary occupancy measurements as well.

8.2 May-November 2011 Beamline and Magnet Installation

During the six month down from May to November of 2011, many of the support structures for the beam line elements, the chicane magnets, and the detectors can be installed. It will not be possible to install small aperture beam line elements (quads, correctors, BPMs) because of their incompatibility with CLAS running. (The beam after the CLAS target must be transported with larger apertures to avoid interactions of the scattered beam on these elements and on small vacuum beam pipe.) It will, however, be important to install the analyzing magnet, the larger aperture vacuum chambers, and cables for beam line devices and chicane magnets during this six month down.

8.3 Beamline and Detector Installation, Checkout, and Test Run, Spring 2012

Final installation of the beam line and the detector systems will be done just before commissioning. If the cabling is in place, installation, survey, and testing of the beam line elements will take a week and will be done by the accelerator crew. Installation of detector elements, including installation of the first magnet of the chicane (on a special platform after the forward carriage), vacuum boxes, and cabling will take about one and a half or two weeks.

Beam line commissioning will take about 3 to 5 days. Commissioning of the detectors and determination of the acceptable luminosity will take about one week. Following commissioning, there will be a one week test run. A total of about three weeks will be needed to fully commission and test the HPS setup.

Anything installed on the forward carriage and on the special platform (the first magnet of the chicane and some of beam line elements) will be removed from Hall B after the Spring 2012 HPS run. This is needed for CLAS decommissioning and eventually 12 GeV detector and magnet installation.

8.4 Re-installation, Checkout and Physics Run after the 12 GeV Upgrade

In the 12 GeV era, beam elements and detector components will be re- installed prior to the HPS run. This will take about a week. Beamline and detector commissioning will take additional one or two weeks. HPS will then be ready for its major data taking. Details of this plan are still being developed, but we imagine roughly three months of running time, split between perhaps three incident electron beam energies (say 2.2, 6.6, and 11 GeV) so as to maximize the experimental reach of the heavy photon search over a wide range of masses. Detailed running plans for the true muonium search also need to be refined. It may be that true muonium running can be incorporated into the above heavy photon search running, but it is also possible that detecting and studying true muonium will require dedicated running and special targets for an additional month or two.

8.5 Reference

1. S. Stepanyan et al., **NIM A** 572, 654 (2007)